UNIVERSITÀ DEGLI STUDI DELL'INSUBRIA
Dipartimento di Scienza e Alta Tecnologia

SPECTROSCOPIC SIGNATURES OF SUB-PC MASSIVE BLACK HOLE BINARIES

Thesis submitted for the degree of

Doctor Philosophiae

Candidate
Carmen Montuori

Supervisor: **Prof. F. Haardt**
Co-supervisor: **Prof. M. Colpi**

November 2012

Abstract

The focus of this thesis is on the electromagnetic signatures associated with massive black hole (MBH) binaries (MBHBs). In current models of structure formation, galaxies assemble in a bottom-up hierarchical fashion. Observations show that MBHs are hosted in the nuclei of almost all nearby massive galaxies. The existence of close MBHBs is therefore expected as the result of galaxy mergers, although clear observational evidences of MBHBs remain elusive. Most of the current sub-pc MBHB candidates have been spectroscopically selected through the Doppler-shift technique. This method consists in the identification of broad emission lines (BELs) shifted with respect to the galaxy reference frame, as traced by the set of narrow lines (NELs). This shift is due to the hypothesized motion of the active MBH orbiting in a close binary. However velocity off-sets between BELs and NELs are not a unique feature of close MBHBs, and cannot be searched for beyond $z \sim 0.8$ since most NELs fall out of the wavelength range covered by current optical surveys. This work presents our contribution to (i) the prediction of new spectroscopic features associated with MBHBs at different evolutionary stages in the aftermath of a gas-rich merger, and to (ii) the search for new secure candidates at different redshifts, ruling out other possible interpretations of their physical nature.

In the first part of this thesis we discuss a MBHB model envisaging a set of narrow lines characterized by the same Doppler-shift displayed by the BELs. This additional NEL system originates from the lower density gas orbiting in the so called gap region excavated by the gravitational interaction between the sub-pc MBHB and a surrounding thin circum-binary disk. We propose this model to interpret the features observed in the spectrum of the quasar SDSSJ092712.65+294344.0 (SDSSJ0927 hereafter). For the case of this peculiar source we show that the binary hypothesis is favored against the other possible physical scenarios of a recoiling AGN or of a chance superposition of

two distinct objects in a galaxy cluster. However further follow up observations are mandatory to monitor on longer timescales ($\gtrsim$ 10 yr) the periodic drift of the BELs expected over the binary orbital period, and to gather additional information on the quasar host galaxy and its close environment. Our study on SDSSJ0927 contributed to the realization of a systematic search for MBHB candidates at $z \lesssim 0.8$ through the development of automatic procedures by different groups including ours. The new algorithm implemented by our group will be also adapted to look for new candidates at higher redshifts based on the presence of two displaced peaks in the profile of the broad CIV line interpreted in terms of two active binary MBHs.

In the second part of this work, we devise a new spectroscopic approach to select MBHBs based on peculiarly reduced flux ratios between broad lines of lower and higher ionization potentials. In particular, we show that MBHBs can display anomalously small flux ratios between the MgII and CIV BELs, i.e. $F_{\rm MgII}/F_{\rm CIV} \lesssim 0.15$, in a limited range of sub-pc separations due to the erosion of the BEL emitting material bound to the secondary active MBH. This erosion is due to the tidal field of the more massive binary companion. The advantage of our newly proposed technique is twofold: (i) it can select new candidates at higher redshifts, $z \sim 2$, where both the considered BELs are visible in the optical spectrum, and (ii) the detection of a reduced $F_{\rm MgII}/F_{\rm CIV}$ would be a strong indication of the presence of a sub-pc MBHB since it is not expected in the other physical scenarios alternative to the binary hypothesis.

We show that it is possible to use our flux ratio criterion to select peculiar AGN spectra at $z \sim 2$ from the database of the Sloan Sky Digital Survey. These peculiar sources can be observed again in the IR band to look for a shift between the broad lines of Hβ, MgII and CIV and the narrow [OIII]λ5007. We start this new MBHB search with a small sample of 9 targets observed in the NIR-H band with the Very Large Telescope. Two sources are selected as binary candidates because the lower ionization lines of the MgII and of the Hβ have reduced fluxes relative respectively to the higher ionization line of the CIV and of the [OIII], and the three observed BELs show moderate shifts up to 1000 $\rm km\,s^{-1}$ relative to the narrow [OIII]. Hence we plan to perform new optical observations of these two sources to confirm and monitor the measured shifts, and to complete the search for MBHBs at $z \sim 2$ to check the reliability of our newly proposed spectroscopic approach.

Contents

Introduction

Understanding the role played by massive black holes (MBHs) in the process of galaxy formation and evolution is essential to gather up in a coherent cosmological picture the many different results accumulated during the last decades in a variety of astrophysical studies. Black holes with $10^6 - 10^9$ $\mathrm{M}_\odot$ are considered the central engines of the accretion process powering the most distant and luminous Active Galactic Nuclei (AGN), also referred to as quasars, up to $z \lesssim 7$ (Mortlock et al. 2011), as well as the less energetic AGN observed at lower redshifts (e.g. Merloni 2004). The imprints of quiescent MBHs have been found in the dynamics of gas and stars observed in the bulges of nearby galaxies and in our own Milky Way indicating that MBHs are ubiquitous in the nucleus of massive galaxies (e.g. Richstone et al. 1998). Black hole masses have also been found to correlate with the large scale properties of their host systems, such as the bulge mass, velocity and luminosity, suggesting a deep link between the evolution of MBHs and their host galaxies (e.g. Gültekin et al. 2009 and references therein).

Mergers between (pre-)galactic objects predicted in the hierarchical cosmological model are thought to be an important driver of both the MBH-host correlations and the redshift evolution of the AGN luminosity function whose peak is observed at $z \approx 2$ for optically selected samples (e.g. Richards et al. 2009). The general picture considers todays inactive MBHs as the result of a past phase of intense activity responsible for the growth of the seeds holes in the first proto-galaxies at high redshifts through a series of mergers and accretion events (e.g. Volonteri et al. 2003; Hopkins et al. 2006; Shankar et al. 2009). The strong tidal fields acting in major mergers between gas-rich systems are able to convey great amount of cold gas towards the nuclear regions of the remnant system starting intense episodes of star formation and the accretion onto the central MBH (e.g. Barnes & Hernquist 1996). The energy output of the powerful AGN phase can have a feedback effect on the large scale environment contributing to shape the galaxy properties and to self-regulate the MBH accretion rate, possibly determining the observed MBH-host relations (e.g. Di Matteo et al. 2005, Croton et al. 2006). Observational evidences supporting this evolutionary scenario indicate that dusty, sturburst galaxies luminous in the IR and sub-millimeter bands show signs of recent or on-going interactions and are often associated with nuclear activity (e.g. Sanders & Mirabel 1996, Alexander et al. 2003).

The formation of massive black hole binaries (MBHBs) is a crucial step in this hierarchical scenario of structures assembled through mergers between systems hosting a central MBH (e.g. Begelman, Blandford & Rees 1980). Inspiralling MBHs reaching very close spatial separations, of the order $\lesssim 10^{-3}$ pc, are also expected to be the among the loudest sources of gravitational waves (GWs) to be detected by future space mission like the New Gravitational-wave Observatory (NGO; Amaro-Seoane et al. 2012) and the on-going Pulsar Timing Array experiment (PTA; e.g. Hobbs et al. 2010). Our theoretical and observational capability to describe the MBHB evolutionary history is challenged by the need to cover a huge dynamical range. Ideally, a realistic description should start from a distance of ~ 100 kpc, on the scale of a galactic merger, going down to separations $\lesssim 1$ pc, where the two MBH starts their orbital evolution as a true Keplerian binary until reaching the coalescence for GW emission.

Up to date, we know about a single case of a spatially resolved Keplerian system of two MBHs in the nucleus of the radio galaxy 0402+379 (e.g. Rodriguez et al. 2006) while the uncertainties in the expected number of MBHBs detectable through electromagnetic and gravitational waves are still large. Further investigations on the MBHB dynamics in different environments and on the related peculiar observational features are therefore essential. In this thesis we present our contribution to the study of the electromagnetic signatures possibly associated with MBHBs both from a *theoretical* point of view, through the prediction of new spectroscopic features distinctive of genuine sub-pc systems, and with *observations*, through the selection of new binary candidates at different redshifts.

Outline

In Chapter 1 we describe our theoretical understanding of the main physical mechanisms driving the formation and the orbital evolution of MBHBs in the different stages of a galaxy merger. In particular we focus on the case of MBHBs evolving in gas-rich environments and on the results obtained in the last years with the use of high resolution numerical simulations. The theoretical framework introduced in the first chapter is at the basis of the MBHB dynamical scenario considered in this thesis and discussed in Ch. 3 and Ch. 4.

In Chapter 2 we summarize the main properties of an up-to-date list of the most relevant observational evidences of MBH pairs characterized by the presence of at least one active MBH and spatial separations ranging from several kpc down to sub-pc scales.

In Chapter 3 we first present the binary model proposed by our group to describe the spectral properties of a specific source, namely the quasar SDSSJ092712.65+294344.0 (SDSSJ0927 hereafter). Then we show that the discovery of this peculiar object concurred in the development of a systematic search for sources displaying similar spectroscopic signatures, yielding to the discovery of other ~ 100 MBHB candidates. We also discuss other possible physical interpretations of this peculiar class of AGN, not involving the presence of a binary system.

In Chapter 4 we present a new spectroscopic technique to select secure sub-pc MBHB candidates based on the measure of peculiar values for the flux ratio between two prominent broad emission lines with different ionizing potentials observed in AGN spectra. Besides we report the results of new IR spectroscopic observations obtained by our group for a small sub-set of MBHB candidates selected at $z \sim 2$ relying on our newly proposed criterion.

In Chapter 5 we summarize this work and give our conclusions. More technical details about the numerical codes considered in this work can be found in Appendix I and II.

Chapter 1

Formation of MBH binaries in galaxy mergers

This Chapter describes the principal results achieved in the study of the physical mechanisms guiding the formation and the subsequent dynamical evolution of a MBHB during a galactic merger. The study of the MBHB dynamics is directly linked to the fundamental question of galaxy formation in a hierarchical cosmological scenario. Our theoretical expectations for the timescales of the binary formation, the number of observable systems and the effective binary coalescence rate are therefore important to attend relevant astrophysical issues such as: the evolutionary history of MBHs, the link between mergers and the triggering of nuclear activity and the MBH-host relations.

Following the seminal paper focused on stellar dynamical effects by Begelman, Blandford and Rees (1980; BBR hereafter), we can distinguish different stages in the overall MBHB evolutionary path. The first phase of MBH pairing is driven by the dynamical friction acting on the single MBHs hosted in the interacting galactic nuclei. This gravitational drag arises in response to the perturbation induced on the background distribution of stars, gas and dark matter by the two MBHs and causes their sinking toward the center of the remnant. In the advanced stages of this process, the two MBHs bind in a Keplerian binary when the total mass enclosed within their relative separation is lower than the sum of the two black hole masses. In the simplest case of a stellar background described as a singular isothermal sphere (SIS), we can define the scale below which the two MBHs form a binary as:

$$a_{\rm BHB} \sim \frac{GM}{2\sigma^2} \sim 5.6\, M_8\, \sigma_{200}^{-2} \text{ pc} \tag{1.1}$$

where $M = M_1 + M_2$ is total binary mass in units of 10^8 $\rm M_\odot$, σ is the one dimensional velocity dispersion of the galaxy nucleus and $\rho(r) = \sigma^2/2\pi G r^2$ is the SIS density profile. At this point, it is useful to introduce the influence radius, $R_{\rm infl}$, defined as the scale below which the gravitational potential is dominated by the mass of the single MBH. We can thus alternatively state that a MBHB is formed when the two holes orbit closer than the influence radius of the more massive one. The expression of $R_{\rm infl}$ varies depending on the properties of the environment and on the MBH relative motion. In the case of a MBH sitting at rest in the center of a SIS, we have:

$$R_{\rm infl}^{\rm SIS} \sim \frac{GM_{\rm BH}}{\sigma^2} \sim 11.2\, M_{\rm BH,8}\, \sigma_{200}^{-2} \text{ pc} \tag{1.2}$$

The mass enclosed within $R_{\rm infl}^{\rm SIS}$ is two times that of the MBH, consistently with the definition given in eq. 1.1. Similar considerations can be made in gas-rich environments provided that the contributions of the thermal and turbulent motions and the MBH velocity relative to the medium are added to the velocity dispersion in eq. 1.2.

Once reached the stage of binary formation, the two MBHs starts to lose energy and angular momentum through the interactions with the single stars and/or the torques exerted by the surrounding gas. In order to coalesce in less than 10^{10} yr because of GW emission, the MBHB separation has to shrink down to a small value of the order of:

$$a_{\rm GW} \sim 0.06\, f(e)^{1/4}\, \frac{q^{1/4}}{(1+q)^{1/2}}\, M_8^{3/4} \text{ pc} \tag{1.3}$$

where $f(e) = [1+(73/24)e^2+(37/96)e^4](1-e^2)^{-7/2}$ is a function of the binary eccentricity e (Peters 1964) and $q = M_2/M_1 \leq 1$ is the binary mass ratio.

The first numerical simulations of collisionless mergers between idealized spherical galaxy models showed that the MBH pairing efficiency is higher for mergers between systems with equal masses in the galactic cores (major mergers) while it is strongly reduced for very unequal mass (minor) mergers with core density contrast $\gtrsim 1/10$ (Governato, Colpi & Maraschi 1994). In the latter case, it was noticed that the lower density galactic core is tidally

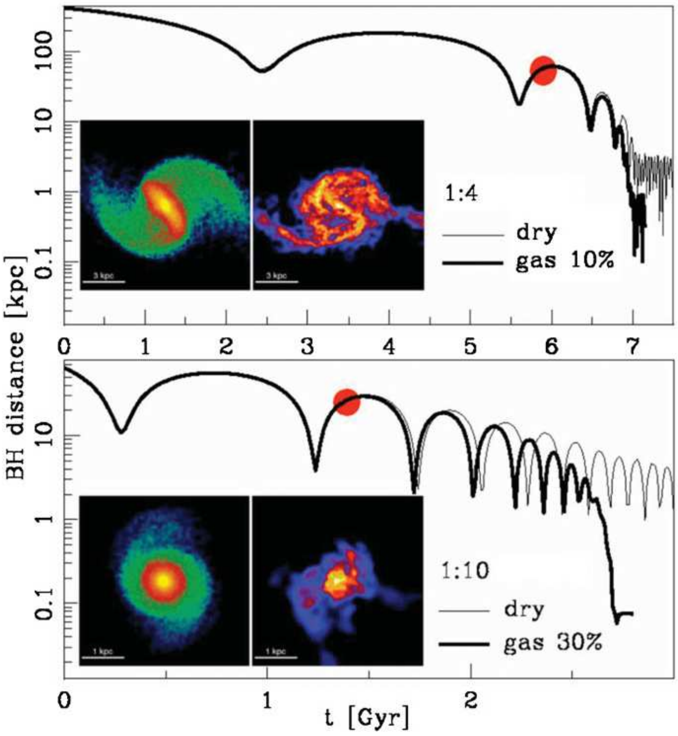

Figure 1.1: MBH separation as a function of time in four simulations of binary mergers of disk galaxies performed by Callegari et al. (2009). *Upper panel*: MBH distance for a galaxy mass ratio of 1/4; the thin and thick lines refer to a gas fraction of $f_g = 0$ (dry case) and $f_g = 0.1$ (wet case) relative to the total disk mass, respectively. The inset shows the color-coded density of stars (left) and gas (right) for the wet case at $t = 5.75$ Gyr (marked in red on the curve); each image is 12 kpc on a side, and the colors code the range $10^{-2} - 1\,\mathrm{M}_\odot\,\mathrm{pc}^{-3}$ for stars, and $10^{-3} - 10^{-1}\mathrm{M}_\odot\,\mathrm{pc}^{-3}$ for the gas. *Lower panel*: MBH distance for a galaxy mass ratio of 1/10; the thin and thick lines refer to the dry and the wet ($f_g = 0.3$) cases, respectively. The inset shows the density maps at $t = 1.35$ Gyr for the wet case; images are 4 kpc on a side (color coding as in the upper panel).

destroyed before its MBH sinks to the center of the primary galaxy. Dynamical friction is not strong enough to further brake the naked MBH that is left wandering in the outer regions of the more concentrated model. These results has been confirmed and further developed by recent numerical studies of minor mergers between disc galaxies including the effects of different amounts of gas in the two interacting galaxies, and of the accretion onto the MBHs along the pairing process. The results of Callegari et al. (2009) displayed in Fig. 1.1 show that the critical galaxy mass ratio for an efficient MBH pair formation is $\sim 1/4$ and $\sim 1/10$ for gas-poor and gas-rich mergers with gas fractions of 0.1 and 0.3 of the total disk mass, respectively. The presence of a dissipative component is necessary to preserve enough mass in the center of the lighter galaxy through ingent gas inflows that are enhanced by bar instabilities occuring in the higher galaxy mass ratio case. In this way the satellite galaxy does not get disrupted before reaching the center of the primary. Moreover Callegari et al. (2011) noticed that, depending on the initial fraction of cold gas in the galactic disks, the final mass ratio of the MBH pair can significantly change from the starting galaxy mass ratio that would result simply assuming the MBH-bulge relation. In particular, it was found that the greater accumulation of matter in the center of the satellite observed in gas-rich mergers increases both the MBH pairing efficiency and the accretion rate on the lighter hole, leading to an increase of the final MBH mass ratio up to a factor of 5.

If the MBHB manage to evolve from the stage of binary formation down to the GW inspiral domain, and if it can be effectively observed along this evolutionary path critically depends on the environmental properties, namely if it is a gas-poor or -rich merger and if there is enough matter to interact with. In Sec. 1.1 we describe the main results achieved in the modeling of the MBHB dynamics in stellar environments. In the following Sec. 1.2 we consider in more details the mechanisms acting in gas-rich systems that are at the base of the physical model we focus on in this work.

1.1 Stellar dynamics

In pure stellar systems, MBHBs evolve mainly through gravitational interactions with single stars. In close three-body encounters, stars extract energy and angular momentum from the binary and are shot out at high velocities that are enough to escape from the nucleus as the binary becomes ”hard”,i.e. its binding energy per unit mass exceeds the star specific kinetic energy, on scales below:

$$a_{\rm h} \sim \frac{G\mu}{4\sigma^2} \sim 2.7\,\frac{q}{(1+q)^2}\,M_8\,\sigma_{200}^{-2}\ {\rm pc} \tag{1.4}$$

where a_h is the binary hardening radius and $\mu = M_1M_2/M$ is the binary reduced mass (e.g. Merritt & Milosavljevic 2005). Numerical results obtained through three-body scattering experiments show that the energy carried away from ejected stars is of the order of:

$$\Delta E \approx \frac{3}{2}\frac{Gm_*\mu}{a} \tag{1.5}$$

corresponding to a decrease in the semi-major axis of $\delta a/a = \delta E/E \sim m_*/M$, where m_* is the stellar mass and E is the binary binding energy (e.g. Quinlan 1996). Fig. 1.2 shows the mass in stars that has to be ejected from a MBHB to reach coalescence for GW emission on a timescale in the range $10^8 - 10^{10}$ yr as computed by Merritt & Milosavljevic (2005) according to $M_{*,\rm ej} \sim (1/3)\, M\, ln(a_{\rm h}/a_{\rm GW})$ for $\sigma = 200$ km s^{-1} and assuming the MBH-σ relation as given by Ferrarese & Ford (2005).

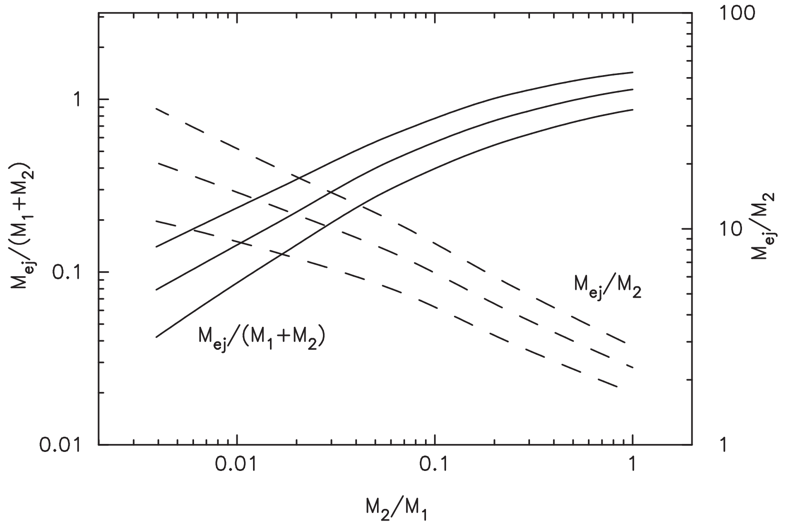

Figure 1.2: Mass in stars ejected by a MBHB in units of the total binary mass (solid) and of the secondary MBH (dashed). The curves show the mass that has to be ejected in order for the binary to coalesce for emission of gravitational waves on a timescale of 10^{10} yr (lower), 10^9 yr (middle) and 10^8 yr (upper) assuming $\sigma = 200$ km s^{-1} and the MBH-σ relation by Ferrarese & Ford (2005) (Merritt & Milosavljevic 2005).

Moreover considering an interaction rate of $\Gamma = (\rho_*/m_*)A\sigma$, where ρ_* is the nuclear stellar density and $A \sim \pi a(GM/\sigma^2)$ is the binary cross section corrected for gravitational focusing, the hardening timescale results to be:

$$t_{\rm H} \sim \frac{\sigma}{\pi G \rho_* a} \sim 1.4 \times 10^9 \left(\frac{\sigma}{200\,{\rm km\,s^{-1}}}\right) \left(\frac{10^4 {\rm M_\odot\,pc^{-3}}}{\rho_*}\right) \left(\frac{10^{-3}{\rm pc}}{a}\right) {\rm yr} \quad (1.6)$$

Eq. 1.6 thus expresses the time that a MBHB would take to reach a separation a starting from larger distances when interacting with a fixed stellar background.

The simple description given above does not take into account that there is a limited number of stars on orbits with a pericenter distance from the MBHB within a few times the binary semi-major axis. These stars define the so called loss cone in the stellar phase-space.

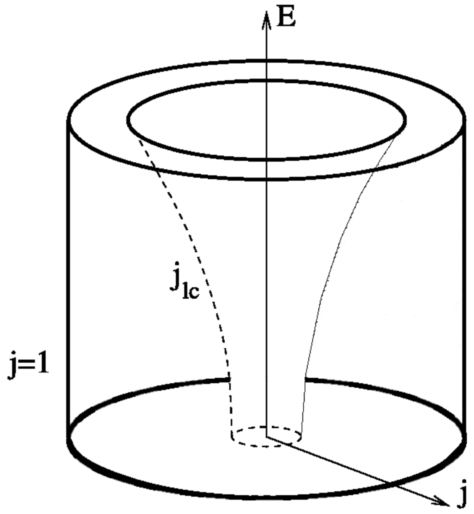

Figure 1.3: Schematic representation of the loss cone. j is the angular momentum of a star with energy E divided by the angular momentum of a circular orbit with the same energy. $j_{\rm lc}$ refers to a star passing by the MBHB at a pericenter distance equal to the binary semi-major axis. Stars at greater distances (i.e. with smaller E) have to be on more radial orbits (i.e. with smaller j) in order to intercept the MBHB (Milosavljevic & Merritt 2003b).

Fig. 1.3 gives a geometrical representation of the loss cone in the $E-j$ plane where j is the angular momentum of a star with energy E in units of the angular momentum of a circular orbit with the same energy (Milosavljevic & Merritt 2003b). Several N-body simulations have confirmed that in spherical systems the mass in stars enclosed in the loss cone is not enough to reach $a_{\rm GW}$. Then the MBHB ejects all the stars in the loss cone once reached separations of the order $\approx a_{\rm h}$. After the loss cone is emptied, the binary hardening rate is given by the timescale of loss cone refilling. This timescale is determined by two-body relaxation processes that are strongly affected by the geometry and the dynamics of the stellar nucleus. For spherical systems the two-body relaxation timescale is longer than the Hubble time leading to the so called last-parsec problem (e.g. BBR, Makino & Funato 2004). In the last years several alternatives have been investigated in order to overcome this obstacle in the MBHB evolution towards the rapid phase of GW inspiral:

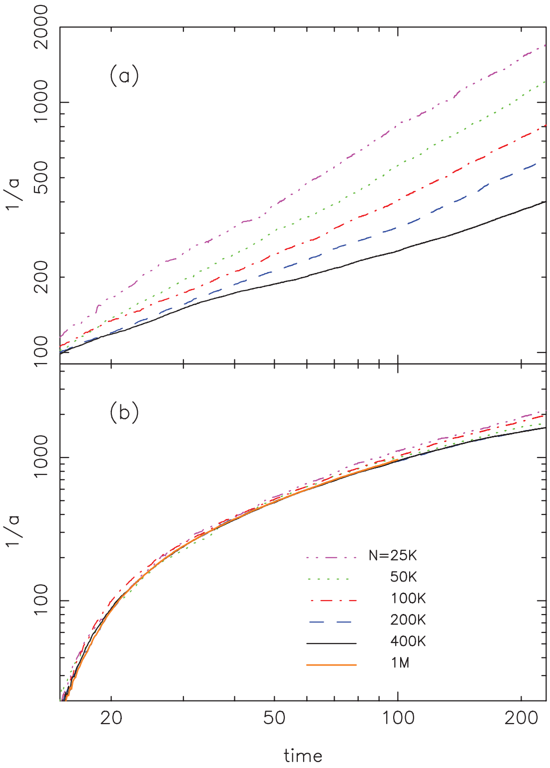

Figure 1.4: Evolution of the inverse of the binary semi-major axis $1/a$ in a set of N-body simulations with different total particle number N performed by Berczik et al (2006). The upper panel (a) refers to spherical, non-rotating galaxy models and the results show a clear dependence on N. This is not observed in panel (b) that refers to flattened, rotating galaxy models.

triaxial nuclei with a much greater number of stars populating the binary loss cone relative to the spherical case (e.g. Merritt & Poon 2004); collisional nuclei where the two-body relaxation processes act on shorter timescales (e.g. Milosavljevic & Merritt 2003a); nuclei perturbed by additional components such as: giant molecular clouds and/or star clusters scattering field stars in the loss cone (Perets et al. 2007), or a third MBH infalling from a subsequent merger accelerating the hard binary coalescence as in a three-body encounter (Makino & Ebisuzaki 1994). In particular, great attention has been given to the former scenario since the stellar nucleus resulting from a galactic merger is expected to be rotating, triaxial and possibly subject to bar instabilities. In triaxial nuclei none of the angular momentum components is a conserved quantity and this results in a large population of stars on so called centrophilic orbits that can pass arbitrarily close to the MBHB (e.g. Merritt & Vasiliev 2011).

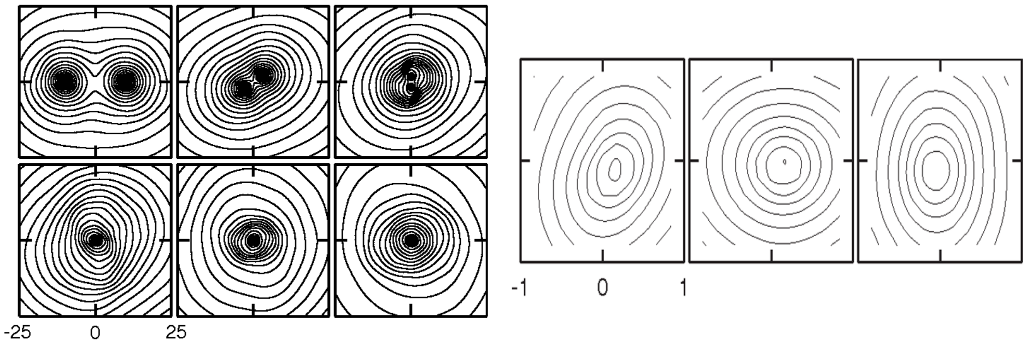

Figure 1.5: *Left*: Density contours projected on the initial orbital plane taken at different times from an N-body simulation of a merger between two spherical galaxies. The upper left panel corresponds to $t = 0$ where a MBH resides at the center of each stellar nucleus. *Right:* Zoom-in of the central region of the merger remnant after the two stellar nuclei have merged. The contours show clear departures from axi-symmetry. The different panels correspond to the projection on the xy plane (left), the xz plane (center), and yz plane (right).

As displayed in Fig. 1.4, the N-body simulations of Berczik et al. (2006) show that the MBHB hardening rate is high and does not depend on the number of particles used in the simulations when considering rotating galaxies that develop a significant triaxiality. Different groups recently began to extend the analysis of Berczik et al. (2006) to more realistic galaxy models and initial conditions through numerical simulations starting from the former phase of the merger between the two stellar nuclei (Khan, Just & Merritt 2011, Preto et al. 2011). Fig. 1.5 is from the work by Khan, Just & Merritt (2011) and shows the non-spherical shape of the remnant of a dissipationless merger between two spherical galaxies each with a central MBH. Beside the

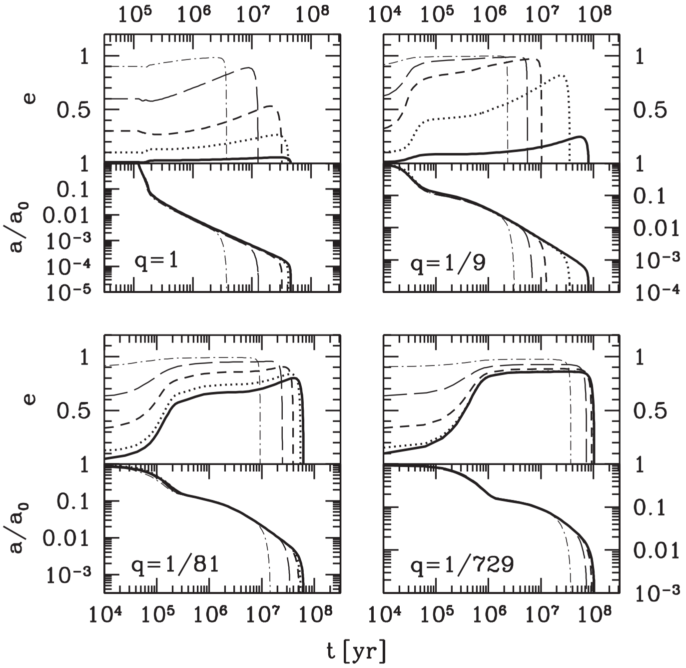

Figure 1.6: MBHB evolutionary tracks produced by the hybrid model of Sesana et al. (2010) where numerical three-body scatterings of bound and unbound stars are coupled with an analytical formalism for the evolution of the stellar density distribution. In each of the four panels, the eccentricity (top) and the semi-major axis (bottom) are plotted as a function of time. Different panels refer to different values for the binary mass ratio q. In each panel, different linestyles are for an initial eccentricity $e_0 = 0.01$ (solid), 0.1 (dotted), 0.3 (short-dashed), 0.6 (long-dashed), and 0.9 (dotted-dashed). The inner stellar cusp slope is fixed to $\gamma = 1.5$.

contraction of the orbital separation, also the evolution of the eccentricity has to be considered in predicting the MBHB fate since it can significantly increase the GW emission rate. The eccentricity variations are determined by the exchange of both the energy and the angular momentum. It is therefore mandatory to know the exact angular momentum distribution of the

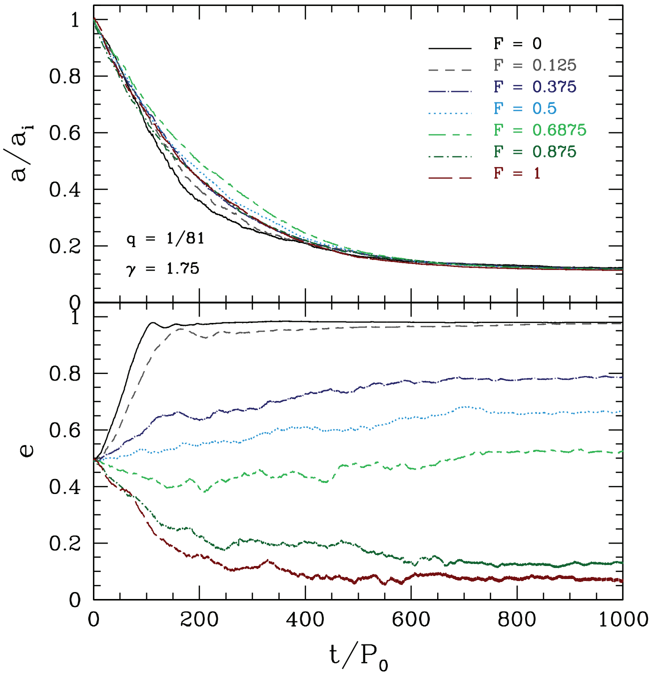

Figure 1.7: Semi-major axis (upper panel) and eccentricity evolution (lower panel) of a MBHB according to the N-body simulations performed by Sesana, Gualandris & Dotti (2011). Different lines correspond to different fractions of co-rotating stars F as labeled in the figure. The binary mass ratio is $q = 1/81$, the slope of the stellar density distribution is $\gamma = -7/4$ and the initial eccentricity is $e_i = 0.5$. P_i is the Keplerian orbital period of the binary at a_i.

stellar system interacting with the MBHB. For this reason, modeling the eccentricity evolution is more complicated and the results are more affected by the numerical noise of the N-body simulations due to the limited number of particles considered ($N < 10^6$).

As shown in the panels of Fig. 1.6, the general picture for MBHBs in bound stellar cusps with different density profiles is that equal-mass binaries on initial circular orbits tend to stay circular while MBHBs that form on eccentric orbits or have $q \ll 1$ experience a significant eccentricity growth up to $e > 0.9$ (e.g. Milosavljevic & Merritt 2001; Aarseth 2003; Baumgardt, Gualandris & Portegies Zwart 2006; Merritt, Mikkola & Selz 2007; Sesana 2010). This result can be explained considering that, because of angular momentum conservation during the gravitational encounter, stars counter-rotating with the binary extract more angular momentum relative to the co-rotating stars (e.g. Iwasawa et al. 2011).

Fig. 1.7 shows the results of direct N-body integrations performed by Sesana, Gualandris & Dotti (2011). This work shows that MBHBs tends to be circularized in rotating stellar systems with a higher level of co-rotation and viceversa. However also for the case of rotating stellar nuclei, several simulations show MBHBs with significant initial eccentricities that tend to grow during the hardening phase as in the case of isotropic systems (e.g. Berczik et al. 2006). This is probably because the binary evolution is driven mainly by the interactions with unbound stars that are diffused in the loss cone on orbits with initial low angular momentum. Future N-body simulations with an increased number of particles will be fundamental to clarify this issue.

1.2 Gas dynamics

There exist both observational and theoretical evidences indicating that the presence of cold gas can have a relevant effect on the formation and the orbital evolution of MBHBs. In numerical simulations of gas-rich major mergers, the dissipative component is subject to strong dynamical instabilities leading to ingent inflows of material in the central regions, promoting the birth of a MBHB. This kind of gravitational interactions are expected to be common in the past where the merger rate of dark matter halos and the galaxy gas fraction increase (e.g. Volonteri, Haardt & Madau 2003; Narayanan et al. 2012 and referenced therein). In agreement with this picture, observational evidences of merging systems in the local Universe hosted in dusty and star-forming environments, known as (U)LIRGs (see Ch. 3), show the presence of massive (up to 10^{10} $M_\odot$) and rotating gaseous structures extending on scales of $\lesssim 100$ pc (e.g. Sanders & Mirabel 1996; Downes & Solomon 1998; Davies et al. 2004).

The presence of a significant amount of gas in the vicinity of a MBHB is fundamental for its detectability since part of the material could be accreted by one or both components leading to electromagnetic signatures distinctive of the different stages of the orbital evolution (see Ch. 3 and 4). Being able to recognize the observational counterpart to a GW event of MBHB coalescence observed with NGO or PTA would add critical information on the host galaxy system, on the binary environment and on its evolutionary history.

In the following we will describe our current understanding of MBHBs evolving in gas-rich environments mainly through the results of several hydrodynamical simulations. Each of the considered numerical experiment is focused on a different spatial scale in order to reach the numerical resolution required to properly model the MBH dynamics. In particular, in Sec. 1.2.1 we will follow a gas-rich merger from the larger galactic scale of ~ 100 kpc until the two MBHs form a binary within a circum-nuclear disk on scales of ~ 1 pc. Then we will study the MBHB formation and orbital evolution down to sub-pc separations (~ 0.1 pc) in an already settled circum-nuclear disk. In Sec. 1.2.2 we will focus on both numerical and analytical studies of binary dynamics starting from sub-pc scales down to the GW inspiral domain soon after the MBHB has opened a central cavity in the surrounding thin circum-binary disk.

1.2.1 Binary dynamics in circum-nuclear disks

The representative case of a major merger between two Milky Way like galaxies has received the attention of several numerical works discussed in the literature (e.g. Springel et al. 2005; Kazantzidis et al. 2005). In particular, Mayer et al. (2007) realized the first set of N-body+Smoothed Particle Hydrodynamics (SPH) simulations with enough dynamical range to follow two equal-mass galaxies approaching on a parabolic orbit with a pericenter distance of 50 kpc until the two holes with 2.6×10^6 $M_\odot$ form a binary on pc scales. The spatial resolution achieved in this numerical experiment is initially of ~ 100 pc and then of ~ 2 pc in the late merger phase thanks to the particle splitting technique.

Before merging into each other via dynamical friction, the simulated galaxies (composed of an exponential disk of gas and stars, a stellar bulge and an extended dark matter halo) experience several close encounters that funnel more than half of the gas present in the initial configuration to the inner few hundred parsecs of each galactic nucleus. In this way after ~ 5.1 Gyr, the two MBHs are surrounded by two rotating, massive gaseous disks, with a radial scale of ~ 100 pc, and have reached a separation of ~ 6 kpc.

As shown in Fig. 1.8, in the higher resolution run restarted from this stage, the two cores finally merge in $\sim 2 \times 10^7$ yr and the two MBHs are found in a single self-gravitating gaseous disk (with a mass of 3^9 $M_\odot$ and

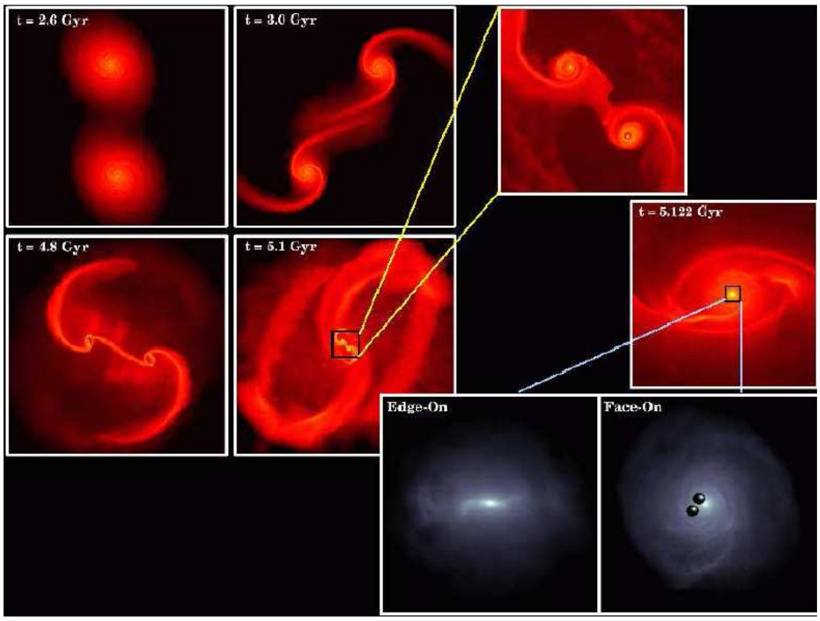

Figure 1.8: Snapshots taken at different times from a numerical simulation of a merger between two Milky Way like galaxies performed by Myer et al. (2007). The sides of the four boxes on the left, corresponding to the initial stages on larger scales, correspond to 120 kpc and 60 kpc for the top and the bottom panels respectively. The boxes on the right are 8 kpc on a side and correspond to a zoom-in of the last stages of the merger when each MBH is surrounded by a massive rotating disk (upper panel) and after the two nuclei have merged (bottom panel). The map color code shows higher gas densities with brighter colors with a logarithmic scale. The two panels in grey scale show a face-on (right) and edge-on (left) view of the nuclear disk in the inner 160 pc of the merger remnant with the location of the two MBHs highlighted with black dots.

a size of $\sim$ 75 pc) more massive than the sum of the two starting nuclear disks because of further inflows of gas. The disk is turbulent and rotationally supported ($v_{\rm turb} \sim 100$ km s^{-1} and $v_{\rm rot} \sim 300$ km s^{-1}) and it gives the dominant contribution to the mass enclosed within a few hundred parsecs from the center. The two MBHs, initially on an eccentric orbit near the plane of the disk with a separation of $\sim$ 50 pc, reach a distance comparable to the numerical spatial resolution in less than a million years. This very short shrinking timescale indicates that the dynamical friction is acting predominantly against the dense gaseous background in the supersonic regime where the gaseous gravitational drag is more efficient than in a stellar environment with the same density (Ostriker 1999).

Supported by works such those of Kazantsidis et al. (2005) and Mayer et al. (2007) and taking into account the properties of massive nuclear disks as observed in interacting systems, different authors simulated the dynamics of two MBHs with separations in the range $0.1\,\mathrm{pc} \lesssim a \lesssim 100$ pc orbiting in a self-gravitating, rotationally supported disk, composed of gas or of gas and stars, in equilibrium with a spherical distribution of stars (Escala et al. 2005; Dotti et al. 2006; Dotti et al. 2007; Dotti et al. 2009a). In order to bracket the uncertainties in the outcomes of mergers with different mass ratios and encounter geometries, the results of these higher resolution numerical experiments were tested varying: the initial binary eccentricity, the binary mass ratio, the angle between the binary orbital plane and the disk, the initial direction of the orbital motion relative to the disk rotation, the density and total mass of the disk and the polytropic index γ used to model the disk thermodynamics according to the equation $P = K\rho^{\gamma}$, where $K = const$. In agreement with Mayer et al. (2007), all these works find a rapid MBHB formation timescale, < 10 Myr, down to parsec scales with the two holes sinking faster if the disk is colder ($1 < \gamma < 5/3$ where $\gamma = 5/3$ corresponds to the adiabatic case for an ideal monoatomic gas); the binary mass and/or the disk mass is increased; the binary orbit lays close to the plane of the disk.

A relevant point discussed in the works by Dotti et al. (2006; 2007) is that the circularization of the orbit is a general effect due to the dynamical friction acting in a rotating background. As shown in Fig. 1.9, a co-rotating MBH starting with a significant eccentricity is accelerated at the apocenter, where it moves slower than the local gas, while at pericenter its velocity is reduced by the gravitational drag of the slower moving gas. The combined effect is the reduction of the eccentricity before the two MBHs bind in a Keplerian system. This result is valid independently if the disk is composed of stars or of gas and star provided that the disk rotational velocity is greater than the gas sound speed and the stars velocity dispersion.

Moreover, thanks to the high spatial resolution of ~ 0.1 pc and the large number of particles ($\sim 2\times10^{6}$) considered in the work of Dotti et al. (2009a), it has been possible to resolve the influence radius of the moving MBHs allowing the modeling of the orbital evolution of an initially counter-rotating orbit and of the accretion rate onto the holes during the orbital decay. Considering the case of two equal mass MBHs where one (referred to as secondary) is ini-

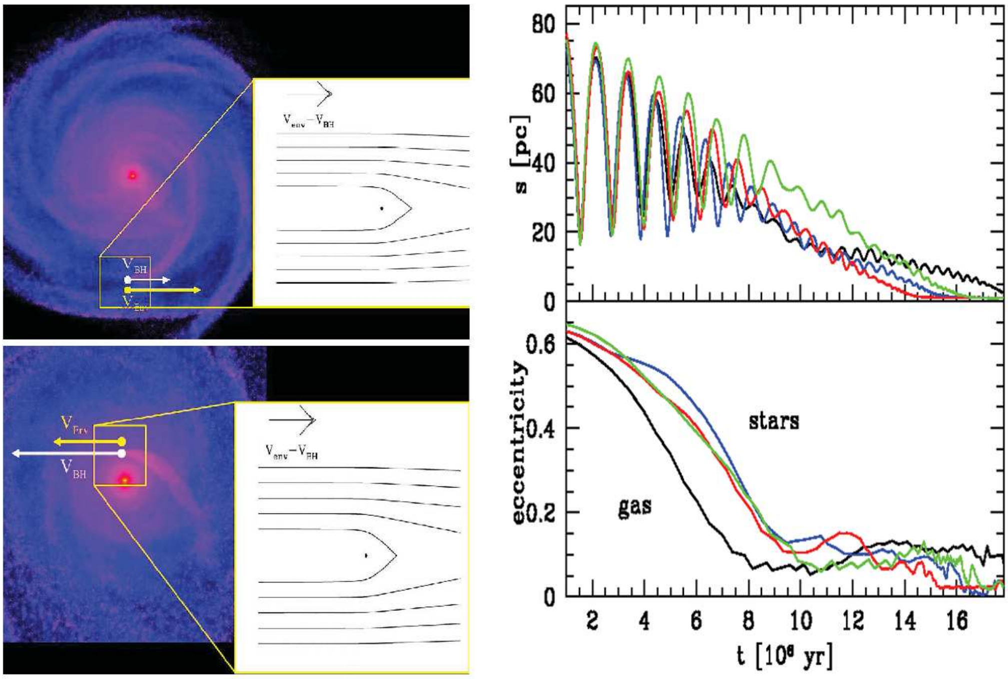

Figure 1.9: *Left:* Face-on projections of a 10^8 $M_\odot$ gaseous circum-nuclear disk simulated in the work by Dotti et al. (2007) for the case with the MBHB mass ratio $q = 1/4$, the primary MBH with 4×10^6 $M_\odot$ at rest at the center of the disk and the secondary MBH on a prograde orbit with an initial eccentricity of 0.7. The upper panel refers to the first MBH apocenter. The color coding shows the z-averaged gas density, the white and yellow arrows refer to the MBH and disk velocities, respectively. In the insert panel the trajectories of the gas particles are drawn, as observed in a frame comoving with the orbiting MBH. The density wake is in front of the MBH trail. The lower panel is for the MBH at its first pericenter. In this case the wake lags behind the MBH trail. *Right:* Separation (s) between the two MBHs and binary eccentricity as function of time for different simulation runs with a MBHB mass ratio $q = 1/4$. Black, blue, red and green lines refer to stellar to total disk mass ratio of 0, 1/3, 2/3, and 1, respectively.

tially on a counter-rotating orbit while the other (called primary) is placed at rest at the center of the disk (see the right panels of Fig. 1.10), it has been found that on a timescale of ∼ 2 Myr the orbital angular momentum changes sign, called angular momentum flip, and the secondary co-rotates with the disk before the MBHB formation. This effect is due to the action of the dynamical friction reducing the secondary MBH velocity at each orbital phase as long as the MBH direction is anti-aligned relative to the gas flow.

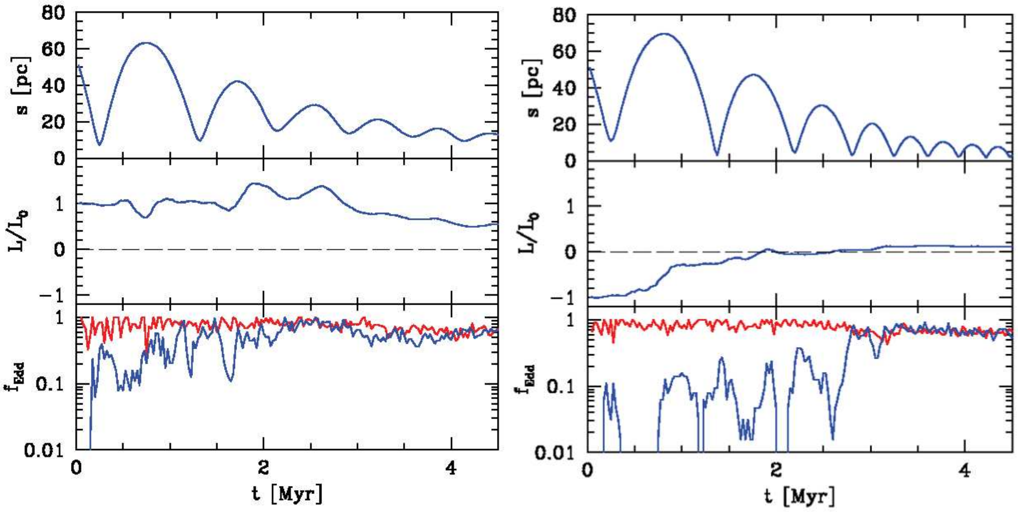

Figure 1.10: Results taken from the simulation by Dotti et al. (2009a) of an equal-mass MBHB embedded in a gaseous circum-nuclear disk with one of the two MBHs, called primary, at rest at the center of the disk and the other MBH, called secondary, on an initial eccentric orbit. The panels on the left(right) are for a secondary MBH on a prograde(retrograde) orbit. Upper panels: MBH separation as a function of time. Middle panels: time evolution of the orbital angular momentum of the secondary MBH (L) normalized to its initial value (L_0). The thin-dashed horizontal line marks $L = 0$. Lower panel: Eddington ratio as a function of time. Red and blue lines refer to the primary and the secondary MBH, respectively.

The results obtained in the analysis of the accretion rate onto the MBHs on both counter and co-rotating eccentric orbits are displayed in Fig. 1.10 and show that both MBHs can be active with variable Eddington ratios ($f_{\rm Edd}$) on a timescale of a few Myr when the two holes orbit at a distance of $\gtrsim 10$ pc. In general, the accretion rate on the secondary MBH is lower and has greater variations, especially in the counter-rotating case or for co-rotating eccentric orbits, because of fast variations in the relative velocity between the gas and the secondary MBH that reduce its influence radius, of gas inhomogeneities near the secondary, and of the finite number of gas particles that do not allow to always resolve the influence radius of the secondary MBH in the counter-rotating case. However the secondary MBH reaches a more constant and higher level of accretion, comparable to that of the primary ($f_{\rm Edd} \sim 0.9$), after the orbit circularization and the angular momentum flip for a retrograde orbit. According to Dotti et al. (2009a), the strong effects on the accretion rate of the secondary MBH related to its motion on eccentric and/or retrograde orbits could play a relevant role in determining the number of double AGN systems detectable in circum-nuclear disks.

1.2.2 Binary dynamics in circum-binary disks

The numerical simulations described in the previous section show that two MBHs bind in a Keplerian binary on a timescale $\lesssim 10^7$ yr inside a self-gravitating nuclear disk formed in the last stage of a major gas-rich merger. In these calculations the gas is treated essentially as a one-phase medium evolved with an effective equation of state whose polytropic index can be changed to mimic different degrees of radiative cooling efficiency (e.g. Spaans & Silk 2000). More realistic simulations that include directly the effect of star formation and feedback from supernovae explosions and accretion onto the MBHs would actually reveal the presence of a multi-phase, clumpy and turbulent medium (e.g. Wada & Norman 2001). However the basic prediction of an efficient MBH pairing process is expected to remain valid. The MBHs bind in a Keplerian binary on a short timescale compared to that of the star formation expected in the simulated nuclear regions while the additional amount of energy injected by supernovae and by the two active MBHs are likely to be significantly lower than the internal energy of the disk (e.g. Mayer et al. 2007 and references therein).

The above considerations do not hold for orbital separations $\lesssim 1$ pc. On these spatial scales the gravitational potential in the vicinity of the two holes is dominated by that of the newly formed MBHB. As already noticed by Escala et al. (2004, 2005) and Dotti et al. (2006), from this time on dynamical friction acting individually on the MBHs is no more efficient and the orbital decay rate is determined by the response of the surrounding gaseous distribution, called circum-binary disk, to the gravitational interaction with the MBHB. The details of the gas dynamics and thermodynamics on sub-pc scales, that are ultimately connected with that of the larger scale structure, become fundamental to assess the MBHB fate. The circum-binary disk properties indeed affect the balance between the gravitational and the viscous torques that possibly lead to the clearing of a central cavity in the circum-binary disk (see below for further discussions), and determine the amount of material that the MBHB can effectively interact with. In the following we will present the results on the latest stage of the MBHB evolution obtained in analytical and numerical works considering different possible scenarios for the still debated binary-disk interaction.

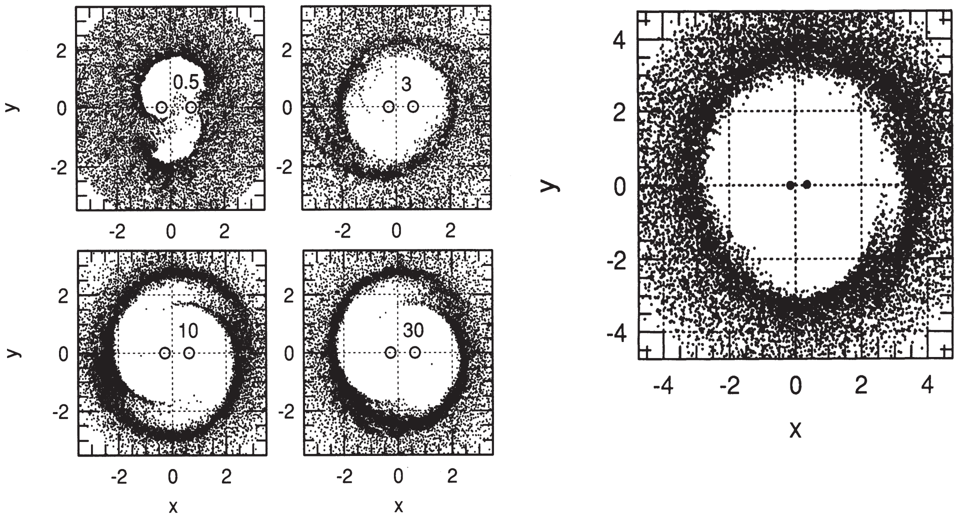

Figure 1.11: Maps of the locations of the SPH particles used to simulate a circum-binary disk around a MBHB with mass ratio $q = 0.3$ in the work of Artymowicz & Lubow (1994). *Left:* Gap evolution for a MBHB with eccentricity $e = 0.1$. The distances in the maps are given in units of the binary semi-major axis. The four panels refer to different times that are indicated in the labels in units of the binary orbital period P. At time $t = 0$ the disk had a uniform surface density distribution. The binary components are shown as circles. A gap extending over $r \approx 2.3a$ surrounds the MBHB in the time-steady configuration shown in the lower left panel. *Right:* Same as for the maps shown in the panels on the left but for a MBHB with $e = 0.5$. The gap radial size is $r \approx 2.8a$. The map corresponds to $t = 50P$.

The excavation of a low density region surrounding the MBHB, referred to as gap, can be basically described drawing an analogy with the effect of the dynamical friction driving the orbital decay of the two MBHs in the circum-nuclear disk. The key concept is indeed the transfer of angular momentum from the binary to the circum-binary disk through gravitational interactions.

Consider for simplicity an unequal mass binary system similar to the condition of a planet (M_1) orbiting around a more massive companion (M_2)

within a protoplanetary disk. In this case, the material located outside the orbit of M_2 is pushed towards higher angular momentum orbits at larger radii because of the breaking drag exerted onto the faster moving MBH (assuming a Keplerian rotation curve). On the contrary, the interaction with the gas inside the orbit of the secondary accelerates the slower moving MBH, bringing the gas on lower angular momentum orbits at smaller radii. So the presence of M_2 affects the disk trying to remove the gas from an annular region around the hole. On the other hand the response of the pressure and the viscous torques acting between the gas particles in the disk tends to fill again the emptied annular region. Then a gap annulus of size Δr will be opened and maintained around the secondary MBH, orbiting around M_1 at a radius r, if:
(i) Δr is greater than the Roche lobe of the MBH (see Sec 3.2.1 for a definition) ensuring that the the exchange of angular momentum between the gas and the MBH occurs not only through the accretion of material but mainly through the gravitational interaction with the gas at the edge of the gap;
(ii) the vertical scale height of the disk is lower than the gap size preventing the gap closure by the disk pressure gradients;
(iii) the gap-closing timescale $t_{\rm close}$ results to be longer than the gap-opening timescale $t_{\rm open}$.
The closing timescale can be computed as the ratio between the gap size and the radial drift velocity of the gas in the disk, i.e. $t_{\rm close} \sim \Delta r/v_{\rm drift}$ where $v_{\rm drift}(r) \sim \nu/r$ for a standard thin disk whose kinetic viscosity coefficient is parameterized as $\nu \sim \alpha c_s H$ where α is the adimensional viscosity constant, c_s is the gas sound speed and H is the disk vertical thickness (Shakura & Sunyaev 1973). The gap-opening timescale is of the order of $t_{\rm open} \sim \Delta L/\dot{H}$ where $\Delta L \sim r^3 \Delta r \Sigma \Omega$ is the angular momentum that has to be added to the gas in order to open an annular gap of size Δr in the disk with surface density Σ and Keplerian orbital frequency $\Omega = \sqrt{(GM_1/r^3)}$, and $\dot{H}$ is the angular momentum exchange rate due to the gravitational interaction between the gas and M_2. The simplest derivation for $\dot{H}$, valid for small q, is based on the assumption that the tidal torque exerted by the secondary MBH on the disk particles can be felt only during close gravitational encounters that deflects the particles circular orbits by a small angle. In this limit, Lin & Papaloizou (1979) obtain that $\dot{H} \sim G^2 M_2^2 \Sigma / r^2 \Omega^2 q$. Hence the condition in (iii) implies the relation $q > \mathscr{R}^{-1}$ where $\mathscr{R} \sim r^2\Omega/\nu$ is the disk Reynolds number, i.e. the ratio between the viscous time ($t_\nu \sim r^2/\nu$) and the disk orbital time ($t_{\rm dyn} \sim 1/\Omega$). The Reynolds number depends on the details of the disk

structure and can be $\gg 10^2$ for the standard thin models. Hence the three conditions listed above are generally satisfied by MBHBs with not-extreme mass ratios embedded in thin circum-binary disks.

Several analytical and numerical works extended the simplified analysis presented above to comparable mass and eccentric binaries showing that hat the gas distribution of the outer disk is more perturbed for higher mass ratios and eccentricities. As show in Fig. 1.11, the results of Artymowicz & Lubow (1994) obtained for protoplanetary systems with different q and e indicate that the gap region is opened in a short period (typically a few tens of binary orbits) compared to the viscous timescale and that the radial extent of the gap surrounding the binary is $R_{\rm gap} \sim 2a$ for $q \gtrsim 10^{-2}$ and $e \lesssim 0.1$, and $R_{\rm gap} \sim 3a$ for $e \sim 0.2 - 0.7$.

The evolution of the binary parameters after the rapid gap-opening phase is regulated by the same balance between the tidal and the viscous torques that determines the size of the central cavity. In order to reach the GW-driven orbital decay regime, the MBHB needs to interact with a distribution of matter able to absorb most of its orbital angular momentum. This condition is automatically verified if additional gas is always supplied to the disk along the binary orbital evolution. In this scenario of a virtually infinite disk, the migration timescale remains of the order of the viscous timescale as far as the unperturbed disk mass contained within the binary orbit is $\lesssim M_2$. At this point, the gas inflow rate is not high enough to further reduce the binary angular momentum and so the migration timescale increases.

As first noticed by Syer & Clarke (1995) and Ivanov, Papaloizou & Polnarev (1999; IPP hereafter), the slowdown of the binary decay implies an increase in the disc surface density outside the orbit of the secondary MBH. The subsequent orbital evolution can be speeded up again depending on the amount of matter accumulated close to the disk inner edge that interacts directly with the secondary MBH. In particular, IPP obtain that the migration timescale is of the order of:

$$t_{\rm decay} \sim S^{\delta}\, t_{\nu} \tag{1.7}$$

where $S > 1$ is the ratio between the mass of the secondary MBH and the disk mass inside the initial binary orbit, and $\delta > 0$ depends on the assumed disk model, namely on the form of its viscosity (e.g. $\delta \sim 0.74$ for a standard α-disk assuming that the opacity is dominated by Thompson scatterings). IPP adopt a disk model such that the Toomre parameter is always ≥ 1

allowing the disc to be gravitationally stable in the region affected by the interaction with the secondary MBH.

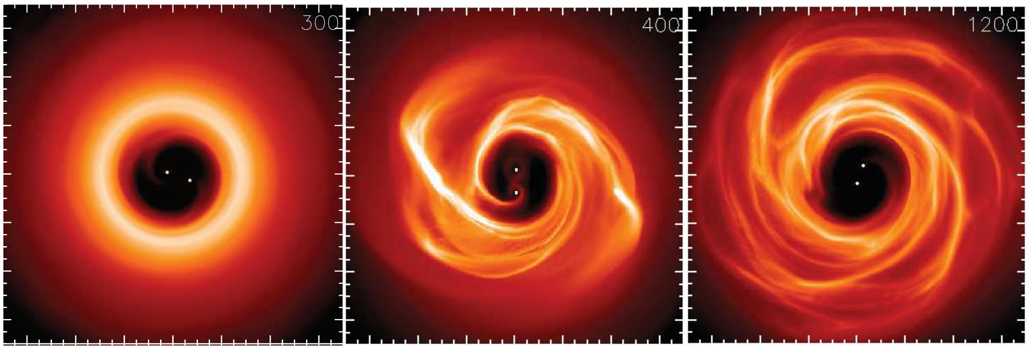

Figure 1.12: Logarithmic maps of the circum-binary disk column density projected on the xy plane at different times during the SPH simulation performed by Cuadra et al. (2009) for the case of a MBHB with mass ratio $q = 0.3$ and a binary-disk mass ratio of 0.2. The squared boxes have a side length of $6a_0$. The colors of the maps code the colum density range $10^{-4.5} - 10^{-2}\, M a_o^{-2}$ going from black to white. Until $t \approx 350\Omega_0^{-1}$, where $\Omega_0 = \sqrt{(GM/a_0^3)}$, material piles up at $R \approx 3a_0$, as a result of the gravitational torques from the binary and the disk itself, forming a dense ring. Then the ring breaks due to its self-gravity, a spiral pattern develops, and the disk stays in that state until at least $t \approx 1200\Omega_0^{-1}$, when the simulation ends.

More recently Cuadra et al. (2009; C09 hereafter) consider that self-gravity is expected to dominate the circum-binary disk dynamics at radii of the order of 0.1 pc. Therefore C09 follow the computation by IPP to derive an estimate of the binary migration timescale for the case of self-gravitating disks. In particular, C09 consider the case of a quasi-stable circum-binary disk where the angular momentum is transported outward by self-gravitating spiral arms as shown in Fig. 1.12. The analytical expectations are found to be in good agreement with the results of high resolution SPH simulations up to the point where the circum-binary disk moves away from the MBHB making the interaction less efficient and leading to a stalling of the binary orbital evolution. This effect is attributed to the finite mass of the simulated disk, of the order of $0.2M$, that is not able to absorb enough binary angular momentum in order to bring the two MBHs down to coalescence.

Following again IPP, C09 compute the rate of orbital decay due to a self-gravitating disk with the maximum surface density that can be sustained without undergoing fragmentation. This rate corresponds to an upper-limit for the binary decay and results to be faster for smaller binary separations. In particular, dens circum-binary disks could drive the coalescence of two MBHs in less than a Gyr starting from $a \lesssim 0.1$ pc only if $M \lesssim 10^7$ $\mathrm{M}_\odot$.

The numerical simulation performed by C09 allows to study also the evolution of the binary eccentricity and to quantify the rate at which the gas is able to peel off the inner edge of the circum-binary disk flowing onto the MBHs in the gap region. The non-axisymmetric torque exerted by the rotating MBHB onto the surrounding gas leads to an increase of the binary eccentricity and to the formation of tidal streams bringing the gas from the disk close to the binary where it bounds to the single MBHs (Fig. 1.12). In order to prevent the numerical calculation to become too slow, gas particles are accreted from either MBH (i.e. removed from the numerical simulation) at a distance shorter than a fixed sink radius (of the order of $\sim 0.1a$). The eccentricity growth does not saturate till the end of the numerical experiment although slowing down with time because of the less efficient coupling with the expanding circum-binary disk. Moreover the accretion rate shows a variability on the orbital timescale and overall is higher for the secondary MBH since it orbits closer to the inner edge of the circum-binary disk with a smaller velocity relative to the denser reservoir of gas.

The trends in the evolution of the binary orbital parameters and the possibility of a variable inflow of material trough the disk inner edge discussed by C09 are in general agreement with the results obtained in different analytical and numerical works (Armitage & Natarajan 2002,2005; Hayasaki et al. 2007,2008; MacFadyen & Milosavljevic 2008; Hayasaki 2009; Lodato et al. 2009; Nixon et al. 2011; Rödig et al. 2011; Shi et al. 2012; Rödig et al. 2012). In particular, Rödig et al. (2011; R11 hereafter) performed SPH simulations of MBHBs with different initial eccentricities embedded in self-gravitating circum-binary disks to understand if the eccentricity growth saturates or if it can lead to $e \approx 1$, where the GW emission would dominate the orbital decay. As shown in the left panels of Fig. 1.13, the conclusion of R11 is that there exists a limiting value for the binary eccentricity corresponding to $e_{\rm crit} = 0.66\sqrt{ln(\delta - 0.65)} + 0.19$, where $\delta \sim R_{\rm gap}/a$, so that $0.55 < e_{\rm crit} < 0.79$ for $2 < \delta < 2.5$, consistently with the results of the numerical simulations. The analytical expression of $e_{\rm crit}$ is obtained considering that the eccentricity grows because of the larger deceleration exerted by the outer disk onto the secondary MBH near apocenter as far as the angular velocity of the secondary is larger relative to that of the gas in the disk.

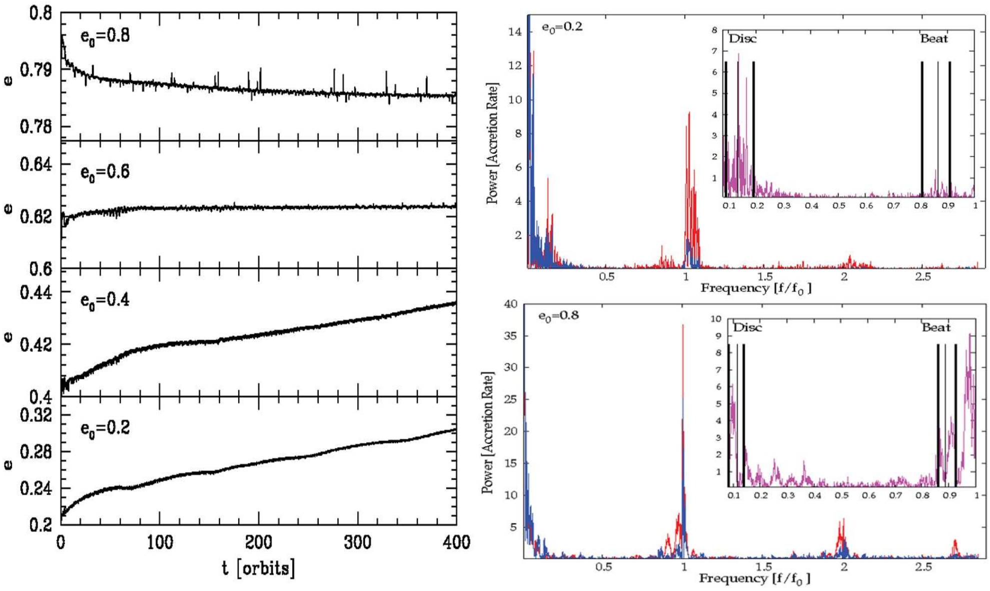

Figure 1.13: *Left:* Eccentricity evolution from the SPH simulations performed by Rödig et al. (2011) of a MBHB with mass ratio $q = 1/3$ embedded in a circumbinary disk of mass $M_{\rm disc} = 0.2M$. The four panels refer to four different runs starting from $e_0 = 0.2, 0.4, 0.6, 0.8$ bottom to top. *Right:* Power spectrum of the accretion rate (in arbitrary units) onto the primary (blue) and secondary (red) MBH for $e_0 = 0.2$(top) and $e_0 = 0.8$(bottom). Frequencies are in units of the initial binary orbital frequency f_0. The inlays show zoom-ins of the power spectra, in the frequency range $0.1 - 1 f_0$ computed summing the accretion rate from the two MBHs (pink). The expected intervals for the disk and the beat frequencies are marked by the thick vertical black lines, as indicated in the labels, and are associated respectively with the rotation of the densest part of the disk and with the difference between the binary and disk rotation.

The theoretical prediction for $e_{\rm crit}$ given by R11 is considered a conservative estimate for the eccentricity evolution. The larger values of $e_{\rm crit}$ predicted for wider gap regions excavated by eccentric binaries could not be actually reached because (i) the gravitational interaction becomes less efficient as the disk moves away from the MBHB, and (ii) the acceleration imparted onto the secondary MBH at pericenter by the gas bound to the primary MBH (neglected in the analytical derivation) tends to circularize the orbit and becomes more relevant for smaller pericenter distances, i.e. for higher eccentricities. Additionally, R11 notice that the accretion rates onto the MBHs show a periodicity at different frequencies corresponding to the orbital motion, to the rotation of the densest part of the disk and to the difference between the binary and the disk rotation. Moreover these periodic signals become more visible for higher eccentricities as shown in the right panels of Fig. 1.13.

The possibility of a time-varying disk mass has been considered in the work of Lodato et al. (2009; L09 hereafter) where the circum-binary disk has a finite mass of gas that is allowed to form stars when it becomes self-gravitating. The consumption of a limited reservoir of gas by the star formation can significantly affect the binary decay timescale if the gas mass left in the disc becomes too low, as already noticed by C09. L09 explore the case where the energy feedback from the star formation process keeps the disk close to marginal stability (Toomre parameter ~ 1). Thus the rate at which new stars are formed is determined by the balance between the corresponding energy input and the disk internal heating. Adopting this simple thermal feedback model, L09 show that the star formation process is too efficient to leave enough gas in the disk in order to assist the MBHB merger in a reasonable amount of time unless $q \sim 0.001$ or the starting orbital separation is already $a < 0.01$ pc (assuming $M_1 = 10^8$ M$_\odot$).

At this point it is important to stress that all the above considerations refer to the case of a MBHB surrounded by a co-planar, prograde circum-binary disk, i.e. co-rotating with the binary. The disk mid-plane is typically assumed to be aligned with the orbital plane because of the torque exerted by the gravitational field of the MBHB (e.g. IPP). However Nixon et al. (2011; N11 hereafter) studied the dynamical effects induced by a co-planar, counter-rotating circum-binary disk.

Retrograde disks are not expected in the standard picture of a gas-rich merger where the two MBHs are forced to co-rotate with the gas of a massive circum-nuclear disk (see Sec. 1.2.1) and the prograde MBHB formed on pc scales is efficiently driven down to coalescence thanks to the exchange of angular momentum with an adequate amount of gas. However the binary orbital evolution can be quite different if most of the gas in the disk is quickly consumed by star formation, as hinted by L09, or if in a dry-merger there is not enough cold gas to interact with and the properties of the stellar nucleus does not allow an efficient binary merger. In these cases N09 consider that the formation of a counter-rotating disk due to a randomly oriented accretion event could be more likely.

In contrast with the prograde case, the gravitational interaction with the counter-rotating disk exerts a braking drag both on the MBHs and the gas. Hence both the MBHs and the disk inner edge move inwards and the binary orbital angular momentum is decreased by the direct summation of the negative angular momentum of the counter-rotating gas that binds to the MBHs. The main results of N09 show that MBHBs starting with $e \gtrsim H/R$, where H/R is the disk aspect ratio, develop a significant eccentricity up to $e \sim 1$ just before coalescence once the secondary MBH has captured a disk mass comparable to its own. The eccentricity growth is explained with a simple argument. N09 assume that the secondary MBH interacts with the disk mostly at apocenter where the radial velocity of the MBH is zero before and after the interaction so that the apocenter distance remains constant. The interaction with the counter-rotating gas always decreases the binary angular momentum and so its semi-major axis. Then the eccentricity has to grow since $a_{\rm apo} = a(1 + e)$ is fixed. Therefore retrograde disks can efficiently lead to binary mergers since the binary shrinks while remaining in close contact with the gas that keeps on flowing at a significant rate especially onto the secondary MBH. However also in this case the key parameter is the available amount of matter since the disk mass required to coalesce the binary is still $\gtrsim M_2$. As pointed out by N09, interacting with a retrograde disk could be a very promising mechanism for lower mass ratios systems, with $q \lesssim H/R$, where the disk mass is enough to reach coalescence and remains also within the limit to keep the disk gravitationally stable.

The arguments discussed so far show how the analytical and numerical works of the last decade improved our understanding of the dynamics of MBHBs interacting with circum-binary disks. However as these investigations go into more depth, we become aware of the complexity lying in the details of the binary-disk connection that still need to be clarified to firmly assess the final fate of the binary. This has been pointed out by works devoted to a comprehensive analysis of the disk-binary gravitational coupling (Rödig et al. 2012; Shi et al. 2012; MacFadyen& Milosavljevic 2008). In particular, Rödig et al. (2012; R12 hereafter) performed several SPH simulations of a MBHB embedded in a self-gravitating circum-binary disk to study the dependence of the binary parameters evolution on the different torques exerted by: the outer disk structure, the mass inflow towards the gap region and the gas orbiting within the two MBHs that is accreted when reaching a separation shorter than a fixed sink radius from either MBH.

As shown in Fig. 1.14, R12 consider that the mass flowing into the gap

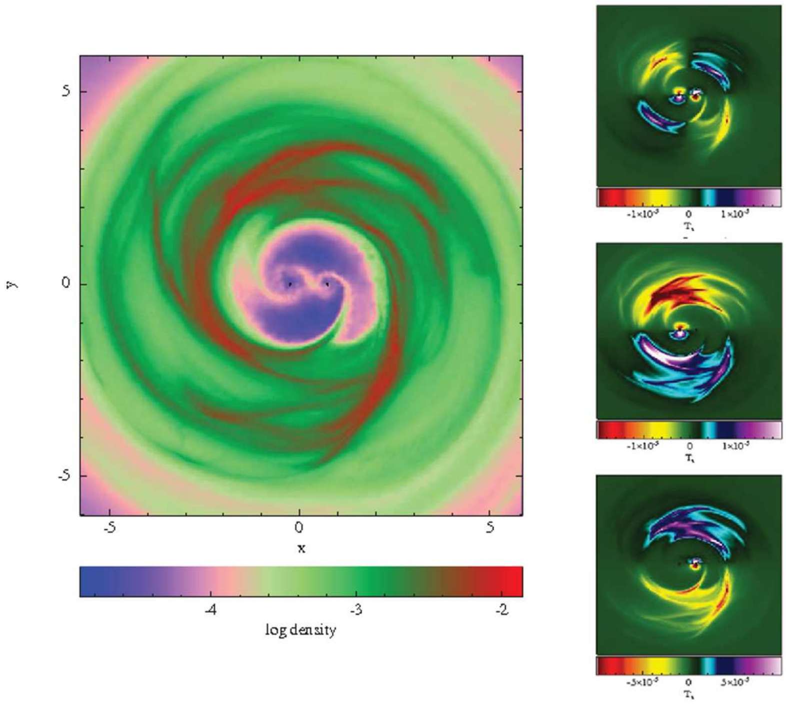

Figure 1.14: *Left*: Snapshot taken from the simulation of a MBHB orbiting in the gap region of a circum-binary disk performed by Rödig et al. (2012). The disk is shown face-on and the color code of the surface density map is present on the bottom side. *Right*: Surface density plot of the z-component of the torque exerted onto the MBHB (upper), the primary MBH (middle) and the secondary MBH (lower). These plots refer to the adiabatic case where the gas streams are clearly visible in the gap where they exert a negative torque when lagging behind the MBHs (yellow tails) and a positive torque when bending in of them (blue horseshoe-shaped contours) .

plays an important role exerting a net negative torque when the MBHs are braked by the trailing streams ripped off the disk inner edge, and on the contrary a net positive torque when the inflows reach the MBHs at super-Keplerian velocities and bend in front of them. R12 notice that the accretion of matter can further complicate this picture since the binary angular momentum increases with the binary mass so that the semi-major axis can shrink even if the total torque acting on the binary is positive and the eccentricity is excited by the interaction with the disc (see eq. 5 of R12).

Overall the major effect on the long-term binary evolution is determined by the balance between the negative and the positive torques due to interaction with the inflowing matter. This torque balance is a sensitive function of the equation of state adopted for the gas in the gap region. In particular, the adiabatic case shows a strongly disturbed disk inner edge profile and more pronounced tidal streams that are effective in shrinking the binary separation contrary to what observed in the isothermal case. However R12 consider that the linear extrapolation of the results from all simulations agree on a rapid coalescence timescale ($< 10^7$ yr for $M \sim 10^8$ $\mathrm{M}_\odot$ and $a \sim 0.1$ pc) but in order to be conclusive this result has to be tested considering: more realistic models for the gas thermodynamics; the feedback from the accreting MBHs that could affect the amount of matter and of angular momentum that is transferred to the binary; and possibly the long-term effect due to the external fueling of the disk.

Chapter 2

Observational signatures of MBH pairs and binaries

In this Chapter we describe the most relevant observational properties of different type of systems selected as potential hosts of MBH pairs in the course of a galaxy encounter or of MBHs bound in binary systems in the final stages of a merger. These sources are detected because at least one of the two MBHs is active and are distincted in spatially resolved and unresolved systems. The former are presented in Sec. 2.1 and are observed thanks to the high spatial resolution of optical and X-ray space satellites and to the radio interferometric technique. With the exception of a Keplerian binary at a projected separation of ~ 7 pc, most of the resolved systems are characterized by large separations, of the order $100\,\mathrm{pc} \lesssim d \lesssim 10$ kpc, and are referred to as Dual AGN systems, i.e. two MBHs not physically bound in a binary whose dynamics is determined by the gravitational potential of the interacting host systems.

Current observational capabilities are not enough to resolve true binary systems orbiting on sub-pc scales. The highest spatial resolution, $\gtrsim 1\,\mathrm{mas}$, achievable by means of the radio interferometers corresponds to a spatial scale $\gtrsim 1$ pc at $z \gtrsim 0.05$. Moreover this radio technique is not suited for wide surveys due to the limited field of view and requires that both MBHs are luminous in the radio band. To overcome these limitations, we have to rely on electromagnetic signatures associated with binary systems that can be probed with other techniques such as variability studies and spectroscopy. The results obtained with the two aforementioned observational approaches are discussed in Sec. 2.2. In particular, Sec. 2.2.2 deals with a first group of spectroscopic MBHB candidates characterized by an optical spectrum with double-peaked emission line profiles. We postpone to the next Chapter a more detailed description of a second class of spectroscopic candidates that represents the focus of the work presented in this thesis.

2.1 Resolved systems

2.1.1 Large separation MBH pairs

Until now a few tens of dual AGN systems have been detected with a variety of observational signatures depending on the dynamical stage of the merger when they are observed and on the properties of the systems involved, i.e. if it is a dry or a wet merger occurring between gas-rich or gas-poor galaxies respectively.

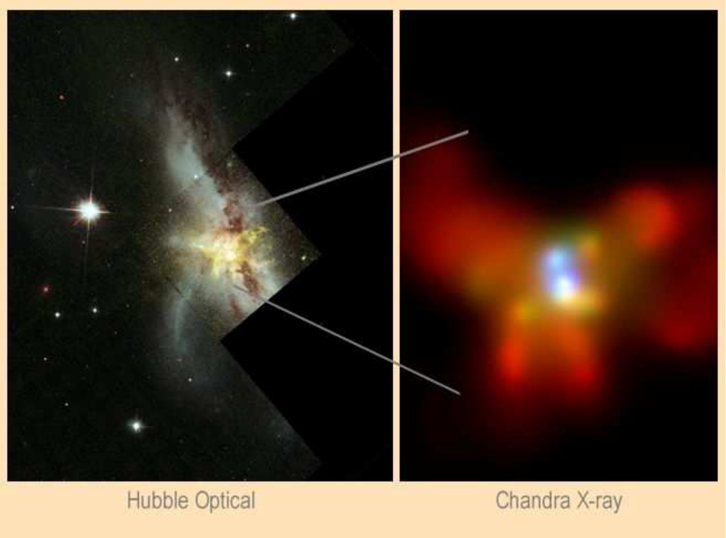

Figure 2.1: *Left*: optical image from the Hubble Space Telescope of the complex morphology of the two interacting galaxies in NGC6240. The gas filaments perpendicular to the dust lane visible against the main body of the systems are probably due to a sturburst superwind. (Gerssen et al. 2004). *Right*: Chandra X-ray image of the inner regions of NGC6240 with two resolved active nuclei at a projected separation of 700 pc (Komossa et al. 2003).

A double active nucleus has been observed in at least three (U)ltra Luminous Infrared Galaxies ((U)LIRGs) which consist of a pair of interacting gas-rich spirals embedded in a dusty and star-forming environment. The bolometric luminosity of (U)LIRGs is indeed dominated by the dust emission in the infrared band, powered by an intense star-burst.

Fig. 2.1 shows optical and X-ray images of **NGC 6240**. This is a well known and studied ULIRG located at $z = 0.0243$ with two optical nuclei at a projected separation of $\simeq$ 800 pc and a velocity difference along the line of sight of $\sim 150\,\mathrm{km\,s^{-1}}$ (e.g. Fried & Ulrich 1985). High resolution observations obtained by Komossa et al. (2003) with the Chandra satellite confirmed the presence of two compact X-ray sources spatially coincidents with the optical and IR nuclei. The detection of a strong iron line in both nuclei is a clear signature of the presence of two accreting MBHs. Observations in the hard X-ray band ($\gtrsim$ 9 keV) revealed that the intrinsic AGN emission is much greater than what obtained in the soft band due to significant dust absorption (e.g. Vignati et al. 1999). Studies of the gas and stellar kinematics in the inner regions ($<$ 500 pc) of this complex system show that each active MBH is surrounded by a rotating stellar disk whose dynamics is decoupled by that of a massive, molecular gas disk located in between the two nuclei (Tacconi 1999, Tecza et al. 2000, Eisenhauer et al. 2004). According to Tecza et al. (2000), the observational properties of NGC 6240 are compatible with a scenario where, although not yet gravitationally bound, the two nuclei are caught right after the first pericenter passage, which caused the current star-burst episode, and will most probably come close again in the future.

Mrk 436 is a second ULIRG at $z = 0.0504$ whose morphology is significantly affected by a recent interaction between two spirals. Bianchi et al. (2008) resolved in the central region of this system the presence of two X-ray compact sources at a projected distance of $\sim$ 3.8 kpc and with a projected velocity difference of $\sim 50\,\mathrm{km\,s^{-1}}$. These X-ray Chandra observations confirmed the presence of a luminous, obscured AGN in both nuclei.

The case of the LIRG **Arp 299** at $z = 0.0103$ is less certain. The system is composed of two interacting galaxies, NGC 3690 and IC 694, with two active nuclei at a projected distance of $\sim$ 4.6 kpc. Multi-wavelengths observations confirmed the presence of an obscured AGN in the nucleus of NGC 3690 (Della Ceca et al. 2002, Ballo et al. 2002, Tarchi et al. 2007, Garcia-Marin et al. 2006) while the case of IC 694 is ambiguous and could be interpreted as a less luminous and less absorbed AGN (Ballo et al 2004). **Mrk 739** (Koss et al. 2011) and **IRAS 20210+1121** (Piconcelli et al. 2010) are two other examples of a kpc scale double active nucleus discovered only with IR and hard X-ray observations in absence of clear optical AGN signatures because of dust obscuration and high levels of star formation.

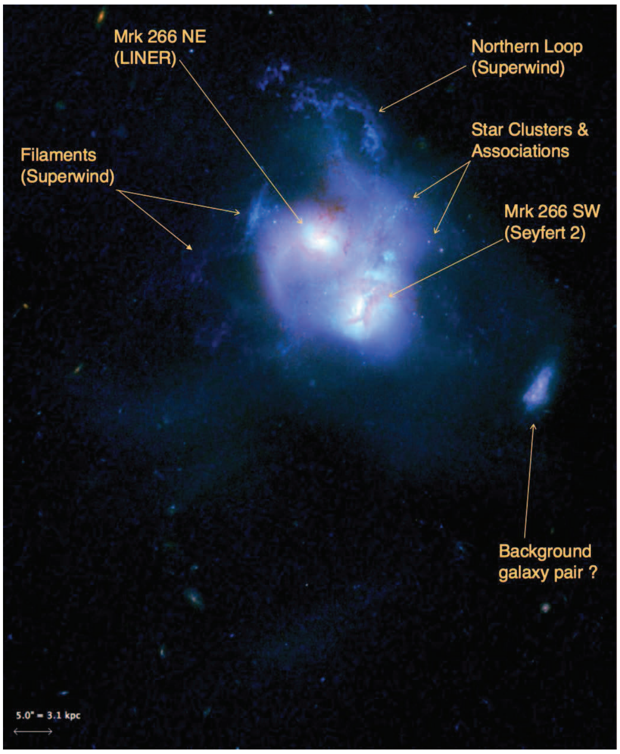

Figure 2.2: HST color composite image of the Mrk 266 system and its tidal features reported in the work by Mazzarella et al. (2012). North is up and east is left. The image field of view is 1.4′ × 1.6′, with a scale bar in the lower left corner. The color table has been chosen to maximize contrast for faint extended structures. Labels identify the major structures of this complex system.

More recently, Mazzarella et al. (2012) presented a multi-wavelength analysis of the merging system **Mrk 266** at $z \sim 0.03$ shown in Fig. 2.2. This is one of the most remarkable LIRGs in the local Universe characterized by several complex processes: vigorous star formation, two nuclei, labelled as North-Est (NE) and South-West (SW), at a projected separation of ~ 6 kpc, a powerful large-scale superwind, and substantial radio continuum and X-ray emission between the nuclei. The results of a detailed spectroscopic and photometric study indicate that both galactic nuclei host an accreting MBH of $\sim 2 \times 10^8$ M$_\odot$. The presence of an AGN in the SW nucleus is supported by the detection of a strong Fe Kα line consistent with the X-ray spectrum of an heavily obscured AGN. The SW nucleus is indeed much more obscured than the NE nucleus. The latter is classified as an AGN based on the presence of a hard X-ray point source, of a bi-conical outflow with aligned radio continuum and optical emission-line radiation, and on the results of mid-IR spectral diagnostics. The presence of an AGN-powered collimated outflow is suggested also by the observations of a circum-nuclear arc containing bright optical knots ~ 240 pc west to the NE nucleus and interpreted as clouds entrained in a shock front produced by the AGN jet. Mazzarella et al. (2012) propose a scenario where Mrk266 is observed in short-lived evolutionary stage leading to the final coalescence phase characteristic of ULIRGs. The two merging systems are indeed embedded in a low-surface brightness halo of tidal debris extending over ~ 100 kpc and have a small velocity difference ~ 135 $\mathrm{km\,s^{-1}}$ along the line of sight. Moreover the total cold molecular gas mass of $\approx 7 \times 10^9$ $\mathrm{M_\odot}$ is similar to local and high-redshift ULIRGs, and $\sim 40\%$ is located between the galaxies representing a reservoir available to form more stars and to fuel the AGN as the two nuclei coalesce.

At slightly larger spatial scales and a lower relative prominence of the dust IR emission, Guainazzi et al. (2005, G05 hereafter) and Green et al. (2010) report the discovery of two systems of interacting disk galaxies with a double active nucleus: **ESO509-IG066** at $z = 0.03$ and **SDSSJ1254** at $z = 0.44$, respectively. The former case shows two obscured AGN at a projected separation of $\simeq 10.5$ kpc. G05 notice that although the optical morphology is only mildly affected, the system is probably gravitationally bound, suggesting a system observed at the initial dynamical stages of a merger. Instead SDSSJ1254 consists of two luminous AGN separated by $\simeq 21$ kpc and hosted in a highly morphologically disturbed system with clear signs of an ongoing gas-rich merger. According to Green et al. (2010), the system is observed at the first pericenter passage that probably caused an enhancement in the accretion rate of one of the two active MBHs.

A prominent tidal tail indicative of a recent interaction and two compact nuclear sources are observed in the HST image of the galaxy **COSMOSJ1000** at $z = 0.36$, as reported by Comerford et al. (2009a) and shown in Fig. 2.3. These authors interpret the two bright sources as two obscured AGN with a projected distance of ~ 2.5 kpc and a line of sight velocity offset of $150\,\mathrm{km\,s^{-1}}$. Through subsequent spectroscopic observations, Civano et al. (2010) detected a velocity off-set of $\sim 1300\,\mathrm{km\,s^{-1}}$ between the broad and narrow components (see Sec. 2.2.2) of the Hβ line. Then

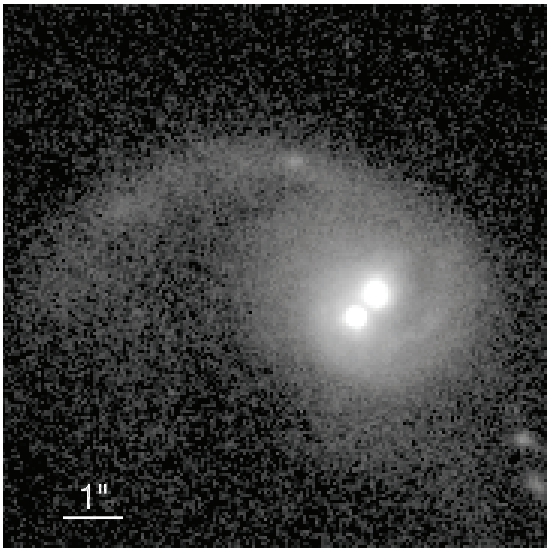

Figure 2.3: HST image of COSMOSJ1000 from the work of Comerford et al. (2009a). The prominent tidal tail is suggestive of a recent merger. Tho bright nuclei, interpreted alternatively as a double AGN system or as a recoiling AGN, are observed near the galaxy center at a projected separation of ~ 0.5", corresponding to ~ 2.5kpc at the source redshift $z \sim 0.36$.

two other possible explanations were proposed for this source: a recoiling AGN (see also Sec. 3.3.1) kicked out the galactic nucleus after that a MBHB reached coalescence $\sim 1 - 10$ Myr ago, and a double AGN system where one of the two accreting MBHs is recoiling due to the slingshot effect produced by a triple MBH system. The nature of this peculiar source is therefore still much debated and new spatially resolved, high-quality spectral analysis is needed to discriminate between the different models (see Blecha et al. 2012 and references therein).

Clues of the presence of a dual AGN system can be found in radio sources displaying one or two pairs of radio jets with peculiarly disturbed radio morphologies. The most famous case is that of **3C75** located at the center of the Abell 400 cluster at $z = 0.0244$. In this system two active nuclei are seen at a projected separation of $\simeq 7$ kpc and both sources emit a pair of radio jets as shown in Fig. 2.4. Optical, radio and X-ray observations favor the scenario where the bending of the radio jets is due to the inter galactic medium wind with a speed of $\sim 1200 \mathrm{km\,s}^{-1}$ relative to the two bound active nuclei orbiting

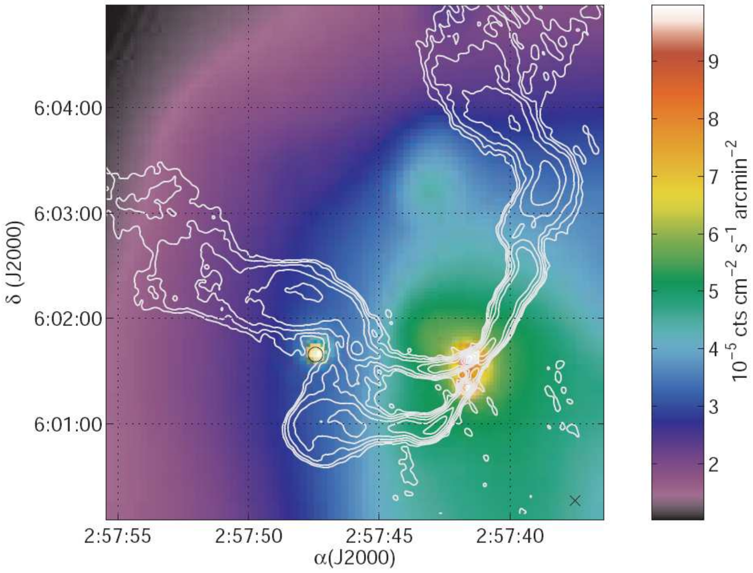

Figure 2.4: X-ray surface brightness map of the central region of the Abell 400 cluster in the 0.7-7 keV band with an overlay of VLA 4.5 GHz contours. The diffuse X-ray emission weighted center is labelled with an x. It can be noticed that the radio jet of one the two nuclei appears to be deflected and to travel around another element of the cluster whose center is marked with an o (Hudson et al. 2006).

around each other (e.g. Hudson et al. 2006 and references therein). Similar features have been discovered in the radio observations of two other sources: **PKS B0319-454** (Klamer et al. 2004) and **PKS 2149-158** (Guidetti et al. 2008).

3C 321 at $z = 0.0961$ is characterized by a compact radio source emitting a powerful radio jet that shows two radio lobes at ~ 250 kpc from the nucleus and a luminous knot at smaller scales in the proximity of a companion galaxy. This is located at ~ 6 kpc from the radio nucleus and is the host of a second active MBH. The results of multi-wavelength observations do not exclude that the interaction observed with the jet may have triggered the nuclear activity in the companion galaxy. However the hypothesis of a previous interaction at the origin of the accretion seen in both nuclei seems to be more plausible (see Evans et al. 2008 for a detailed discussion). Similarly Ivison et al. (2008) consider that a galactic interaction is responsible for the AGN activity of the more distant radio source **4C 60.07** ($z = 3.8$) as well as of its companion galaxy at 30 kpc away and of the intense level of star formation observed in the system. Kunert-Bajraszewska & Janiuk (2011) suggested that the disturbed morphology of the jet and of the host galaxy of the radio source **FIRST J164311.3+315618** could be attributed to the interaction occurred at the first pericenter passage with the companion AGN located 15 kpc away.

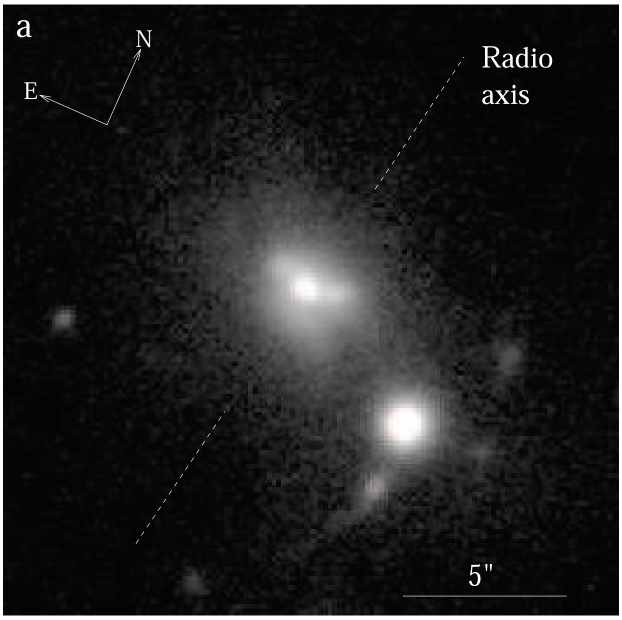

Figure 2.5: Gemini image of PKS0347+05 reported in the work by Tadhunter et al. (2012). The scale bar and the North and Est directions are shown in the lower right and upper left corner, respectively. The axis of the jets emitted by the radio galaxy coincident with the north est system is also shown.

Besides, Tadhunter et al. (2012; T12 hereafter) recently clarified the nature of the peculiar powerful radio source **PKS0347+05** at $z \sim 0.339$ discovering that it consists of a radio-loud/radio-quiet Double AGN system at a projected separation of ~ 25 kpc. The results of previous photometric observations revealed the presence of a diffuse galaxy at the position expected for the radio source host at odds with the spectroscopic detection of strong broad lines (see Sec. 2.2.2) and non-stellar continuum emission typical of compact radio-loud quasars. The new optical observations obtained by T12 showed that the spectrum of the radio host galaxy displays only weak narrow emission lines while the broad emission lines originate from a compact object observed at ~ 5" to the south west from the radio nucleus. The analysis of deep optical images, shown in Fig. 2.5, reveal a high degree of morphological disturbance with a warped dust lane crossing the nuclear regions of the radio galaxy host, tidal tails and a bridge connecting the radio galaxy to the western nucleus. Moreover the optical and IR spectra provide robust evidence for a strong and recent ($t \lesssim 100$ Myr) star formation activity. Therefore T12 favor a scenario where both AGN were triggered in a major galaxy merger, responsible also for the high level of star formation observed, but the merger-driven accretion rate into the nuclear regions of the radio source switched off within the last $\sim 10^6$ yr so that the information about the resulting decrease of the AGN activity has not yet reached the extended lobes and hotspots.

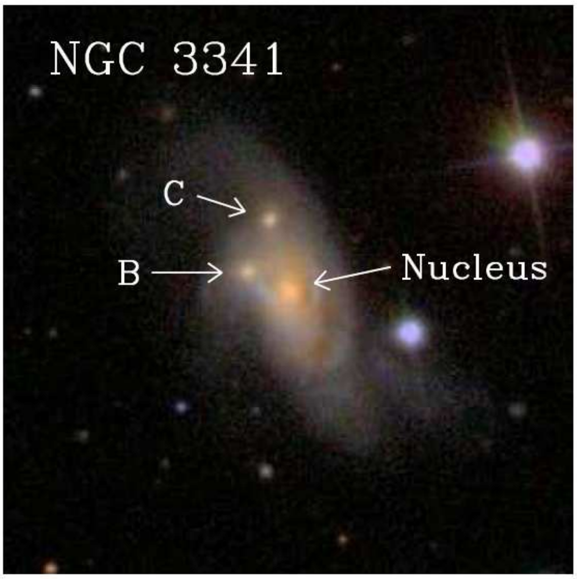

Figure 2.6: Color-composite image of NGC3341 from the Sloan Sky Digital Survey (Barth et al. 2008).

All the sources described so far are examples of major mergers, i.e. of interaction between two systems with a mass ratio $\gtrsim 0.3$. Although more difficult to observe, evidence of nuclear activity probably triggered in the course of a minor merger has been serendipitously found in **NGC 3341** (Barth et al. 2008) whose optical image is shown in Fig. 2.6. The system consists of a spiral galaxy interacting with two minor dwarfs galaxies indicated as B and C in the figure. These two companions are located at projected separations of ~ 5.1 kpc and ~ 8.4 kpc and have a line of sight velocity difference $< 200\,\mathrm{km\,s^{-1}}$ from the primary galaxy. The optical spectrum of one of the two dwarfs companions, namely of nucleus B, shows the presence of an obscured AGN. The nature of the other two nuclei is more uncertain and they are probably the hosts of both a low luminosity AGN and of HII regions. Future X-rays observations are necessary to verify the nature this peculiar source that would be the first case of a multiple AGN system in a triple minor merger.

More recently Fabbiano et al. (2011) reported the discovery of two obscured AGN in the central regions of the spiral galaxy **NGC 3393** at a projected separation of 150 pc. The discovery is interpreted in terms of a merger of unequal mass galaxies considering that: (i) the timescale for the two MBHs to reach the close observed separation would be longer relative to the case of a major merger, enhancing the chance of detecting such events; (ii) the remnant of a minor merger would be more consistent with the regular spiral morphology of NGC 3393 and its old circum-nuclear stellar population.

Finally, after the results reported by Comerford et al. (2009b) for a sample of elliptical galaxies, different groups started a systematic search of dual AGN candidates selected because of two systems of narrow lines (see Sec. 2.2.2) with velocity offsets of a few $100\,\mathrm{km\,s^{-1}}$ observed in the same optical spectrum. During a galaxy merger, the two MBHs hosted in the inspiralling nuclei can give rise to two separated set of narrow emission lines if they are both active at the same time, and if their separation is $\gtrsim 1$ kpc. In this case the two narrow line regions do not overlap and have a relative velocity of $\lesssim 300(M_{10}/d_1)^{1/2}\,\mathrm{km\,s^{-1}}$, where M_{10} and d are respectively the total mass and the separation of the two nuclei in units of $10^{10}\,\mathrm{M_\odot}$ and 1 kpc, assuming that their binding energy is ≤ 0. However further spatially resolved spectroscopy and high resolution photometric observations are necessary to confirm the dual AGN scenario against other possible physical interpretations such as the presence of a rotating gaseous structure or a biconical gas outflow in the narrow line region of a single active MBH (e.g. Heckman et al. 1981, Greene & Ho 2005). The most recent results of these searches indicate that $\lesssim 1\%$ of low-redshift AGN displays a double-peaked [OIII] narrow line and that $\lesssim 10\%$ of these sources may actually host two active MBHs (e.g. Fu et al. 2012, Liu et al. 2012 and references therein).

2.1.2 0402+379: the only resolved bound binary

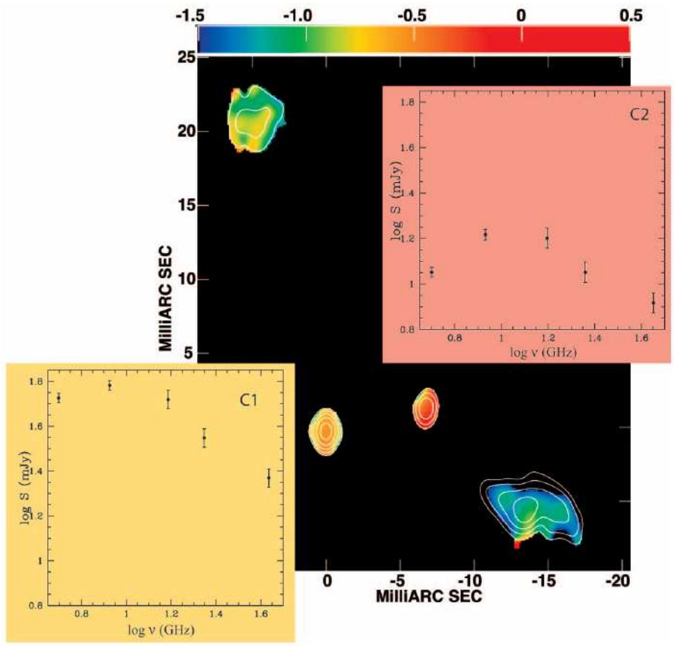

Figure 2.7: Spectral index distribution between 8 and 22 GHz from VLBA observations of the two resolved radio nuclei in 0402+379. The contours in the background are from VLBA observations at 22 GHz (Rodriguez et al. 2006).

0402+379 is a radio galaxy observed at $z = 0.055$ by Maness et al. (2004; M04 hereafter). M04 noticed the presence of two variable compact components (labelled C1 and C2) characterized by a flat spectrum and a projected separation of $\simeq 7.3$ pc. M04 identified two plausible explanations for the peculiarities of this source: the presence of a single accreting MBH in one of the two compact sources with the other one interpreted as an unusual component of the radio jets; a binary system of two accreting MBHs. In order to distinguish between these two scenarios, and in particular to measure the relative motion of the two compact sources, Rodriguez et al (2006; R06 hereafter) obtained high frequency and high resolution observations with the Very Long Baseline Array (VLBA). Figure 2.7 shows the results of these VLBA observations at 22 GHz together with the spectral index distribution of the two radio components C1 and C2. The analysis of R06 confirmed the compactness of both components and disfavored the interpretation of C2 or C1 as a luminous knot in the southern jet considering that: (i) the radio jets components move away from C1 in opposite directions with substantial velocities $\gtrsim 0.1c$ while C2 does not show a comparable significant motion; (ii) the characteristics found in C1 and C2 are typical of AGN; (iii) if C2 is the core responsible for the observed jets and C1 is a jet component it would be difficult to explain the absence of the corresponding counter-jet given the orientation of the source close to the plane of the sky; (iv) the absence of a jet associated with C1 in the 5 GHz VLBA observations is not unusual considering compact radio sources with comparable fluxes.

All these findings leave the remaining most likely explanation that both C1 and C2 are active MBHs in a compact binary system with C2 being the source of the radio jet. According to R06, this hypothesis is supported by the optical and X-ray observations of the host system showing an elliptical galaxy embedded in a halo of faint, disturbed emission extending to a possibly interacting companion. Further observations will be important to verify the nature of this extended emission and its connection with a recent merger and the nuclear activity. In the MBHB scenario, R06 estimates the binary total mass from the relation between the MBH mass and the luminosity of the host galaxy (Kormendy & Gebhardt 2001) obtaining a value of $\sim 7 \times 10^7 \mathrm{M}_\odot$, implying a coalescence timescale for GW emission exceeding the Hubble time.

2.2 Unresolved systems

2.2.1 Periodic light-curves: the case of OJ287

OJ287 is classified as a blazar at redshift $z \simeq 0.3$, i.e. a radio loud AGN seen close to face-on along the direction of the radio jet. This source has been monitored for more than a century (Valtonen et al. 2006 and references therein) and its light curve shows a complex periodic behavior with two main cyclic oscillations on timescales of ~ 12 and ~ 60 years. Other blazar sources show optical variability with indication for periodicities but these periodic signatures are generally less significant and persistent as in OJ287 (see e.g. Komossa et al. 2006). For instance, the MBHB scenario has been considered in two recent works by Godfrey et al. (2012) and Caproni et al. (2012) to interpret the periodic structure of the bright knots observed in the jet of PKS

0637-752 and BL Lacertae, respectively. However further observations are necessary to favor the binary hypothesis against other possible explanations such as accretion disk instabilities and jet precession motions in the presence of an isolated accreting MBH. Although there exist alternative models also for the case of OJ287 (Villforth et al. 2010), it is the strongest MBHB candidate selected up to date because of a periodic signature in its lightcurve.

The MBHB model proposed in Lehto & Valtonen for OJ287 (1996; LV96 hereafter) considers an eccentric binary system with $e \simeq 0.663$, an orbital period of 12 yr and an unequal binary mass ratio. The observed blazar corresponds to the primary MBH feeded by an accretion disk whose plane is assumed to be almost perpendicular with respect to the binary orbit. In this scenario the two luminosity peaks with the shorter periodicity are due to the impacts between the primary accretion disk and the secondary MBH at its pericenter passage. Instead the longer brightness cycle is explained considering that the precession of the orbit is $39\,^{\circ}$ per period so that the semi-major axis rotates through $180\,^{\circ}$ in almost 5 periods corresponding to ~ 60 yr.

The secondary MBH mass is assumed to be of the order of $10^8 \mathrm{M}_{\odot}$ and the primary mass can be consistently derived considering two different constraints: the precession of the binary orbit predicted by the theory of General Relativity and the requirement of a stable primary accretion disk after multiple impacts with the secondary MBH. The former criterion implies a primary mass of $\sim 1.8 \times 10^{10} \mathrm{M}_{\odot}$ while the latter leads to a lower limit of $10^{10}\,\mathrm{M}_{\odot}$. The values derived in this model for the primary mass are close to the upper limit of the observed AGN mass distribution. However it can be regarded as a reasonable result considering that OJ287 is among the most luminous observed blazars with a peak luminosity of $\sim 3 \times 10^{47} \mathrm{erg\,s^{-1}}$ (Worral 1982).

Recent results reported by Valtonen et al. (2008) correspond to the last observed luminosity burst. This was scheduled on September 2007 according to the orbital parameters determined with the 5 luminosity peaks observed between 1957 and 2005. The outburst occurred within a day of the time predicted by the MBHB model taking into account the emission of gravitational waves. In the absence of the gravitational wave emission, the outburst predicted by the MBHB model would have happened 20 days later.

2.2.2 Spectral signatures: double-peaked broad emission lines

The spectrum of an AGN is characterized by strong emission lines observed on top of the continuum emission. These emission lines are classified as broad (BELs) or narrow (NELs) if their profile width is larger or smaller than $\sim 1000\,\mathrm{km\,s^{-1}}$, respectively (e.g. Osterbrock & Ferland 2006). In the standard AGN model (e.g. Urry & Padovani 1995), BELs are emitted by gas gravitationally bound to the active MBH, forming the so called broad line region (BLR) on scales $\lesssim 1$ pc. Instead NELs originate from ionized gas located at much greater distances ($\sim 0.1 - 1\,\mathrm{kpc}$) and subject to the host galaxy potential.

Since the seminal paper by BBR, spectroscopy has been considered a viable tool to find direct evidence of the orbital motion of active MBHs bound in a Keplerian binary. In presence of a binary system, BELs are expected to peak at a different velocity from that of the NELs because of the orbital motion of the active MBH around its close companion. An advantage of this technique is that it is not limited by any requirement of high spatial resolution. On the contrary spectral features associated with MBHBs become more significant at pc/sub-pc scales where the expected velocity off-sets between the broad and narrow lines are $\gtrsim 1000\,\mathrm{km\,s^{-1}}$.

Gaskell (1983) was among the first to attribute the presence of two displaced broad line peaks in sources such as 3C 390.3 to the orbital motion of two MBHs, each with its associated BLR. A natural prediction of the MBHB model is that the broad line peaks should drift towards opposite directions according to the binary orbital period. Spectral monitoring over several years is therefore required to confirm the presence of a binary considering that the period of sub-pc MBHBs can be as long as a few 100 yr.

Long-term variability studies (Eracleous et al. 1997; Gezari et al. 2007; Lewis et al. 2010) of about two dozen AGN displaying two peaks in the broad line profiles did not find evidence of the behavior expected in the MBHB scenario. Currently the most favored model to explain the shape of the line profile as well as other peculiar features of this class of AGN, refereed to as double-peaked emitted (DPEs), considers an accretion disk in the BLR of a single AGN (see discussion of Eracleous & Halpern 2003 for details).

One of the most recent MBHB candidate selected because of two set of BELs at different redshifts is **SDSS J1536+0441** (Boroson & Lauer 2009). This source was also proposed as a peculiar case of DPE and its nature is still

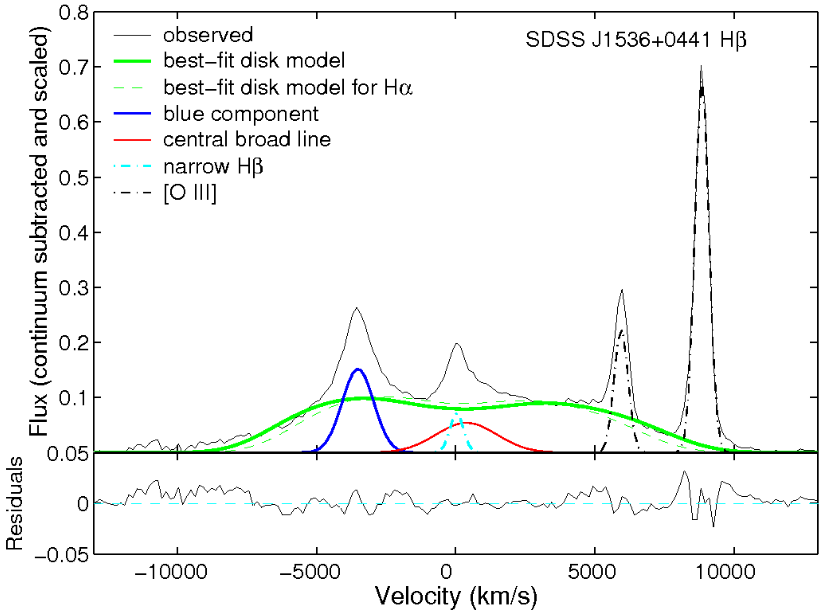

Figure 2.8: Hβ continuum subtracted emission line profile for the quasar SDSSJ1536. Tang & Grindlay (2009) consider different components to fit the observed black line profile according their proposed MBHB model. As listed in the panel, the green double-peaked lines refer to the disk model for the BLR around the primary MBH that is considered responsible also for the red central broad component. The blue-shifted peak is associated with the secondary MBH while the dash-dotted black and cyan lines refer to the narrow components of the Hβ and the [OIII] doublet, respectively.

under debate. In particular, the optical spectrum of this candidate shows a first set of broad and narrow lines at the same redshift and a second set of only broad lines blue-shifted if $\sim 3600\,\mathrm{km\,s^{-1}}$. Chornock et al. (2010) gave support to the case of a DPE against the binary interpretation because of an additional red shoulder detected in the broad line profiles with subsequent spectral observations.

Further multi-wavelength studies performed also by our group revealed the presence of a moderately rich cluster around SDSS J1536+0441 together with a companion galaxy at a distance of $\sim$ 5 kpc. However the nucleus of the companion source is not expected to significantly contribute to the observed BELs disfavoring the case of a chance superposition of two unrelated sources along the line of sight (Wrobel & Laor 2009, Decarli et al. 2009a, Lauer & Boroson 2009, Decarli et al. 2009b). Moreover Tang & Grindlay (2009) suggested that this AGN hosts a MBHB where the lighter active MBH contributes to the blue-shifted BEL peak while the more massive MBH is a DPE as shown in Fig. 2.8. A similar model was then discussed by Barrows et al. (2011) to explain the peculiar features of the blue peaks observed in the BELs of the DPE **SDSSJ0932+0318**.

Chapter 3

A new sample of spectroscopic MBHBs and the peculiar case of SDSSJ0927

In this Chapter we focus on spectroscopic MBHB candidates displaying a set of optical broad emission lines at a different redshift from that of the host galaxy rest frame. We start with the analysis of the peculiar observational features of the AGN SDSSJ092712.65+294344.0 (SDSSJ0927 hereafter). We discuss the model of a sub-pc MBHB orbiting in the central cavity of a circum-binary gaseous disk that have been proposed by our group to interpret the peculiar features of SDSSJ0927. Our analysis of this source have been presented in the work of Dotti, Montuori et al. (2009b), published at the same time with that of Bogdanovic et al. (2009) who make similar considerations. We then describe the subsequent search of AGN spectra resembling that of SDSSJ0927 carried out in the spectroscopic database of the Sloan Sky Digital Survey (SDSS; York et al. 2000) by different groups including ours. Finally we present possible physical scenarios alternative to the binary hypothesis to interpret this peculiar class of AGN.

3.1 The peculiar spectrum of SDSSJ0927

SDSSJ0927 is a luminous AGN observed in the course of SDSS (Adelman-McCarthy et al. 2007). The optical spectrum is reported in figure 3.1 after correcting for the galactic extinction corresponding to $E(B-V) = 0.021$

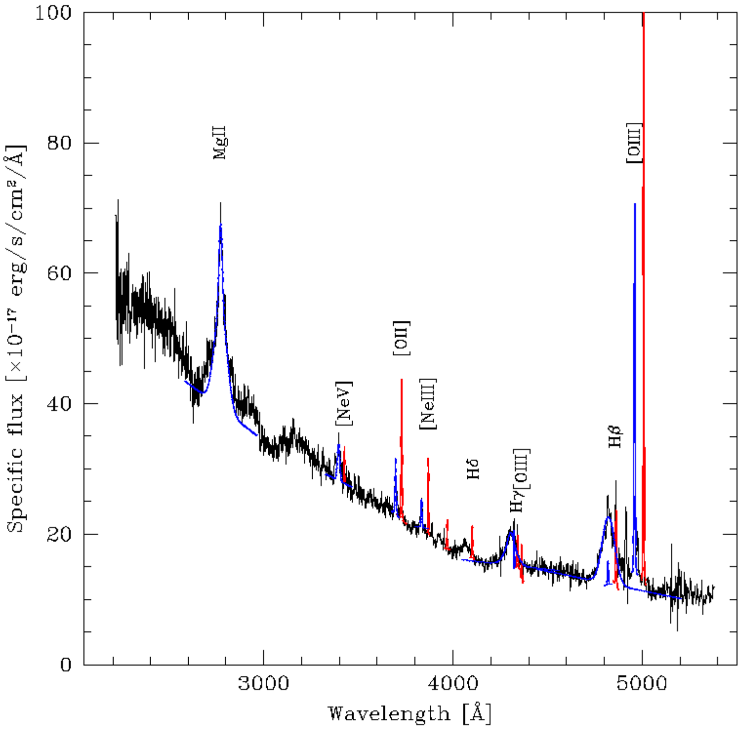

Figure 3.1: Optical SDSS spectrum of SDSSJ092712 reported at a redshift of $z = 0.713$. The red and blue curves represent Gaussian profiles fitted on the set of rf-NELs and on the blue-shifted broad and narrow emission lines, respectively (see the text for details).

mag as reported by the Nasa/IPAC Extragalactic Database[1] according to the map of Schlegel et al. (1998). The peculiarity of this spectrum consists in the presence of two distinct sets of emission lines whose profiles are highlighted in red and blue in the figure. The red curves correspond to a first set of lines at a redshift of $z = 0.713$ displaying similar, very narrow profiles. These narrow lines are typically observed in AGN spectra and will be referred to as rest-frame NELs (rf-NELs). The second set of blue lines is at redshift $z = 0.698$ corresponding to a blue-shift of $\simeq 2630$ km s^{-1} relative to the rf-NELs. This blue-shifted system consists of two sub-sets of emission lines characterized by different profile widths. The blue-BEL system (b-BELs) shows the typical

---

[1] http://www.ned.ipac.caltech.edu/

MgII and hydrogen Balmer lines with FWHM $\sim$ 4000 $\mathrm{km\,s^{-1}}$ while the blue-NELs (b-NELs) consist of the typical narrow forbidden lines although the high ionization lines such that of [NeV] and [NeIII] show unusually large FWHM up to $\sim$ 1250 $\mathrm{km\,s^{-1}}$.

Element	$\lambda(\text{Å})^b$	FWHM ($\mathrm{km\,s^{-1}}$)	FWHM^c ($\mathrm{km\,s^{-1}}$)	Flux ($10^{-17}\mathrm{erg\,s^{-1}\,cm^{-2}}$)
[OIII]	5007.58	209	146	515
	4363.76	245	195	7
Hβ	4861.52	283	241	57
Hγ	4341.01	325	288	26
Hδ	4101.91	227	170	23
[NeIII]	3969	294	253	18
	3869.28	209	146	34
[OII]	3727.91	441	415	129
[NeV]	3425.79	265	219	17

^{b} reported at the redshift of the rf-NELs $z = 0.713$
^{c} corrected for the instrumental resolution

Table 3.1: Properties of the rf-NELs in the optical spectrum of SDSSJ0927.

Table 3.1 gives the results obtained from the fits of the rf-NELs while table 3.2 refers to the blue-shifted system. All the emission lines are fitted on the spectrum reported at the redshift of the rf-NELs using Gaussian profiles.[2] To obtain the corrected FWHM values reported in the tables we subtract the instrument spectral resolution for the resolved lines[3]. The spectrograph resolution is of the order of the wavelength separation between the two lines of the [OII] λ3727 doublet and therefore it cannot be resolved.

		b-NELs		
Element	$\lambda(\text{Å})^b$	FWHM (km s^{-1})	FWHM^c (km s^{-1})	Flux (10^{-17}erg s^{-1} cm^{-2})
[OIII]	4960.12	260	212	325
	4323.10	138		11
Hβ	4818.92	308	269	19
[NeIII]	3834.04	443	417	33
[OII]	3696.32	413	386	58
[NeV]	3395.17	1319	1311	87
		b-BELs		
Hβ	4821.76	4882	4880	850
Hγ	4305.68	3713	3711	316
MgII	2771.71	4167	4164	1550

^{b} reported at the redshift of the rf-NELs $z = 0.713$
^{c} corrected for the instrumental resolution

Table 3.2: Properties of the two sets of broad and narrow blue-shifted lines in the optical spectrum of SDSSJ0927.

3.2 Binary model

In our model, SDSSJ0927 hosts a close MBHB interacting with a co-planar circum-binary thin disk. We focus on the best studied case of a prograde disk, i.e. co-rotating with the MBHB, as expected for a gas-rich major merger where there is enough cold gas in the surrounding of the MBHB to sustain a significant accretion rate onto the MBHs along the orbital decay (see Ch. 1). In this scenario, we assume that the observed AGN is the secondary, lighter MBH (M_2) of a binary orbiting in the central lower density region of the circum-binary disk. As discussed in Ch. 1, if the binary mass ratio is $q = M_2/M_1 \sim 1$, where M_1 is the primary MBH, the secondary can strongly perturb the surrounding disk structure, creating over few orbital

---

[2] The line flux computed for the blue-shifted system should be corrected by a factor of $1+z$, where $z = v_{\rm shift}/c$. However the correction would be of the order of 1% and can be neglected in our analysis.

[3] The resolution of the SDSS spectrograph is $\frac{\lambda}{\Delta\lambda} \sim 2000 \Rightarrow \mathrm{FWHM}_{\rm spectrograph} \approx 150$ km s^{-1}. To correct the FWHM we consider: $\mathrm{FWHM}_{\rm measured} = \sqrt{\mathrm{FWHM}^2_{\rm spectrograph} + \mathrm{FWHM}^2_{\rm line}}$

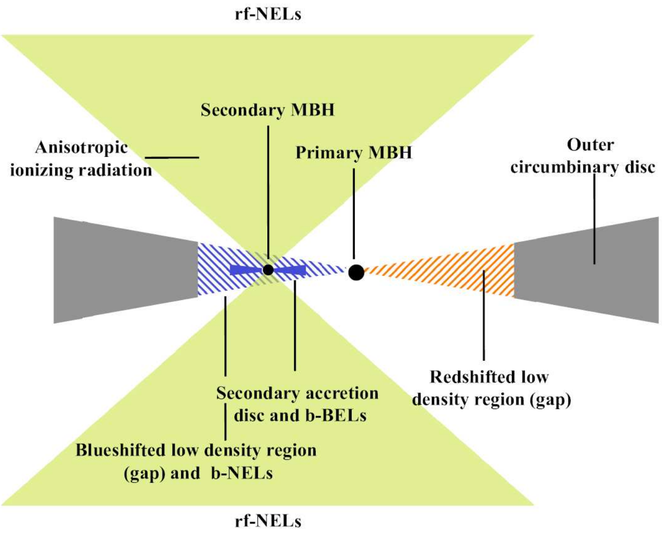

Figure 3.2: Sketch of the MBHB circum-binary disk structure in the nucleus of SDSSJ0927.

periods an annular low density region, commonly referred as gap, hindering long lasting accretion events onto the primary MBH. M_2, remaining in closer gravitational contact with the inner rim of the outer disk, has a low velocity difference with the higher density reservoir of gas, thus sweeping up an accretion stream that inflows from the edge of the gap. This continuous refueling supplies an accretion disc around M_2, and allows for luminous accretion events during its orbital decay (e.g. Cuadra et al. 2009; Rödig et al. 2012). As for large q and separations $\lesssim 0.1-1$ pc migration occurs on timescales $\gtrsim$ than the viscous time in the outer disk (see Ch. 1), this binary can be long-lived and we work under this hypothesis.

A sketch of the model is shown in Fig. 3.2. We will consider M_2 the only accreting MBH of the binary. In this model, the rf-NELs are emitted from the standard large-scale narrow line region extending far out in the galaxy up to ~ 1 kpc while the b-BELs are produced in the broad line region gravitationally bound to M_2, and can be blue-shifted or red-shifted depending on the orbital phase of the secondary. The b-NELs come from a region of the gap near M_2, where forbidden lines are emitted because of the low density of the gas. Since M_2 and the gas orbiting in the gap at comparable radii are subject to the same gravitational potential of M_1, both move with approximately the same Keplerian velocity. Accordingly, the same blue-shift for the b-BELs and b-NELs can be explained if M_2 emits an anisotropic ionizing radiation normal to the plane of the disk so that the ionizing photons interact preferentially with the gas in the gap near M_2. This is naturally achieved if for example the accretion flow around M_2 is a standard Shakura-Sunyaev accretion disk. Indeed, cosine-like behavior of the thermal ionizing flux, coupled to the small solid angle subtended by the circum-binary disk, assures that the ionization parameter of gas in the gap region not in the immediate vicinity of M_2 is relatively low.

In the next two Sections we will compute the orbital parameters and the properties of the gas in the gap region requested to reproduce the observed spectral features of SDSSJ0927.

As said before, a similar interpretation for SDSSJ0927 was proposed independently by the group of Bogdanovic et al. (2009; B09 hereafter). The slight difference between our work and that of B09 consists in the interpretation of the b-NELs. According to B09, the b-NELs are emitted by the gaseous streams flowing onto M_2 from the inner edge of the circum-binary disk. The streams properties are expected to be intermediate between those of the BLR around M_2 and of the NLR around the binary, giving rise to both permitted and forbidden lines from the higher and lower density parts of the flow, respectively.

3.2.1 Orbital Parameters

In this Section we use some of the observed properties of SDSSJ0927 (the blue-shift and the FWHM of the b-BELs, and the continuum luminosity at 5100 Å) to constrain the dynamical properties of the hypothetical MBHB. The compatibility of the model with the other observed spectral features (in particular the blue-shift and the flux of the b- NELs) is discussed in the next section.

According to what discussed in Sec. 3.2 and considering the large blue-shift of the observed b-NELs and b-BELs, corresponding to a high velocity of the accreting MBH, we assume that the active MBH is M_2, the lightest hole. Its mass is computed from the width of the broad Hβ line and the continuum luminosity measured at 5100 Å assuming the BLR radius-luminosity relation of Kaspi et al. (2005). We thus obtain a BLR radius of the order of $R_{\rm BLR} \simeq 0.1$ pc and a MBH mass of $M_2 \simeq 6 \times 10^8$ M$_\odot$. We will further assume that the binary is moving on a (quasi) circular orbit (see below for a discussion on this point).

The first constraint to be verified is that the observed broad line region responsible for the b-BELs is bound to M_2 , and is not tidally stripped by M_1. This condition can be re-written as $R_{\rm BLR} < R_{\rm L}$, where $R_{\rm L}$ is the Roche lobe radius of M_2 . For a circular binary, $R_{\rm L}$ represents the radial size of the equipotential surface centered on the secondary MBH and connected with that around the primary MBH through the inner Lagrangian point. We estimate $R_{\rm L}$ using the approximation in Eggleton (1983) and impose:

$$\frac{R_{\rm L}}{a} = \frac{0.49q^{2/3}}{0.6q^{2/3} + ln(1 + q^{1/3})} \tag{3.1}$$

where a is the semi-major axis of the MBHB. The observed velocity, $v_{\rm obs}$, of M_2 depends on M_1 , a, the binary orbital phase and the orientation of the plane of the binary in the sky:

$$v_{\rm obs} = v_2 \sin i \cos\phi = \sqrt{\frac{GM_2}{aq(1 + q)}} \sin i \cos\phi \tag{3.2}$$

where v_2 is the orbital velocity of M_2 relative to the center of mass, $i \in [0°, 90°]$ is the angle between the line of sight and the direction normal to the orbital plane, and $\phi \in [0°, 360°]$ is the phase of the orbit. From eqs. 3.1 and 3.2, and assuming $\cos\phi = 1$ in order to minimize M_1 , we obtain

$$\frac{GM_2}{v_{\rm obs}^2 R_{\rm BLR}} \sin^2 i > q^{1/3}(1 + q)\frac{0.6q^{2/3} + \ln(1 + q^{1/3})}{0.49}. \tag{3.3}$$

The fraction on the left hand side of eq. 3.3 is constrained by the observations while the right hand side is a monotonically increasing function of q. Given the inclination i, eq. 3.3 defines a maximum q, and a corresponding minimum M_1 . We focus on the minimum mass of M_1 , obtained for the largest value of $\sin i$, that is fitting all the observational constraints. Assuming that the unification model for AGN (Urry & Padovani 1995) remains valid for this peculiar object, the observation of the b-BELs limits the maximum value of the inclination of the orbital plane to $i_{\rm max} \approx 40°$, which implies $q \approx 0.35$, $a \approx 0.34$ pc, and $M_1 \approx 1.7 \times 10^9 {\rm M}_\odot$, value consistent with the observed high mass end of the MBH mass function. These values correspond to an orbital period of 370 yr. The time-scale for two MBHs in SDSSJ0927 to reach final coalescence due to gravitational wave emission is 3×10^9 yr, shorter than the

Hubble time. If the binary model will be confirmed, it would be the proof of the existence of a dynamical process able to overcome the so called last parsec problem (see Ch. 1) and drive MBHBs to the final coalescence.

Using the FWHM of [OIII] as a tracer of the stellar velocity dispersion, σ, and assuming the $M_{\rm BH} - \sigma$ relation given by Ferrarese & Ford (2005), we obtain for M_1 a mass ~ 3 orders of magnitude smaller than our estimate. This would be in contrast with the high luminosity of SDSSJ0927, which would imply extremely super Eddington luminosity ($\sim 10^3$ Eddington). On the other hand, in the MBHB scenario, the dynamics of gas may be not representative of the galactic potential, due to the recent galaxy merger.

As discussed in Chapter 1, the interaction between the binary and the surrounding disk affects the evolution of both the orbital separation and the eccentricity. In particular, as the semi-major axis decreases, the binary eccentricity is expected to grow after the gap opening phase up to fairly high values $e \sim 0.6 - 0.8$ (e.g. Rödig et al. 2011). In the specific case of SDSSJ0927 an eccentricity of the order $e \lesssim 0.5$ is still compatible with our binary model. Larger values are instead unlikely: if the binary has a large eccentricity and M_2 is near apocenter, an extremely massive M_1 is needed to justify such a large orbital velocity. On the other hand, Shields et al. (2009a) obtained a new optical spectrum of this source with the Hobby-Eberly Telescope that confirmed the basic features observed in the SDSS spectrum and set an upper limit of 10 $\rm km\,s^{-1}\,yr^{-1}$ on the change of the Doppler shift of the b-BEL system. In the binary scenario, this prevents M_2 to be caught too close to the pericenter. We note that assuming a circular orbit and the set of MBHB parameters discussed above, the b-BEL system moves only of 4.2 $\rm km\,s^{-1}$ over three years, corresponding to an average shift of 1.4 $\rm km\,s^{-1}\,yr^{-1}$.

3.2.2 Emission from the gap region

Our model suggests that the b-NELs are produced from the low-density gas in the gap region near M_2. This assumption explains the blue-shift of these lines, as we discussed in Sec. 3.2. For consistency, we need to constrain the properties of the gas in the gap, and check if its physical status is consistent with the production of the b-NELs and with the energy flux observed at these frequencies.

We assume that the gas in the gap is mostly ionized, so that we can derive the gas properties from the luminosity of the Balmer lines. Under the hypothesis of isotropic emission the total luminosity of the Hβ line is

$$L_{\mathrm{H}\beta} = 4\pi D_L^2 F_{\mathrm{H}\beta} = h\nu_{\mathrm{H}\beta} n_p n_e \alpha_{\mathrm{H}\beta} V_{\mathrm{gap}}, \tag{3.4}$$

where $D_L = 4127$ Mpc is the luminosity distance of SDSSJ0927, $F_{\mathrm{H}\beta} = 1.9 \times 10^{-16}$ erg s^{-1} cm^{-2} is the flux of the b-NEL component of the Hβ line (that we obtained directly by fitting the rest-frame, de-reddened SDSS spectrum as explained in Sec. 3.1), h is the Planck constant, $\nu_{\mathrm{H}\beta}$ is the frequency of the Hβ photons, n_p and n_e are the densities of protons and electrons respectively, and $\alpha_{\mathrm{H}\beta}$ is the recombination coefficient. In order to estimate n_e we need to constrain the volume of the emitting region, V_{gap}, that we assume to be half of the total volume of the gap in which M_2 resides (see discussion in Sec. 3.2)

$$V_{\mathrm{gap}} = 2\pi \int_0^{R_{\mathrm{gap}}} r^2 \frac{H(r)}{r} dr, \tag{3.5}$$

where $H(r)$ is the thickness of the low density gaseous structure at a radius r and R_{gap} is the gap radius. For a binary mass ratio $q \sim 0.3$, as obtained in the previous Section, the position of the inner edge of the outer circumbinary disk is known to be $R_{\mathrm{gap}} \approx 2a$ (e.g. Artymovicz & Lubow 1994). We use the standard assumption that $H(r)/r = c_{\mathrm{s}}/v_{\mathrm{Kepl}}$, where c_{s} is the local sound speed of the plasma and v_{Kepl} is the Keplerian velocity of the gas due to the potential well of M_1 . In this first estimate we assume $T \approx 10^4$ K, that corresponds to $H(r)/r \approx 5 \times 10^{-3}$. Replacing this ratio in eq. 3.5 and using eq. 3.4 we obtain $n_e \approx 8 \times 10^6$ cm^{-3}.

A different estimate for n_e can be obtained assuming that the vertical support of the low density gas in the gap is due to a supersonic turbulent motion of the plasma of the order of 1/2 the average FWHM of the b-NELs. In this second estimate we assume $v_{\mathrm{turb}} \approx 200$ km s^{-1}, corresponding to $n_e \approx 2 \times 10^6$ cm^{-3}. We emphasize that these estimates must be considered as a lower limit, because the gas can be clumpy (so that only a fraction of the irradiated gas will contribute consistently to the Hβ emission), and because the anisotropic radiation produced in the accretion disc of M_2 can irradiate less than 1/2 of the gap.

An additional, independent constraint on n_e can be obtained from the flux ratios of different Oxygen lines, in particular the [OII]$_{3727}$ doublet and the [OIII]$_{4363,4959,5007}$ lines (see e.g. Osterbrock & Ferland 2006 and references therein). The ratio between the two components of the [OII] doublet cannot be employed here, since the lines are practically unresolved.

We restrict our analysis to the [OIII] lines and in particular to the ratio $[\mathrm{OIII}]_{5007+4959}/[\mathrm{OIII}]_{4363}$. We notice that the b-$[\mathrm{OIII}]_{5007}$ and the rf-$[\mathrm{OIII}]_{4959}$ are blended while the b-$[\mathrm{OIII}]_{4959}$ is not reported in table 3.2 because of the very low S/N value of the spectrum at the corresponding wavelength, probably due to a bad sky subtraction. Therefore we derive the b-$[\mathrm{OIII}]_{5007+4959}$ assuming a factor of 3 between the fluxes of $[\mathrm{OIII}]_{5007}$ and $[\mathrm{OIII}]_{4959}$ in both systems (Osterbrock & Ferland 2006). We then compare the observed line flux ratio to the expectations for a gas in photo-ionization equilibrium, which yields $T_e = 10^4 - 2 \times 10^4$ K.

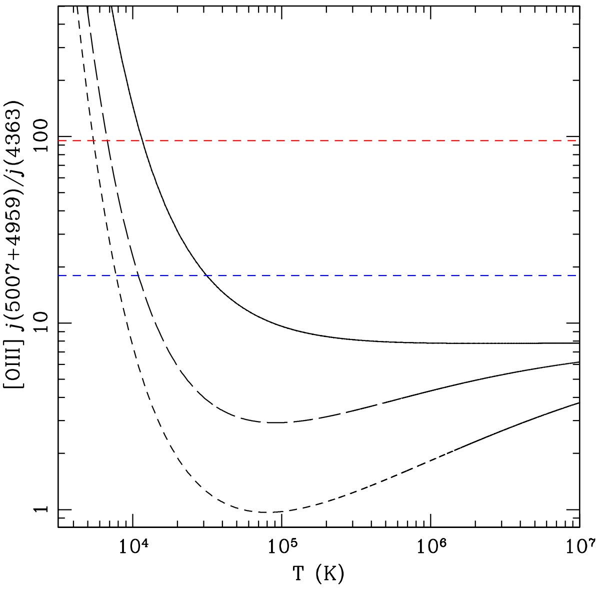

Figure 3.3: [OIII] line ratios as function of the temperature for different values of the electron number density n_e. The solid curve is for $n_e = 10^5\,\mathrm{cm}^{-3}$ at which value the low-density limit given in eq. 3.6 coincides with the non approximated expression given in eq. 3.7. The long and short-dashed curves correspond to eq. 3.7 for $n_e = 2\times10^6\,\mathrm{cm}^{-3}$ and $n_e = 8\times10^6\,\mathrm{cm}^{-3}$, respectively. These two density values represent a possible estimate for the gas in the gap region as explained in the text. The blue and red horizontal dashed lines corresponds to the values measured from the optical spectrum of SDSSJ0927 for the b-NELs and the rf-NELs, respectively.

As shown in Fig. 3.3, in order to be consistent with the expected temperature range we have to discard the low-density limit approximation typically assumed for the narrow line region given by:

$$\frac{j_{5007} + j_{4959}}{j_{4363}} = \frac{7.9 \exp\left(3.29 \times 10^4/T\right)}{1 + 4.5 \times 10^{-4} n_e/T^{1/2}} \tag{3.6}$$

where j_λ is the emission coefficient of a line at wavelength λ in units of $\mathrm{erg\,s^{-1}\,cm^{-3}\,sr^{-1}}$. Therefore we follow Seaton (1954) to compute the detailed equilibrium balance between the different levels of the [OIII], considering the contribution of collisional excitations and de-excitations, and we obtain the following expression:

$$\frac{j_{5007} + j_{4959}}{j_{4363}} = \frac{7.9(1 + 4 \times 10^{-6} n_e/T^{1/2}) \exp\left(3.29 \times 10^4/T\right)}{1 + 4.5 \times 10^{-4} n_e/T^{1/2}}. \tag{3.7}$$

Eqs. 3.6 and 3.7 can be computed as the ratios between the line emission fluxes in units of $\mathrm{erg\,s^{-1}\,cm^{-2}}$ as measured from the spectrum. The physical quantities needed to derive the line fluxes from j_λ are indeed the same for the three lines and cancel out in the ratio. The expression given in eq. 3.7 is function of both n_e and T_e and in particular for $T_e \sim 10^4$ K we obtain $n_e \sim 2.5 \times 10^6$ cm^{-3}. This density is fully consistent with the predictions from the Hβ luminosity. Increasing T_e, n_e decreases. At the maximum temperature allowed by the photo-ionization equilibrium, 2×10^4 K, the b-system has $n_e \sim 4 \times 10^5$ cm^{-3}. As mentioned before, typically [OIII] lines are produced in regions with much lower density ($n_e \simeq 10^3$ cm^{-3}). SDSSJ0927 is indeed confirmed to be a peculiar system.

We check our results by calculating if the production of a forbidden line such as the [OIII] in such high density regions is self-consistent. We compute the density of [OIII] ions $n_{\mathrm{[OIII]}}$ from the observed luminosity of [OIII] lines assuming the volume of the emitting region considered for the Hβ line with the temperature and electron density derived above from the observed flux ratio. We find $n_{\mathrm{[OIII]}} \simeq$ 2–4 orders of magnitude lower than n_e. This ratio is fully consistent with standard metallicities in quasars hosts.

The estimates of n_e obtained from the [OIII] and Hβ lines are much smaller than the density expected for a standard α-disk around M_1 at $r \sim a$, indicating the presence of a gap, confirming our expectations. However all the previous considerations can explain the presence of both Hβ and forbidden lines, but the [OII] doublet. [OII] emission is not consistent with such high densities, because the [OII] critical density for collisional de-excitation is $n_e \lesssim 10^4$ cm^{-3}. The detection of [OII] lines suggests that the gap is filled with an inhomogeneous, cloudy medium. The source of this inhomogeneity may be the competition between the gas inflow from the circum-binary disk and the periodic perturbation exerted by the MBHB (see, e.g. Cuadra et al. 2009; Bogdanovic et al. 2008; Rödig et al. 2012). In an inhomogeneously filled gap, Hβ lines are emitted in the highest density regions ($n_e \gtrsim 2 \times 10^6$ cm^{-3}), while [OIII] and [OII] lines are produced by intermediate (3×10^5 cm^{-3} $\lesssim n_e \lesssim 3.5 \times 10^6$ cm^{-3}) and low ($n_e \lesssim 10^4$ cm^{-3}) density regions, respectively.

3.3 Alternative scenarios

The presence of two set of broad and narrow emission lines at different redshifts in the same spectrum is not a distinguishing feature of a close MBHB. SDSSJ0927 was indeed initially selected by Komossa et al. (2008; K08 hereafter) as a first candidate *recoiling MBH* ejected from the host galaxy nucleus in the aftermath of a binary coalescence. On the other hand Heckman et al. (2009; H09 hereafter) and Shields et al. (2009a; S09 hereafter) proposed the scenario of a *chance superposition* along the line of sight of two distinct galaxies interacting near the center of a rich cluster. As mentioned in Sec. 2.2.2 and further discussed in Sec. 3.4, the most direct option to confirm the binary hypothesis would be to observe the expected periodic oscillation of the BELs around the host galaxy rest-frame because of the binary orbital motion. However below we will present further arguments disfavoring the other possible physical interpretations for the specific case of SDSSJ0927 apart from the eventual confirmation of a periodic BEL drift that will require follow up monitoring observations on timescales $\gtrsim$ 10 yr.

3.3.1 Recoiling MBH

Recent numerical relativity simulations have shown that for certain configurations of the MBH spins and of the orbital angular momentum, the remnant of a binary coalescence can attain kicks with quite large velocities up to ~ 5000 km s^{-1} because of the anisotropic emission of gravitational waves just before the merger (e.g. Lousto & Zlochower 2011 and references therein). In the recoiling scenario proposed by K08 for SDSSJ0927, the remnant MBH has been ejected at a projected speed of ~ 2630 km s^{-1} from the host galaxy nucleus together with its bound accretion disk and broad line region gas responsible

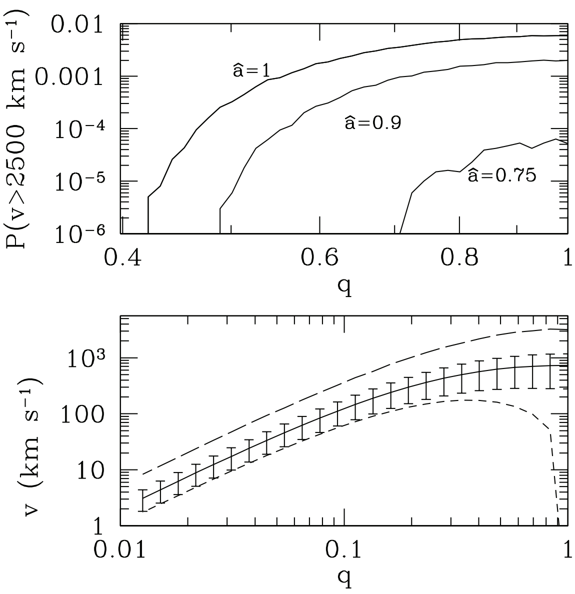

Figure 3.4: *Top*: probability for large recoil velocities ($v > 2500\ \mathrm{km\,s^{-1}}$) due to the coalescence of a MBHB expressed as a function of the binary mass ratio q and estimated as explained in the text. The lines are for three representative spin values for the two binary MBHs as indicated in the labels. Both holes are assumed to have the same spin, assuming isotropic orbital parameters. No recoil with $v > 2500\,\mathrm{km\,s^{-1}}$ is possible for MBH spin parameters $\hat{a} < 0.65$. *Bottom:* recoil velocity due to the coalescence of a MBHB obtained from the numerical relativity results of Lousto & Zlochower (2009). The recoil velocity is shown as a function of the binary mass ratio q for maximally Kerr holes with $\hat{a} = 1$. Long-dashed curve: maximum recoil. Short-dashed curve: minimum recoil. Solid curve: mean recoil, with 1-σ scatter. In all cases the recoil velocity is averaged over 10^6 orbital configurations for each q.

for the b-BELs. The rf-NELs represent the emission from the illuminated gas of the bulk of the NLR left behind while the b-NELs could arise in a trail of partially bound gas and swept-up ISM and/or from outflowing gas in the outer regions of the expanding accretion disk bound to the recoiling MBH. However we will show below that for this peculiar source the binary hypothesis is considerably more probable than the ejection hypothesis and that the origin of the b-NELs remains problematic in the recoiling scenario of K08.

The FWHM of the b-NELs is larger than the FWHM of the rf-NELs and of typical FWHMs of NELs observed in AGN. By contrast, the FWHM of b-NELs is not large enough to assure that the emitting gas is bound to the recoiling MBH, although this should be the case as the b-NELs have the same Doppler shift as the b-BELs. K08 suggest that the b-NELs are emitted by gas shocked in the interaction of the MBH with the ISM. In this case however, there is no reason why the speed of the shocked gas should equal that of the MBH (Devecchi et al. 2009). Alternatively, K08 consider that b-NELs are emitted in the outer part of the accretion disk with substantial radial spreading and/or in an unspecified kind of outflow. This last possibility was discussed in details by B09. They find that mass outflows strongly reduce the density of the inner regions of the accretion disk implying a low rate of gas accretion onto the MBH. In this case the luminosity would be much weaker than observed, unless the kicked MBH is more massive than $5 \times 10^9\,\mathrm{M}_\odot$.

Moreover we can estimate the probability of detection of an ejection with $v > 2500\,\mathrm{km\,s^{-1}}$ (we conservatively adopt this lower limit to the recoil velocity, which provides an upper limit to the detection probability) by convolving the probability of large recoils (shown in Fig. 3.4), based on the recent numerical relativity results of Lousto & Zlochower (2009), with the MBHB merger rates by Volonteri, Haardt & Madau (2003). We select coalescences in the redshift range $0.5 < z < 1$ (compatible with the redshift of SDSSJ0927), further imposing a total binary mass $M > 5 \times 10^8\,\mathrm{M}_\odot$ (i.e. the mass of the hypothetical recoiling MBH as obtained in Sec. 3.2.1). Marginalising over the MBH masses and q, the highest rate of successful recoils, $v > 2500\,\mathrm{km\,s^{-1}}$, is found by imposing maximal values for the spin parameters for both holes; the spins initially lie in the orbital plane pointing in opposite directions. The rate is 5×10^{-6} yr^{-1}. The expected ejection rate becomes less than 10^{-6}yr^{-1} assuming both MBHs with maximum spins but with isotropically distributed directions and decreases drastically with decreasing spin magnitude.

Then we compare the result for the recoiling scenario with the likelihood of the detection of a MBHB with the properties inferred by our model. We use the same theoretical merger-tree for cosmological MBHBs used before, imposing again limits on the redshift range ($0.5 < z < 1$), and computing the probability that an observer at $z = 0$ detects binaries with $M_1 > 1.5 \times 10^9$ $\mathrm{M}_\odot$ and $M_2 > 5 \times 10^8$ $\mathrm{M}_\odot$ across the entire sky. The observable merger rate corresponds to $\sim 10^{-4}$ binaries per year, a value 20 times larger than the expected rate of ejections obtained using the most favorable conditions for high kick velocity, as discussed before.

3.3.2 Chance superposition

The third model discussed by S09 and H09 to explain the peculiar features of SDSSJ0927 considers the possibility of a superposition of two galaxies, assuming the presence of a rich galaxy cluster. In particular, S09 favor the idea of a chance superposition of two distinct accreting MBHs, one unobscured AGN responsible for the blue-shifted broad and narrow emission lines and a second obscured AGN emitting the rf-NELs, while H09 propose the presence of just one active, unobscured MBH at the redshift of the blue-shifted system that is photoionizing the gas of a smaller galaxy falling toward it, giving rise to the rf-NELs. This model is the simplest explanation for the three sets of lines, and is immediately testable since it requires the presence of a rich galaxy cluster for two main reasons: (i) the observed high velocity difference between the two hypothesized galaxies would be too large for a simple ongoing merger in the absence of a deep potential well such that of a massive cluster; (ii) considering that the SDSS host galaxy image appears point like and the fiber spectrograph have a diameter of ~ 3 arcsec, the probability of a chance superposition of two AGN within 1 arcsec is not negligible only in presence of a cluster.

In order to confirm the presence of a galaxy overdensity around SDSSJ0927, Decarli et al. (2009c; D09 hereafter) obtained a deep NIR image of the field of this source and considered additional UV information to better assess the nature and redshift of field sources. Using four clusters at different redshifts for comparison, D09 find that the sources observed in the NIR image are several times fewer than expected if a cluster similar to those considered surrounded SDSSJ0927. The redshift differences of the two systems of SDSSJ0927 is at least two times larger than the velocity dispersions in the clusters considered for the comparison. If the alleged cluster surrounding SDSS0927 would be richer (so that its velocity dispersion would be higher), the expected galaxy counts will be even higher. Therefore the conclusion of D09 is that the cluster interpretation of SDSSJ0927 is strongly disfavored.

3.4 Systematic search

SDSSJ0927 was found by K08 searching for AGN with high [OIII] velocity shifts. After this discovery, two other sources displaying broad emission lines displaced by several 1000 $\mathrm{km\,s^{-1}}$ with respect to the NELs were noticed by

Shields, Bonning & Salviander (2009b) and Decarli et al. (2010) in the course of a search for double AGN systems and of a study of radio luminous AGN, respectively. As described in Sec. 2.2.2, two other MBHB candidates with double-peaked BELs were selected almost at the same period. These findings were possible because of the wealth of spectroscopic data made publicly available in the recent years by the SDSS. However these peculiar spectroscopic MBHB candidates remain elusive objects whose expected number and interpretation are still affected by theoretical uncertainties due, on the one hand, to the assumed binary merger rate, lifetime and observability timescale, on the other hand to the degeneracy between the binary hypothesis and the other possible physical scenarios discussed in Sec. 3.3 and 2.2.2.

All the above considerations urged two different groups to undertake a systematic search in the SDSS database in order to obtain the possible largest catalogue of spectroscopic sub-pc MBHB candidates and to begin follow up observations on a significant sample of objects. Specifically the group of Tsalmantza et al. (2011; T11 hereafter) considered a sample of $\sim$ 59000 AGN and galaxies at redshifts $0.1 < z < 1.5$ and applied an automatic method - heteroscedastic matrix factorization (Tsalmantza & Hogg 2012) - able to detect spectra with two sets of emission lines that are consistent with a MBHB, a DPE, a chance superposition or a recoiling MBH. The second group of Eracleous et al. (2012; E12 hereafter) applied a principal component analysis technique (Boroson & Lauer 2010) to a list of 15900 AGN having redshift $z < 0.7$ to search for close MBHB or recoiling MBH candidates whose spectra display broad, single peaked Hβ lines with velocity offsets $\gtrsim$ 1000 km s^{-1} relative to the NELs. In particular, T11 identified 32 AGN with peculiar spectra among which 4 new sources have been interpreted as MBHB candidates in addition to the 5 objects already discussed in literature while the analysis of E12 yielded 88 candidates, 13 of which in common with the sample of T11. E12 obtained also follow-up spectroscopic observations of 68 candidates measuring accelerations of the off-set peaks in the range -120 to $+120$ km s^{-1} yr^{-1} in 14 objects. Although further observations on longer timescales are needed, the measure of a significant acceleration weaken the case of a recoiling MBH favoring that of a MBHB for these peculiar 14 candidates.

E12 focus on the case of a single-peaked broad line shifted from its nominal wavelength considering the MBHB or the recoiling MBH scenario as reasonable explanations for this peculiar spectroscopic feature. On the contrary the hypothesis of an accretion disk around a single AGN instead of two active, binary MBHs is believed much more likely for the case of two displaced BEL peaks. However our incomplete understanding of the structure and dynamics of the BLR does not allow to exclude that single-peaked shifted BELs could be related also to asymmetries in the BLR of a single MBH such as perturbations in the form of spiral arms in the class of models where the BLR is the surface of the accretion disk. Therefore all the candidates selected by both groups will be subject to follow-up observations (i) to monitor the shift of the BEL peaks in the optical spectra; (ii) to verify if the profiles of the broad UV emission lines show the same properties of the broad optical ones (this is not expected in the case of a DPE; e.g. Eracleous et al. 2009), and (iii) to study the environment and the morphology of these peculiar sources to find signs of a surrounding cluster and/or of an on-going interaction with close companions.

Chapter 4

A new spectroscopic technique: line flux ratios diagnosis

In this Chapter we investigate the possibility of identifying new observational features associated with close MBHBs at the longest-lived orbital stage between the disk-driven migration and the GW-inspiral. In particular we aim to select other spectroscopic signatures complementary to the presence of velocity off-sets between different emission line sets. Our analysis is intended to overcome the major drawbacks of the simple and direct Doppler-shift technique: the binary interpretation is not unique and requires extensive follow-up observations to be favored against other possible physical scenarios (see Ch. 3 for discussions on this point), and the search of MBHB candidates among the optical spectroscopic databases is limited to $z \sim 0.8$ since the rest-frame wavelength of the main narrow emission lines is $\gtrsim 3000$ Å.

Relying on the results presented below, we propose a new spectroscopic technique to select MBHB candidates at a redshift of $z \sim 2$ based on the identification of peculiar values of the flux ratio between BELs of different ionization potentials. In Sec. 4.1 we briefly describe the main features of the model we focus on, i.e. a MBHB embedded in a co-planar circum-binary disk. Sec. 4.2 and 4.3 present the results obtained respectively considering only the emission from the BLR bound to the active MBH and then adding the external contribution from the gap and the circum-binary disk. The main tools considered to carry out our study have been the photoionization code CLOUDY (version 08.00; Ferland et al. 1998) and a simple radiative transfer algorithm developed to analyze the results of high resolution SPH simulations. Finally in Sec. 4.4 we apply our technique to select a sample of

MBHB candidates at $1.9 \leq z \leq 2.1$ from the SDSS. We present the results of new spectroscopic observations obtained for a list of objects from our selected targets in order to search for a shift between the broad Hβ, MgII and CIV and the narrow [OIII] line that fall in the NIR band at the considered redshifts. The results discussed in this Chapter have been published in two works by Montuori et al. (2011; PaperI hereafter) and Montuori et al. (2012; PaperII hereafter).

4.1 Binary model

We consider a binary model similar to the one described in Sec. 3.2 to interpret the peculiar source SDSSJ0927: a sub-pc, circular MBHB with mass ratio $q \sim 0.3$, surrounded by a prograde circum-binary disk. We assume that the binary has already cleared a gap (i.e. a low density hollow region in the midst of the disk) confining its activity around the secondary MBH (M_2) fed by material flowing from the inner edge of the disk (e.g. Artymovicz & Lubow 1994, Ivanov et al. 1999, Cuadra et al. 2009, Rödig et al. 2012).

We work under the hypothesis that a small-scale accretion disk is maintained around M_2 throughout the binary orbital decay induced by the external torques from the circum-binary disk or by the emission of gravitational waves. As described in Haiman, Kocsis & Menou (2009), there exists a time in which the inner edge of the circum-binary thin disk can no longer follow the migration of the secondary as the inward viscous diffusion timescale in the disk becomes longer than the timescale of GW-driven inspiral ($t_{\rm GW}$). At such a separation the circum-binary disk decouples and the secondary might be no longer fueled. In this case, from the decoupling time on, the secondary active MBH is expected to consume its disc on a timescale that is $\gtrsim t_{\rm GW}$ (see eq. 21 of Haiman et al. 2009 for an expression of the viscous time in the case of a steady-state thin accretion disk). Thus we can assume that the activity of the secondary MBH can be sustained throughout the binary evolution.

In this scenario we consider that the Roche lobe of the secondary MBH ($R_{\rm L}$), whose expression is reported in eq. 3.1, is function of the orbital separation. Due to the orbital decay induced by viscous torques or GW emission, $R_{\rm L}$ decreases and we expect a progressive erosion of the BLR bound to M_2. BEL clouds no longer bound to the secondary MBH, experiences, outside $R_{\rm L}$, the tidal torque from the binary and are dragged away. We thus work under the hypothesis that the BLR is tidally truncated at $R_{\rm L}$ as the binary orbit shrinks under the action of external torques.

The question we want to address is the following: is there an observable signature in the emitted spectrum associated with this evolutionary scenario?

We expect that the emission from the peripheral BELs becomes inefficient below some critical orbital separation. This can be especially relevant for low-ionization lines in comparison to high-ionization ones, since the former are emitted preferentially at greater distances from the source of the ionizing flux. To this purpose, in the Sec. 4.2 we devise a method to compute the expected effects of the tidal truncation of the BLR of M_2 on the flux ratios between lines of low and high ionization potentials. Then we improve upon our first analysis in Sec. 4.3 considering the possible contribution to the BELs resulting from the reprocessing of the secondary MBH radiation by the gas of the circum-binary disk and by gas streams in the gap region flowing toward the MBHB.

4.2 Flux ratios: the broad line region of the active MBH

This Section presents the results reported in our exploratory PaperI where we investigate the possibility that the presence of a binary system can affect the flux ratios between broad emission lines originating from the BLR anchored to the secondary, active MBH.

We consider three of the most prominent BLR lines observed in the spectra of AGN: CIV, MgII and Hβ. We then focus on the flux ratios between those lines that can be simultaneously observed in an optical survey, such as the SDSS, up to redshift $z \sim 2$. In particular we compute the flux ratios between the lines of MgII and CIV ($F_{\rm MgII}/F_{\rm CIV}$) and those of MgII and Hβ ($F_{\rm MgII}/F_{\rm H\beta}$). The flux ratios are calculated for different sizes of the BLR around the secondary according to the scenario outlined in Sec. 4.1. For a circular binary with mass ratio q, secondary mass M_2 and separation a, the BLR is truncated at the Roche radius $R_{\rm L}$. The secondary is assumed to emit a luminosity $L = f_{\rm Edd} L_{\rm Edd}$ with a constant Eddington ratio $f_{\rm Edd}$. The greatest orbital separation ($a_{\rm o}$) is set under the assumption that $R_{\rm L}(a_{\rm o})$ coincides with the size ($R_{\rm BLR}$) of the BLR of an isolated MBH accreting at $f_{\rm Edd}$ as expected from the observational relation of $R_{\rm BLR}$ with the luminosity at 3000 Å (McLure & Jarvis 2002; see eq. 4.1), considering $\lambda L_\lambda(3000) \sim (1/5.6)\, L$

(Richards et al. 2006).

In order to compute the flux ratios at each separation, i.e. at each orbital period $P(a)$, we use the photoionization code CLOUDY (version 08.00; Ferland et al. 1998). To map the BELs we refer to the "locally optimally cloud" model (LOC; e.g. Baldwin et al. 1995).[1] Following Korista et al. (1997) and Korista & Goad (2000), we compute a grid of photoionization models assuming each cloud as a slab of constant gas density with solar metallicity and a clear view to the ionizing flux. The shape of the ionizing continuum is taken as one of the templates for a radio-quiet active galaxy stored as part of the CLOUDY code. The column density is set to $N_{\rm H} = 10^{23}\,{\rm cm}^{-2}$ and is kept fixed for all clouds. We consider the contribution of clouds with $8 \leq \log{(n_{\rm H}/{\rm cm}^{-3})} \leq 14$ and hydrogen ionizing flux $18 \leq \log{(\Phi_{\rm H}/{\rm cm}^{-2}\,{\rm sec}^{-1})} \leq 24$[2].

According to the LOC model the main properties of AGN spectra are dominated by selection effects of atomic physics and radiative transfer that determine, for each individual BLR cloud, the reprocessing efficiency of the ionizing continuum into line radiation. In this contest, it is assumed that there exists a spread in gas properties at each radius in the BLR. Therefore in order to compute the total BELs flux, we have to consider the contribution of each cloud lying in the density-flux plane spanned by the photoionization grid models. In particular it was shown that one can sum over all these contributions by making the simplifying assumption that clouds are distributed in gas density and distance following a weighting function separable in both variables (e.g. Baldwin et al. 1995).

The above assumptions usually refer to a spherically symmetric distribution of BLR clouds but they are still consistent with the case of a thick disk, which is the expected distribution for the BLR gas in the model described in Sec. 4.1. Both geometries imply a high covering factor which is in agreement with the observations (e.g. Gaskell 2009). On the other hand a high covering factor and a disk like geometry imply that the effect of cloud self-shielding may become relevant. In this case it has been shown that regions emitting BELs of different ionization potential are more clearly spatially separated (Gaskell 2009 and references therein). We expect that accounting for BLR self-shielding the effect of the the BLR erosion on the $F_{\rm MgII}/F_{\rm CIV}$ ratio would

---

[1] Considering current uncertainties on the nature and geometry of the BLR, we choose this model compared to more complex ones (see review of Gaskell 2009 and references therein).

[2] See Appendix II

be even stronger than what obtained in our calculations.

In our study, we consider the case of a uniform distribution of cloud distances and densities, and a second case in which the weighting function is a power law with index -1 in both variables (power-law model, here on). We set the density range for the two different distributions such that at the largest orbital separation the computed flux ratios are consistent with the typical values observed in the AGN spectra, i.e. $F_{\rm MgII}/F_{\rm CIV} \sim 0.3 - 0.4$ (see Sec. 4.4). In particular we set: $9 \leq \log{(n_{\rm H}/{\rm cm}^{-3})} \leq 12.6$ for the homogeneous model, and $9 \leq \log{(n_{\rm H}/{\rm cm}^{-3})} \leq 14$ for the power-law model. Considering the adopted cloud distributions in density and space, the resulting mean number density as function of distance are: $n_{\rm H} \sim 2 \times 10^{12}\,{\rm cm}^{-3}$, constant with radius for the uniform BLR model, and $n_{\rm H} \sim 8 \times 10^{12}\,(r_{\rm in}/r)\ {\rm cm}^{-3}$ for the power law case, where $r_{\rm in}$ is the inner BLR radius. In the power law case the contribution from higher density gas at greater distances is less relevant than in the uniform model. The need of a higher density limit in the power law model to reproduce the observed values of the $F_{\rm MgII}/F_{\rm CIV}$ ratio can be therefore understood considering that the MgII line is more efficiently reprocessed at higher densities and lower fluxes than the CIV line.

4.2.1 Results

Fig. 4.1 shows the flux ratios $F_{\rm MgII}/F_{\rm CIV}$ and $F_{\rm MgII}/F_{\rm H\beta}$ as a function of the Keplerian orbital period of the MBHB, for $q = 0.3$ and for a secondary with $M_2 = 10^7, 10^8, 10^9\ {\rm M}_\odot$. The upper panel refers to the case of uniformly distributed BLR clouds, while the lower to the power-law model.

We find that the ratio $F_{\rm MgII}/F_{\rm CIV}$ is a decreasing function of the orbital separation, and so of P, and therefore it can be regarded as a possible diagnostic tool in the spectroscopic search of binary systems. On the other hand the $F_{\rm MgII}/F_{\rm H\beta}$ ratio is fairly constant apart from a sharp decline present only in the case of a uniform clouds distribution, that will be discussed below. Therefore $F_{\rm MgII}/F_{\rm H\beta}$ is not sensitive to the truncation of the BLR while $F_{\rm MgII}/F_{\rm CIV}$ shows lower values for closer separations in both BLR models and is already reduced of an order of magnitude before the drop that occurs in the uniform distribution case. These results are consistent with what expected considering that lines of different ionization potential, such as those of CIV and MgII, are preferentially emitted in spatially separated regions.

As mentioned before, in the case of a uniform BLR, both flux ratios decrease rapidly around a critical orbital period $P_{\rm drop}$. This rapid decay is not observed for the case of a power-law BLR distribution. As described above, observations require that the BLR cloud density does not exceed $\log(n_{\rm H}/{\rm cm}^{-3}) \lesssim 12.6$ for the uniform model. Higher densities needed in the power-law model can still contribute to the MgII line emission at closer orbital separations, preventing the occurrence of the drop in the line flux ratio. However we expect to observe at most a few binary systems at such small periods ($P < P_{\rm drop}$) because of the short coalescing timescale for GW emission.

Vertical lines refer to the orbital period $P_{\rm dec}$, for a selected binary, below which the binary decouples from the circum-binary disk. As described in Sec. 4.1, at this stage the MBHB is already in the GW-driven inspiral regime and in Fig. 4.1 we report the corresponding times for GW-driven coalescence, in the range $3 \times 10^3 - 10^6\,$yr. The period at the binary-disk decoupling is computed following Haiman et al. (2009) for a steady geometrically thin accretion disk (see their equations 30). We notice that for the parameters chosen in our calculation the decoupling occurs at $P_{\rm dec} \gtrsim P_{\rm drop}$ where there is more chance to observe binary systems and the values of the $F_{\rm MgII}/F_{\rm CIV}$ ratio can be already reduced up to an order of magnitude, as discussed before.

Fig. 4.2 carries the same information of Fig. 4.1 but expresses the decrease in the flux ratios as a function of the velocity of the secondary MBH relative to the center of mass of the binary. The velocity is in principle measurable as Doppler-shift between the BELs and the narrow lines emitted from gas at larger distances. The velocity reported in Fig. 4.2 refers to the maximum observable velocity offset, corresponding to a binary seen edge-on and at at one of the two orbital nodes.

Fig. 4.3 illustrates the effect of varying the Eddington ratio for the case of a secondary with $\mathrm{M}_2 = 10^7\ \mathrm{M}_\odot$, $q = 0.3$ and for a uniform BLR. The flux ratios curves shift to shorter periods for lower Eddington ratios. The unperturbed outer radius of the BLR of the secondary is proportional to its luminosity through the $R_{\rm BLR} - L$ relation of McLure & Jarvis (2002) given by eq. 4.1, as in the case of isolated MBHs. This implies that the smaller BLR of a secondary accreting at a lower pace starts to be tidally perturbed at smaller binary separations. On the other hand for lower values of $f_{\rm Edd}$ the binary-disk decoupling may occur at greater orbital separations, due to the longer viscous time scale.

According to the results presented above, the spectrum of a MBHB, at the orbital stage of viscous/GW driven migration, shows decreased line flux ratios, compared to what observed for single black holes, due to the erosion

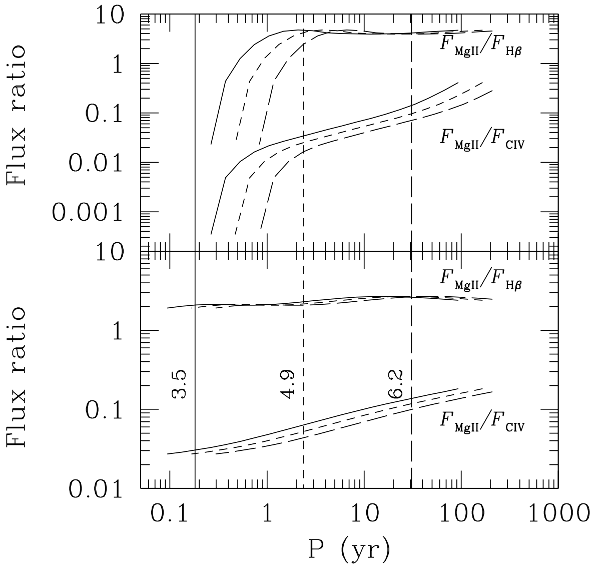

Figure 4.1: Flux ratios between the broad emission lines of MgII and CIV ($F_{\rm MgII}/F_{\rm CIV}$) and those of MgII and Hβ ($F_{\rm MgII}/F_{\rm H\beta}$) as function of the orbital period P for a MBHB with different total masses. The mass ratio is set to $q = 0.3$ and the Eddington ratio to $f_{\rm Edd} = 0.1$. Solid/dashed/long-dashed lines refer to a secondary mass of $M_2 = 10^7 - 10^8 - 10^9$ $\rm M_\odot$, respectively. The vertical lines mark the orbital period at the time the binary detaches from the circumbinary disk. Upper (Bottom) panel corresponds to the uniform cloud (power-law) model.

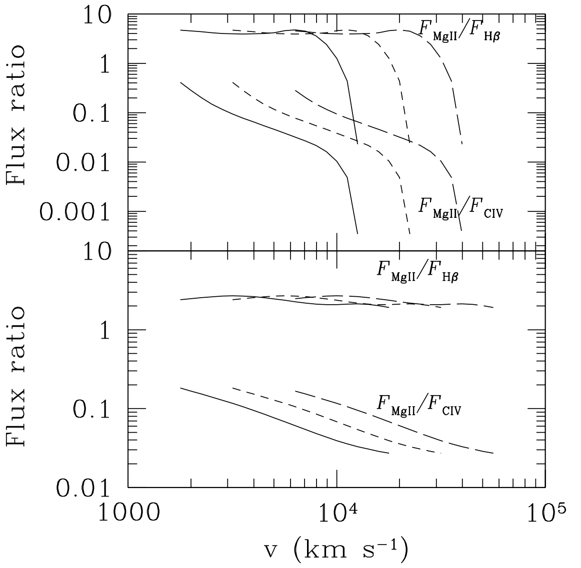

Figure 4.2: Line flux ratio (as in Figure 4.1) as a function of the secondary MBH orbital velocity relative to the center of mass. The velocity reported here would express the velocity offset between the BEL and the NEL systems for a MBHB seen edge-on and at one of the two orbital nodes.

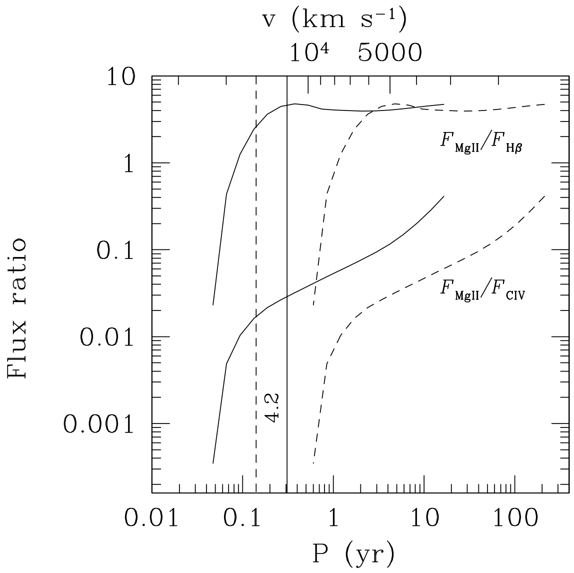

Figure 4.3: Line flux ratios for two different values of $f_{\rm Edd}$, for the uniform cloud model with $q = 0.3$ and $M_2 = 10^7$ $\rm M_\odot$. Solid (dashed) lines refer to $f_{\rm Edd} = 0.01$ (0.3). The line ratio curves shift to shorter periods for lower values of $f_{\rm Edd}$ while the opposite occurs for higher Eddington ratios. As explained in the text, this is due to the correlation between the unperturbed outer radius of the secondary BLR and its luminosity. Vertical lines correspond to the binary-disk decoupling. Lower values of $f_{\rm Edd}$ imply longer periods in correspondence of binary-disk decoupling because of the longer viscous time scale.

of the BLR at the Roche lobe radius of the active secondary. In light of our findings, AGN spectra characterized by $F_{\rm MgII}/F_{\rm CIV} \lesssim 0.1$ could be interpreted as a signature of MBHBs with separations $\lesssim 0.1\,$pc, and orbital periods $P \lesssim 50\,$yr for a total binary mass in the range of $10^7 - 10^9 \rm M_\odot$. This flux decrease amounts to nearly three orders of magnitude for binary systems at the shortest separations, in the case of BELs emitted by a uniform distribution of cloud properties. For clouds with steeper distributions in space and density the flux ratios can be diminished of a factor $\lesssim 10$.

As noticed before, the flux ratio is particularly low when the MBHB is in the short-lived evolutionary stage of GW inspiral. In this phase, the binary often reaches the critical orbital distance below which the circumbinary disk decouples from the inspiralling MBHs. In principle, this could be important when considering the potential contributions to the observed BELs not included in our calculations. Depending on the uncertain physical conditions of the gas in the surroundings of the binary, the gas located at the inner edge of the circum-binary disk may contribute to the BELs, making the predicted diminished values of the flux ratios more difficult to observe. We expect a weakening of the potential emission from clouds residing in the circum-binary disk, should the emission be present, since the disk edge freezes and the distance between the emitting MBH and this gas keeps on increasing. On the other hand the radial extent of the BLR of the active MBH is already significantly reduced before the binary-disk decoupling so that the eventual emission from the circum-binary material could become the dominant contribution already at $P > P_{\rm dec}$. These considerations will be further elaborated in the following Section where we will focus on the emission from the denser matter located at the disk inner edge and inflowing from it onto the MBHs, and on the presence of lower density gas in the gap region.

4.3 Flux ratios: the central cavity and the circum-binary disk

In this Section we report the results of PaperII where we improve upon our earlier investigation discussed in the previous Section. In particular we study the contribution to the BELs resulting from the reprocessing of the MBH radiation by the gas of the circum-binary disk and by the gas streams in the gap region flowing toward the MBHB. The emission from illuminated gas not bound to the active MBH was indeed neglected in Sec. 4.2. Sections 4.3.1 and 4.3.2 describe how we extend our previous results, guided by a qualitative analysis, and later by a more quantitative study carried out with data taken from SPH numerical simulations.

4.3.1 Key spatial scales along binary evolution

In order to overcome some of the simplifying assumptions made in the our previous investigation, we consider here the potentially observable contribution from gas in the circum-binary disk surrounding the MBHB. We start with a schematic view of the spatial scales relevant to our binary evolutionary model. Two characteristic radii are present: the Roche Lobe Radius $R_{\rm L}$

around the secondary, only active MBH and the inner edge of the circum-binary disk $R_{\rm gap}$. The Roche Radius $R_{\rm L}$, given by eq. 3.1, and $R_{\rm gap} = 2a$ (e.g. Artymovicz & Lubow 1994) are plotted in Fig. 4.4 as function of the binary orbital separation a, for a circular MBHB with mass ratio $q = 0.3$ and mass of the secondary $M_2 = 10^8$ M$_\odot$.

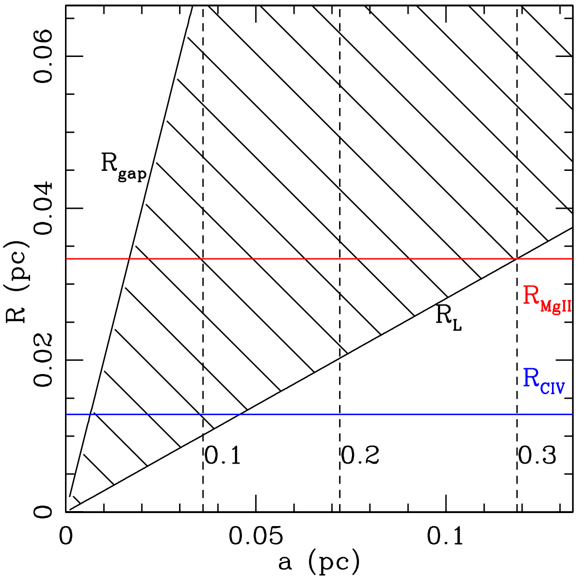

Figure 4.4: Schematic view of the most relevant spatial scales in our MBHB model as a function of a. The binary is interacting with a circum-binary disk, and the secondary MBH is the only active member of the system. The binary mass ratio is $q = 0.3$, the secondary MBH mass is $M_2 = 10^8$ M$_\odot$. The two solid black lines represent the radii of the Roche lobe ($R_{\rm L}$) around the secondary MBH, and the radius of the inner edge of the circum-binary disk ($R_{\rm gap}$), respectively. The shaded area in between these two lines corresponds to the lower density region in the central part of the circum-binary disk, i.e. the gap. The red and blue horizontal lines correspond to the values of $R_{\rm BLR}$ computed from the radius-luminosity relationship for the MgII and the CIV emission lines, respectively. The secondary MBH is assumed to be active as an AGN with an Eddington ratio of 0.1. The vertical dashed lines mark the orbital separations corresponding to different values of $F_{\rm MgII}/F_{\rm CIV}$ computed for the material bound to the active MBH, orbiting inside $R_{\rm L}$ (see the text for more details).

The shaded area corresponds to the gap region between $R_{\rm L}$ and $R_{\rm gap}$, while the horizontal lines correspond to the values of $R_{\rm BLR}$ calculated from the following radius-luminosity relations for the CIV ($R_{\rm CIV}$, in blue, Kaspi et al. 2007) and the MgII ($R_{\rm MgII}$, in red, McLure & Jarvis 2002):

$$R_{\rm CIV} = 0.002 \times \left(\lambda L_{1350}/10^{43}{\rm erg\,s^{-1}}\right)^{0.55}\ {\rm pc} \tag{4.1}$$

$$R_{\rm MgII} = 0.022 \times \left(\lambda L_{3000}/10^{44}{\rm erg\,s^{-1}}\right)^{0.47}\ {\rm pc} \tag{4.2}$$

where $\lambda L_{1350} = 1/5L$ and $\lambda L_{3000} = 1/5.6L$ are the continuum luminosities at 1350Å and 3000Å, and L is the bolometric luminosity (Richards et al. 2006). We consider the case of a secondary MBH shining with a constant Eddington ratio set to $f_{\rm Edd} = 0.1$. The vertical dotted lines mark the orbital separations corresponding to different values of $F_{\rm MgII}/F_{\rm CIV}$ (0.1, 0.2 and 0.3 as indicated in the figure) for the lines emitted by the gas of the BLR located inside $R_{\rm L}$. These orbital separations are computed as described in Sec. 4.2. In particular, the emission from the BLR around the secondary MBH is modelled according to the LOC model (e.g. Baldwin et al. 1995), adopting a power-law with index set to -1 for the clouds radial distance from the active source, and a uniform distribution for the clouds density at each radius. The hydrogen number density is set in the range $10^9{\rm cm}^{-3} \leq n_{\rm H} \leq 6\times10^{12}\,{\rm cm}^{-3}$ so that at $a_0 \simeq 0.12$ pc, the starting point where $R_{\rm L} = R_{\rm MgII}$, $F_{\rm MgII}/F_{\rm CIV}$ is consistent with the typical values observed for standard AGN, i.e. $\sim 0.3-0.4$ (see Sec. 4.4).

Moving toward smaller MBHB separations, we highlight the occurrence of intervals possibly characterized by different observational signatures. As the binary separation shrinks, $R_{\rm L}$ becomes smaller than $R_{\rm MgII}$. According to our previous results, this implies a reduction in the ratio $F_{\rm MgII}/F_{\rm CIV}$ for the BELs associated with the BLR of the secondary MBH. We consider the results of Sec. 4.2.1 to be valid until the flux ratio drops to a value $F_{\rm MgII}/F_{\rm CIV} \sim 0.1$ at an orbital separation of $a \simeq 0.04$ pc, corresponding to a period of $P \simeq 40$ yr, for the selected binary parameters. The contribution coming from the material not bound to the secondary active MBH can be still neglected at these separations considering that (i) the gas density in the gap region is expected to be much lower than the density relative to standard BLRs, and the BELs are efficiently reprocessed only at high densities; and that (ii) the inner edge of the circum-binary disk $R_{\rm gap}$ is located at a distance $> 2R_{\rm MgII}$ so that the ionizing flux reaching the higher density material associated with the outer circum-binary disk would be more than an order of magnitude lower relative to the flux intercepted by the gas bound to the active source.

As the semi-major axis shortens further on, this spectroscopic signature is not expected to be a good tracer of the presence of a sub-pc MBHB, since the additional contribution of the circum-binary disk cannot be any longer neglected, yielding an increase in $F_{\rm MgII}/F_{\rm CIV}$. At intermediate separations of the order of $a \simeq 0.02$ pc, where $R_{\rm gap} \approx R_{\rm MgII}$, $F_{\rm MgII}/F_{\rm CIV}$ could be even higher than what typically observed for isolated AGN since the circum-binary disk could start to contribute significantly to the MgII line while the CIV emission flux could be still reduced relative to the case of a single AGN since $R_{\rm L} < R_{\rm CIV} < R_{\rm gap}$. At the smallest orbital separations, of the order of $a < 0.01$ pc, where $R_{\rm gap} \lesssim R_{\rm CIV}$, the higher density gas of the circum-binary disk could efficiently reprocess both the CIV and the MgII emission lines bringing $F_{\rm MgII}/F_{\rm CIV}$ back to the values observed for standard BLRs.

4.3.2 Reprocessing of radiation in circum-binary disks

In Sec. 4.3.1 we qualitatively showed that the flux ratio of the MgII and CVI emission lines varies with the MBHB separation, and that this change may not be monotonic with decreasing a due to the contribution to the line flux from dense gas present in the circum-binary disk, depending on the relative position of the two critical radii $R_{\rm CVI}$ and $R_{\rm MgII}$ with respect to $R_{\rm gap}$ and $R_{\rm L}$.

To proceed more quantitatively in our analysis, we model the spectroscopic signatures of a close MBHB applying here a simple line radiative transfer algorithm on data extracted from a simulated model of a circum-binary gas disk. The model self-consistently accounts for the presence of a low (but finite) density region, i.e. the gap, and of gas streams that leaking out through the inner edge of the disk are accreted by the binary.

In particular we consider the numerical results presented in Sesana et al. (2012, S12 hereafter) who used a modified version of the SPH code Gadget-2 (Springel 2005, Cuadra et al. 2009) to model the complex feeding process of a MBHB embedded in a coplanar, co-rotating circum-binary accretion disk. The orbital separation in the simulation, $a \simeq 0.01$ pc, is in the interval appropriate to test our working hypothesis, namely that the line fluxes from MgII and CVI can have a contribution from dense gas in the circum-binary disk. At the considered orbital separation, the simulated binary system is still dynamically coupled with the circum-binary disk, while its orbital decay is dominated by the emission of gravitational waves (see S12 and references therein).

We map the simulated gas density field on a cubic, three dimensional coarse grid[3], and in the following we will refer to the cubic grid elements as pixels. Pixels are then exposed to the ionizing radiation originating from gas accreting in the putative small-scale disk around the secondary MBH. The small-scale accretion disk is assumed to be co-planar with the binary, and the ionizing emission is modeled adopting a cosine-like dilution along the disc axis to mimic thermal emission from an optically thick (geometrically thin) accretion flow (e.g. Ivanov et al. 1999, Shakura & Sunyaev 1973). In the SPH simulation at hand the gas accretion rate onto the MBH is given by summing over all particles crossing the MBH sink radius in a time-step. In our analysis, we select simulation snapshots corresponding to the secondary MBH radiating with a luminosity of 0.1 the Eddington luminosity (assuming 10% radiative efficiency).

The gas ionization state of the simulation pixels is computed using the code CLOUDY (version 08.00; Ferland et al. 1998). We adopt the AGN SED template stored in the code, scaled to the appropriate level given by the coordinates of the considered pixel. The ionization state of the gas is determined moving from the innermost pixels to the outer region along straight ray paths. To trace the cumulative effect of radiation absorption along a ray path, we make a net distinction between pixels which are optically thick and optically thin to the HI ionizing continuum. We assume that a pixel is not reached by ionizing radiation if at least one optically thick pixel is met along a ray. Our treatment is clearly a simplified description of the real radiative transfer, as we assume complete (zero) absorption for $\tau \geq 1$ ($\tau < 1$). However this procedure greatly facilitates the analysis process, and at the same time captures the basic feature of sharp ionization fronts expected in the circum-binary gas.

The next step consists in the modeling of the BELs. A self-consistent model for the BLR is still lacking as it is poorly constrained by the observations. Despite these limitations, the origin of the BELs is generally attributed to compact, dense condensations rapidly moving in a hotter intercloud medium (e.g. Osterbrock & Ferland 2006). Though the density of such unresolved clouds (estimated to be $\gtrsim 10^{10}\,\mathrm{cm}^{-3}$) is well above the maximum density given by our SPH simulation, we can use the gas distribution determined in the SPH simulation as a physically motivated "background" density field to model the spatial distribution of the BEL clouds. To this aim, we

---

[3] The results of our analysis are not significantly affected by the choice of the grid geometry and resolution.

select the densest ($n_{\rm H} > 10^8\,{\rm cm}^{-3}$) ionized regions of the circum-binary disk and of the streams flowing from its inner-edge, and there we superimpose a distribution of gas overdensities mimicking the BEL clouds. Operatively, we add a gaseous clump in all illuminated pixels whose hydrogen number density is above a given threshold. Such limiting value is set so that the total number of pixels embedding BEL clumps do not exceed the 10% of the total number of ionized pixels. The density of each BEL clump is set randomly from a uniform distribution in the range $10^8\,{\rm cm}^{-3} \leq {\rm n_H} \leq 10^{12}\,{\rm cm}^{-3}$. We further assume that the clumps filling factor is $\ll 1$, so that the cumulative shielding effect along ray paths can be neglected. As discussed in the following section, we manage to check the consistency of our expectations discussed in Sec. 4.3.1 without any other constraint on the distribution of such BEL clumps.

Once the BEL clumps are added, we use again CLOUDY to compute their line emission properties. As a final remark, we caution that we do not model the emission coming from the gas orbiting inside the Roche lobe of the secondary. The numerical resolution is not high enough to describe the properties of the material located at radii $\ll 0.5\,a$. We note that the main interest of our work here is to compute the broad line emission from the material not bound to the active MBH but rather bound to the binary, in order to test our qualitative expectations.

4.3.3 Results

In this Section we describe the results from a simulation of a close MBHB with $a \simeq 0.01$ pc, a secondary MBH with mass $M_2 \simeq 10^8$ ${\rm M}_\odot$ and mass ratio $q \simeq 0.3$, surrounded by a co-planar, co-rotating circum-binary disk with a gap. In particular, we consider a snapshot where the secondary active MBH accretes with $f_{\rm Edd} \simeq 0.1$ (we adopt a radiative efficiency of 0.1). As discussed in Sec. 4.3.1, the binary model implies that $R_{\rm CIV} \lesssim R_{\rm gap} < R_{\rm MgII}$. Therefore we expect that the gas in the circum-binary disk would give an important contribution to the BELs.

In Fig. 4.5 we show our results superimposing the intensity contour plot of the MgII and the CIV lines on the density map of the selected snapshot. As described in Sec. 4.3.2, the BELs clouds are distributed on top of the cubic grid adding a gaseous clump to those illuminated pixels whose hydrogen number density is $n_{\rm H} \geq 10^8\,{\rm cm}^{-3}$. These pixels are located in the gap region and in a thin layer above the circum-binary disk midplane, within a

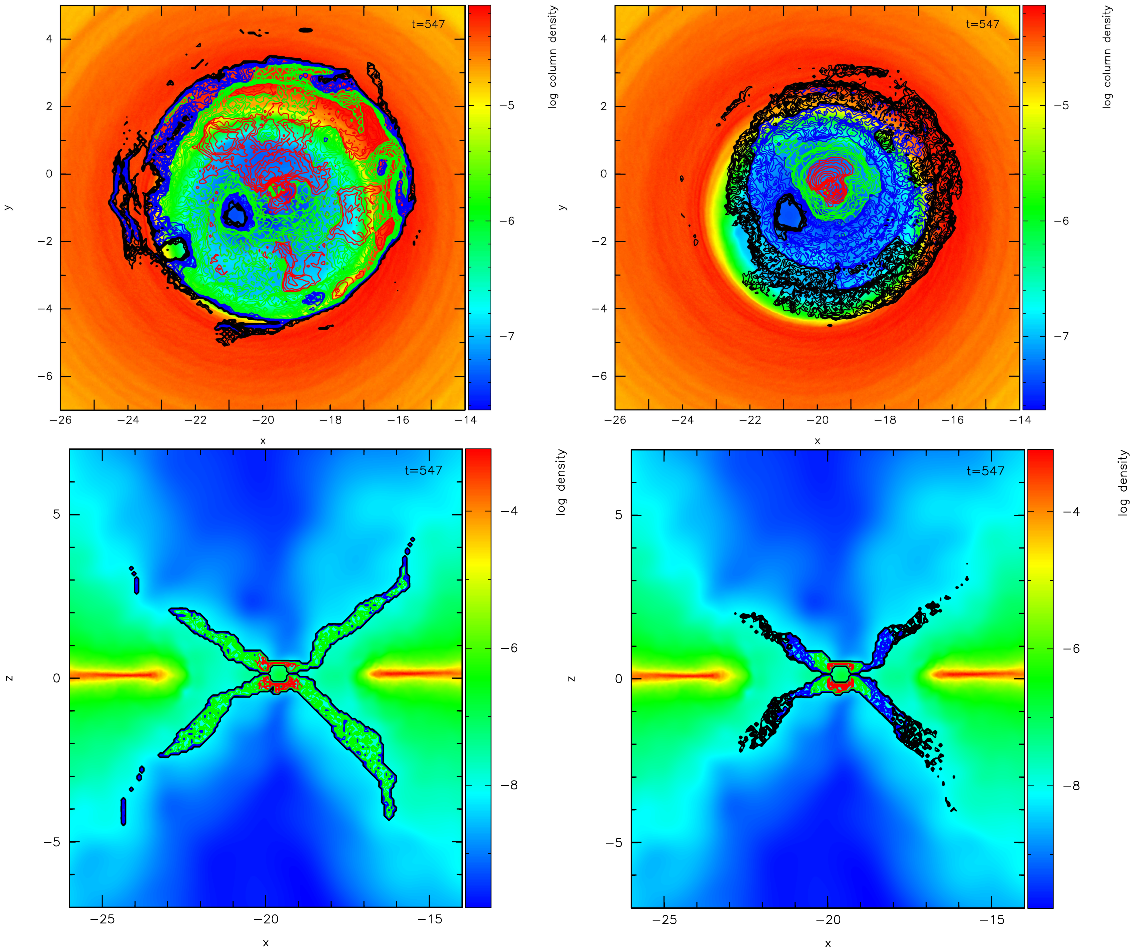

Figure 4.5: Contour plots of the MgII (left panels) and CIV (right panels) emission line intensity superimposed on the density map of a snapshot taken from a SPH numerical simulation of a massive MBHB embedded in a coplanar, corotating circum-binary disk. The upper panels show the projected intensity map for a face on view relative to binary orbital plane superimposed on the surface density map. The lower panels correspond to an edge-on view with a slice of the intensity map overlaid on a slice of the density map, both taken in the zx plane at the y-coordinate of the secondary MBH. The secondary coordinates are (-19.6, -0.9, 0.1). The lower density gas of the gap region has green and blue colors in the density maps while the higher density gas of the surrounding circum-binary disk is colored in red and yellow. Similarly the color scale of the emission line contour levels spans two order of magnitudes, uniformly spaced in the logarithm, starting from the maximum intensity value in the map with red going to green, blue and black. These plots are obtained following the post-process analysis procedure described in more detail in the text.

radius $r \lesssim 2R_{\rm MgII}$ (where $2R_{\rm MgII} \simeq 0.065\,$pc, corresponding to $\simeq 6$ internal unit lengths of the simulation). As shown in Fig. 4.5, the emission line intensity maps follow the spatial distribution of the gaseous clumps. We obtain $F_{\rm MgII}/F_{\rm CIV} \gtrsim 0.2$ for the emission coming from the gaseous over-densities. The relative contribution to the CIV and the MgII lines coming from the gap region is of the order of 67% and 34%.

In order to verify that our results are not affected by the details of the post-process procedure, we perform a second analysis starting from the same snapshot but considering an isotropic ionizing source. Although the number of illuminated pixels is 30% larger in this case, the results are consistent with the previous analysis. The emission coming from the gap region increases since the ionizing flux is not zero in the direction perpendicular to the polar axis. In this case we have $F_{\rm MgII}/F_{\rm CIV} \gtrsim 0.15$ and the relative contribution to the CIV and MgII lines from the gaseous clumps in the central cavity is of the order of 73% and 25% respectively. We point out that the simplified procedure adopted for the distribution of the over-densities does not take into account that the formation of the gaseous clumps might be disfavored in the gap region, characterized by lower densities and higher temperatures. For this reason $F_{\rm MgII}/F_{\rm CIV}$ could be higher than what computed with our analysis since we might be overestimating the contribution to the CIV line coming from the clumps closer to the ionizing source.

According to Sec. 4.3.1, we expect to select MBHB candidates with a peculiarly reduced value of $F_{\rm MgII}/F_{\rm CIV}$ when the circum-binary disk is still too far from the active source and does not give a significant contribution to the BELs. As shown in Fig. 4.4, $F_{\rm MgII}/F_{\rm CIV}$ computed for the BLR around the secondary MBH is reduced to a value of $\simeq 0.1$ at an orbital distance of the order of $a \simeq 0.04$ pc, while the inner edge of the circum-binary disk $R_{\rm gap}$ is located far out at radii $\simeq 2R_{\rm MgII}$. In order to quantitatively check such predictions we perform an additional test using the same snapshot and rescaling the unit length by a factor of 4 so that the orbital separation of the simulated binary system is $a \simeq 0.04$ pc. According to eq. 14 of S12, the rescaling keeps a disc-to-binary mass ratio of a few percent, still consistent with the value of 1.5×10^{-2} assumed in the simulation for $a \simeq 0.01$ pc. Now we can compare the emission fluxes obtained with the distribution of gaseous clumps considered for the $a \simeq 0.01$ pc case with the emission fluxes computed for an equal number of clumps (with the same total mass and densities) superimposed on the snapshot rescaled at $a \simeq 0.04$ pc. In particular, the gaseous clumps are added to the rescaled snapshot pixels that are ionized by the active source and whose number density is $n_{\rm H} > 5 \times 10^6\,{\rm cm}^{-3}$.

With this procedure we find that the contribution to the CIV and the MgII fluxes from the circum-binary disk, at a binary separation of $a \simeq 0.04$ pc, is reduced relative to the case with $a \simeq 0.01$ pc by a factor of $\simeq 10$ and $\simeq 100$, respectively. This is consistent with our expectations considering that on average the ionizing flux reaching the high density clumps is in this case reduced of an order of magnitude. According to the model assumed for the cloud distribution in the BLR of the secondary MBH, at the considered orbital separation the BELs flux reduction, relative to the fluxes computed at a_0, is of the order of 28% and 75% for the CIV and the MgII line, respectively. According to our results, the contribution from the outer disk to the CIV line can be neglected while that to the MgII line corresponds to an increase of $\sim 10\%$. Even considering this external emission, we obtain $F_{\rm MgII}/F_{\rm CIV} \sim 0.15$ that is still reduced relative to its typical values for single AGN. This is consistent with our MBHB selection criterion, as discussed in Sec. 4.2, of $F_{\rm MgII}/F_{\rm CIV} \lesssim 0.1$ considering both the uncertainties in the calculations and in the BLR model.

Fig. 4.6 shows, as function of the mass of the secondary active MBH, the minimum and maximum values of the orbital period P (upper panel) and of the orbital velocity v_2 (lower panel) of the active MBH relative to the binary center of mass, within which we expect to select a MBHB from its peculiarly reduced value of $F_{\rm CIV}/F_{\rm MgII}$. The corresponding MBHB separations can be inferred given the relation $a \simeq 0.08\,(M_2/10^8{\rm M}_\odot)^{1/3}(P/100\,{\rm yr})^{2/3}$ pc for a binary mass ratio of 0.3.

Relying on the results discussed so far, the limiting values for P and v_2 are obtained requiring that (i) $R_{\rm gap} \gtrsim 2R_{\rm MgII}$, so that the circum-binary disk contributes to the MgII line at most by 10% relative to the typical BEL flux of a single AGN; (ii) $F_{\rm MgII}/F_{\rm CIV} \lesssim 0.15$ even considering the additional contribution from the gas not bound to the active MBH. We set the upper limit for $F_{\rm MgII}/F_{\rm CIV}$ to 0.15 on the basis of the observed distribution inferred from $\simeq 6000$ quasar spectra in the SDSS archive ($\simeq 90\%$ of the sources has a $F_{\rm MgII}/F_{\rm CIV} > 0.15$, see Sec. 4.4). Maximum periods (minimum velocities) depend on the way we model the BLR around the active MBH. In the upper panel of Fig. 4.6, describing the run of P with M_2, the lower solid line refers to the BLR model considered in the previous sections, i.e. a uniform density distribution and a power-law with index -1 for the radial distances distribution (hereon model A). The upper solid line corresponds to the case of a power-law with index -0.5 for the radial distribution while the densities are

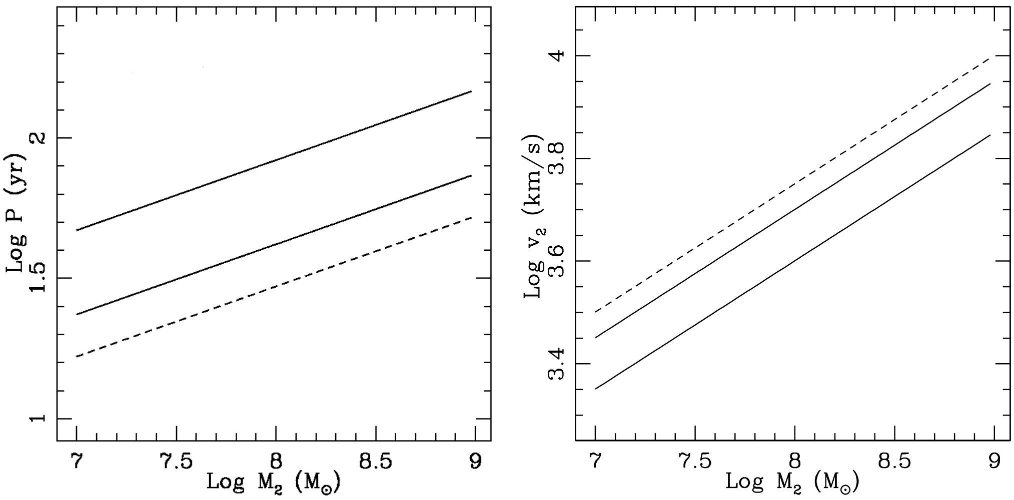

Figure 4.6: Range of orbital parameters of MBHB candidates characterized by a peculiar value of $F_{\rm MgII}/F_{\rm CIV}$. The orbital period P (upper panel) and the orbital velocity of the active MBH v_2 (lower panel) are plotted as function of the mass M_2 of the active MBH. The MBH is accreting with $f_{\rm Edd} = 0.1$, and the binary mass ratio is $q = 0.3$. Two different models for the BLR bound to the active MBH are considered. Solid lines refer to the maximum orbital period (minimum orbital velocity) for the two considered BLR models. Dashed lines indicate the minimum period and the corresponding maximum orbital velocity. These parameters are the same for both BLR models (see text for details).

set uniformly in the range $10^9 {\rm cm}^{-3} \leq n_{\rm H} \leq 2.5 \times 10^{12} {\rm cm}^{-3}$ (hereon model B). In the lower panel for v_2 the upper and lower solid lines refer to model A and model B, respectively. For model B (which has a flatter radial distribution and a lower upper limit for the density range relative to model A) the emission coming from the outer part of the BLR is more relevant and $F_{\rm MgII}/F_{\rm CIV}$ can be significantly reduced also at higher orbital separations. However in model B we notice that $F_{\rm MgII}/F_{\rm CIV}$ computed at the starting orbital separation, corresponding to $R_{\rm L} = R_{\rm MgII}$, is lower of a factor of ~ 0.8 because of the lower density assumed for the BLR clouds. Therefore we consider the maximum orbital values computed with model B as upper limits. Moreover for BLR clouds distributed uniformly in both radius and density, the effect of the flux ratio reduction would be even stronger than the models considered in the figure. On the other hand the BEL fluxes would be so diminished as the orbital separation shrinks that the contribution from the external gas would be more effective in increasing $F_{\rm MgII}/F_{\rm CIV}$ to its standard values. In this case there would be a narrower range of orbital parameters suitable to observe a peculiar $F_{\rm MgII}/F_{\rm CIV}$ because of the presence of a close MBHB.

Solid and dashed lines in Fig. 4.6 scale as $M_2^{1/4}$. The scaling can be simply understood considering that the maximum and minimum orbital separations (thus the maximum and minimum P) correspond to a fixed ratio $R_{\rm L}/R_{\rm BLR}$. This means that $R_{\rm L,max/min} \propto f_{\rm Edd}^{1/2} M_2^{1/2}$ (see the $R_{\rm BLR}$-luminosity relations reported in Sec. 4.3.1), where the subscript $_{\rm max/min}$ refers to the maximum/minimum value of the parameter. Since $a \propto R_{\rm L}$, we obtain

$$P_{\rm max/min} \propto \left(\frac{a^3_{\rm max/min}}{M_2}\right)^{1/2} \propto \frac{(f_{\rm Edd}^{1/2} M_2^{1/2})^{3/2}}{M_2^{1/2}} \propto M_2^{1/4} \tag{4.3}$$

and

$$v_{2,\rm max/min} \propto \left(\frac{M_2}{a_{\rm min/max}}\right)^{1/2} \propto \left(\frac{M_2}{f_{\rm Edd}^{1/2} M_2^{1/2}}\right)^{1/2} \propto M_2^{1/4} \tag{4.4}$$

As noticed before, until now we have worked under the assumption of a circular binary orbit so that there is a fixed relation between the Roche radius of the secondary MBH and the binary semi-major axis. A number of numerical studies showed that the interaction with a circum-binary disk can bring the eccentricity of a binary system up to a constant saturation value which is fairly high, i.e. $e \sim 0.6 - 0.8$ (e.g. Cuadra et al. 2009, Rödig et al. 2011). The Roche lobe radius is ill-defined for an eccentric binary. On an eccentric orbit with $e \sim 0.6$, the active, secondary MBH has an apocenter (pericenter) ~ 1.6 (~ 0.4) times larger (smaller) than a circular orbit. Under these circumstances, the BLR of the secondary MBH may have no time to re-expand after the truncation at the pericenter passage due to the characteristics of the periodic inflows of material onto the MBHs. The analysis presented in Sec. 4.3.3 for the $a \simeq 0.01$ pc case would not be significantly affected by the precise value of the Roche lobe of the secondary MBH. Indeed, $R_{\rm L} \lesssim 0.15\, R_{\rm MgII}$ in both cases so that the circum-binary disk would still give the major contribution to the BELs.

Results are different when most of the emission comes from the material bound to the secondary MBH, as in the $a \simeq 0.04$ pc case. In this case, if the BLR of the secondary MBH does not expand after the pericenter passage, $F_{\rm MgII}/F_{\rm CIV}$ would be that computed for a binary with a semi-major axis reduced by a factor $\simeq 2.5$. Then, it could be possible to select binary candidates with longer orbital periods compared to the circular case. If instead the BLR expands to fill $R_{\rm L}$ at the apocenter the flux ratio reduction would be less significant. The chance to select a binary candidate before the circum-binary disk starts to contribute to the BELs would be lower, and more affected by the details of the BLR model.

Low values of the line flux ratios should be accompanied by at least one or two of the following signatures. The first signature would be the presence of de-projected velocity offsets between the BELs and the NELs of the order $\sim (2000-10,000)(0.1/f_{\rm Edd})^{1/4}$ km s^{-1} for a secondary MBH mass in the range $M_2 \sim 10^7 - 10^9 {\rm M}_\odot$ and a mass ratio of 0.3. The second would be a change in luminosity over the orbital period P. The results of different works indicate that the accretion rate on the active MBH can be modulated on the timescale of the binary orbital period (e.g. Röedig et al 2011 and references therein). The line emission features investigated in our study are occurring at orbital periods $P \sim 20 - 200(f_{\rm Edd}/0.1)^{3/4}$ yr. Therefore we expect that periodicity both in velocity-offsets and in continuum luminosity can be used to verify the binary hypothesis through spectral monitoring of binary systems on timescales ≥ 10 yr, as it would be feasible for example in the case of a MBHB with $M_2 = 10^8 {\rm M}_\odot$ at $P \sim 32$ yr when $t_{\rm GW} \sim 7.5 \times 10^7$ yr.

Can these features possibly disentangle genuine binary candidates from the case of a recoiling MBH? The signature of a periodicity in the BELs is not expected in the case of a recoiling MBH. The MBH ejected from the nucleus of the host galaxy after binary coalescence would carry away a disk with an outer radius of the order of $R_{\rm out} \sim GM_{\rm BH}/v_{\rm kick}^2$, where $M_{\rm BH}$ and $v_{\rm kick}$ are the mass and the velocity of the recoiling MBH, respectively. As discussed in Sec. 3.3.1, numerical simulations in general relativity show that the maximum predicted value for the kick velocity is $\lesssim 5000\,{\rm km\,s^{-1}}$ (e.g. Lousto & Zlochower 2011 and references therein). This would correspond to the minimum outer radius for the disk bound to the ejected MBH, $R_{\rm out}^{\rm min}$, that we can compare with the BLR radius, $R_{\rm BLR}$, for an isolated MBH given by eq. 4.1. From Fig. 4.6 we derive that $R_{\rm BLR}$ has to be reduced by a factor > 0.5 in order to have a significant decrease of $F_{\rm MgII}/F_{\rm CIV}$. We find $R_{\rm out}^{\rm min}/R_{\rm BLR} > 0.5$ for $f_{\rm Edd} \lesssim 0.1$ and the mass of the remnant MBH in the range $M_{\rm BH} \sim 10^8 - 10^9$ ${\rm M}_\odot$. In this case we expect that the line ratios between the low and the high ionization lines do not differ from what observed in the case of a standard AGN.

4.4 MBHB candidates at z $\sim$ 2

In this Section we describe the possible use of the results reported in Sec. 4.2.1 and 4.3.3 as tool to select new secure spectroscopic MBHB candidates taking advantage of the huge quantity of data collected by recent surveys. In particular we present our search for new binary candidates at redshift $z \sim 2$ in the public archives of the SDSS selecting quasar spectra with unusually reduced values of $F_{\rm MgII}/F_{\rm CIV}$.

As considered before, at redshifts $z \gtrsim 0.8$ it is difficult to find evidences of velocity offsets between BELs and NELs since the wavelength of the most common NELs is longer than $\sim$ 3000 Å (e.g. Osterbrock & Ferland 2006). Therefore our results can be useful to look for MBHB candidates in a redshift range that has been not yet explored. The candidates selected because of a peculiar $F_{\rm MgII}/F_{\rm CIV}$ can be observed in different wavelength ranges in order to detect large velocity offsets between the broad and narrow emission line systems and/or variability in the luminosity, both modulated at the binary period (on timescales $\geq$ 10 yr). The detection of at least one of these two features, together with the reduced line ratio, provides an unambiguous signature of a sub-parsec MBHB (see Sec. 4.3.3).

Fig. 4.7 represents the normalized distribution of the ratio $F_{\rm MgII}/F_{\rm CIV}$ for 5850 quasars at $1.9 \leq z \leq 2.1$ from the SDSS DR6 catalog. The median value of the distribution at ~ 0.3 is marked by the solid vertical line. To test the findings of our study, we obtained observing time at the ESO Very Large Telescope in order to analyze the spectroscopic optical (rest-frame) features of MBHB candidates selected among those objects which in Fig. 4.7 show flux ratio values reduced by a factor $\gtrsim 2$ than what typically observed. In particular, we selected 9 objects visible from the Paranal site and characterized by $F_{\rm MgII}/F_{\rm CIV} \leq 0.1$ and $F_{\rm CIV} > 8 \times 10^{-15}\,{\rm ergs^{-1}cm^{-2}}$ in order to avoid contaminations from faint sources and to achieve an average signal-to-noise ratio $S/N \gtrsim 5$.

Observations were carried out with the ISAAC spectrograph adopting the SWS1-SH grism in LR mode which allows a spectral coverage in the range 14000 − 18200 Å and a resolution of $\lambda/\Delta\lambda \approx 500$ with 1 arcsec slit. The aim of our analysis is to measure (i) the shifts between the broad lines of CIV, MgII and Hβ relative to the narrow [OIII]$_{\lambda 5007}$ line, taken as the host galaxy rest frame, and (ii) the values of $F_{\rm MgII}/F_{\rm CIV}$ and $F_{{\rm H}\beta}/F_{\rm [OIII]}$ in order to verify that both the low ionization broad lines of MgII and Hβ have reduced fluxes relative to what observed in typical AGN spectra. We

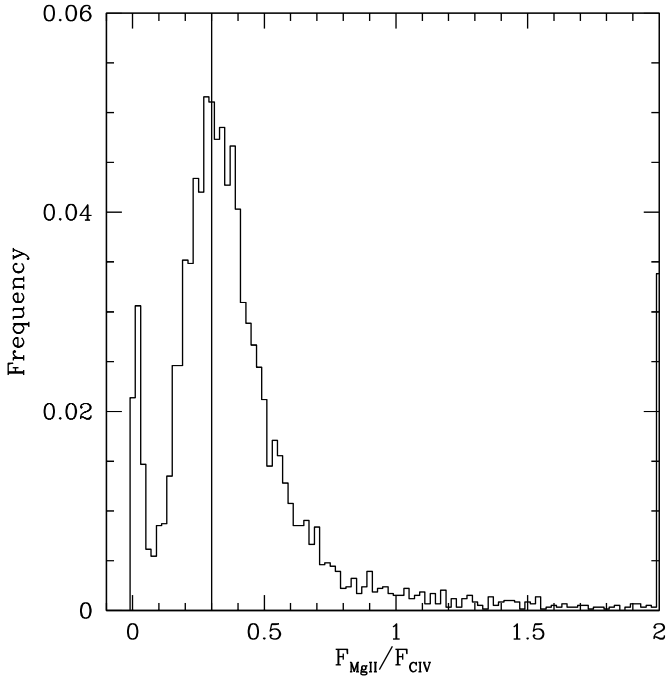

Figure 4.7: Normalized distribution of $F_{\rm MgII}/F_{\rm CIV}$ measured from the SDSS spectra of 5850 quasars at redshift $1.9 \leq z \leq 2.1$. The vertical solid line marks the median value of the flux ratio distribution at ~ 0.3. According to the results presented in this Chapter, we can look for sub-pc MBHB candidates among the sources with flux ratios reduced of a factor $\gtrsim 2$ than the distribution median value.

perform Gaussian fits on our collected NIR spectra and on the optical ones taken from the SDSS database to obtain the peak wavelength position of the considered emission lines. The line fluxes are computed summing the area subtended by the observed line profile in an appropriate wavelength range after having subtracted the continuum emission. We verified that the results of this procedure have lower uncertainties than the flux measures obtained through the Gaussian fits since the fainter MgII and Hβ lines are severely affected by the spectral noise leading to unreliable fitting results, and the profile of the CIV line is not always symmetric.

We are able to detect the Hβ and the $[\rm OIII]_{\lambda 5007}$ lines in the NIR spectra of 8 over 9 targets. The results of our spectral analysis are displayed in Fig. 4.8 and reported in Table 4.1. The errors on the BELs shifts come

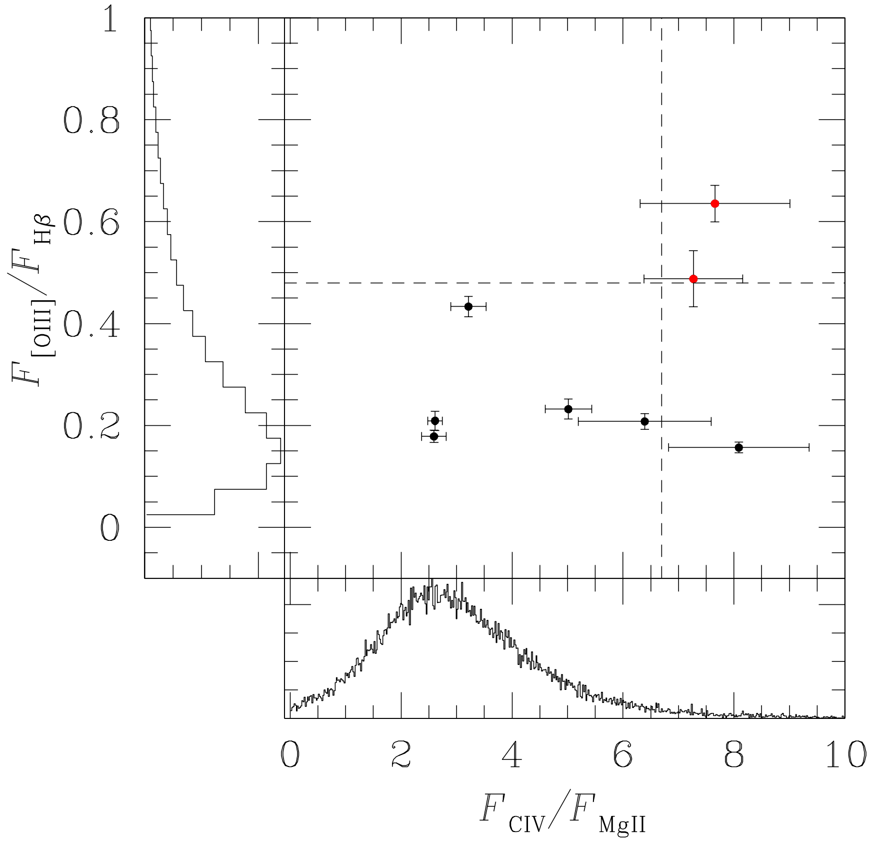

Figure 4.8: Values of $F_{\mathrm{CIV}}/F_{\mathrm{MgII}}$ and $F_{[\mathrm{OIII}]}/F_{\mathrm{H}\beta}$ obtained from our analysis of the optical and NIR spectra of 8 AGN selected at $z \sim 2$. According to our model, the two sources highlighted in red in the upper right corner, i.e. located on the right and above the vertical and horizontal dashed lines respectively, are classified as MBHB candidates (see text for details).The normalized distributions of $F_{\mathrm{CIV}}/F_{\mathrm{MgII}}$ and of $F_{[\mathrm{OIII}]}/F_{\mathrm{H}\beta}$ from the catalog of Shen et al. (2011) are shown on the side of the relative axis.

from the uncertainties on the peak wavelength position that are computed from the distribution of peak wavelengths resulting from the Gaussian fits with $\chi^2 < \chi^2_{\mathrm{bestfit}} + 1$, where $\chi^2_{\mathrm{bestfit}}$ is the Chi-square value corresponding to the best fit model. The errors on the flux ratios are given by summing the uncertainties on the flux measures in the wavelength range assumed for each broad line. The error on each flux measure is obtained interpolating the standard deviation of the flux distribution in wavelength bins with a width of 50 Å.

Fig. 4.8 shows the values of $F_{\rm CIV}/F_{\rm MgII}$ and $F_{\rm [OIII]}/F_{{\rm H}\beta}$ as measured for our targets together with the normalized distribution of the two flux ratios on the side of the relative axis as obtained from the catalog of Shen et al. (2011). Considering the median values of the two observed flux ratio distributions, MBHB candidates are expected to show $F_{\rm CIV}/F_{\rm MgII} \gtrsim 6.7$ and $F_{\rm [OIII]}/F_{{\rm H}\beta} \gtrsim 0.48$ assuming that $F_{\rm MgII}/F_{{\rm H}\beta}$ is constant for most binary orbital separations (see Sec. 4.2). Our targets should therefore be located in the upper right corner of Fig. 4.8, respectively on the right and above the vertical and horizontal dashed lines.

Besides the peculiar flux ratios, MBHB candidates are expected to show Doppler-shifts between the broad lines and the narrow [OIII] line. We take into account that the NIR data were collected ~ 3 yr (rest frame) after the optical observations so that in this time interval the hypothesized orbiting active MBH could have changed the direction of its motion along the line of sight. Hence we expect the three BELs to be Doppler-shifted all in the same direction or else the Hβ line to be shifted in the opposite direction with respect to the the MgII and the CIV lines.

From Fig. 4.8 and Table 4.1 it can be seen that 2 objects can be classified as MBHB candidates relying on the above criterions since they show reduced flux values for both the Hβ and the MgII line and their BELs are shifted accordingly with the binary model. However the absolute values of the shifts, in the range of $200 - 1500$ km s^{-1}, are not very high and need to be confirmed. Indeed we have planned new optical observations for these two peculiar sources to verify and monitor the shifts measured for the MgII and the CIV lines and to check that $F_{\rm MgII}/F_{\rm CIV}$ is still reduced. If confirmed as good MBHB candidates, these observations would represent a first positive test for our proposed spectroscopic technique since 2 over 4 targets with reduced values for $F_{\rm MgII}/F_{\rm CIV}$ would also show a reduced $F_{{\rm H}\beta}/F_{\rm [OIII]}$ and display the expected shift between the broad and the narrow lines. Concerning this point we have to consider that according to our analysis, 4 over 8 targets do not show a significantly reduced $F_{\rm MgII}/F_{\rm CIV}$ as expected from the starting selection based on the SDSS data. Comparing the $F_{\rm MgII}/F_{\rm CIV}$ distribution obtained from the SDSS database and shown in Fig. 4.7 with that computed for the same sources using the data by Shen et al. (2011) we verified that the median values are similar but the secondary peak observed at lower flux ratios in the SDSS data is not present in the distribution from Shen et al. (2011). We conclude that the automatic analysis procedure implemented in the SDSS tends to fail when applied to AGN spectra showing the peculiar features predicted in our MBHB model. These considerations will be taken carefully into account to carry out the NIR observational program to select more MBHB candidates at $z \sim 2$.

Object	z[a]	$F_{\rm CIV}/F_{\rm MgII}$	$F_{\rm [OIII]}/F_{\rm H\beta}$	Hβ shift[b] (km s^{-1})	MgII shift[b] (km s^{-1})	CIV shift[b] (km s^{-1})
J0917+3241	2.0211±0.0001	7.3±0.9	0.49±0.05	-176±258	-459±135	-1439±60
J1422+0120	2.0957±0.0003	7.7±1.3	0.63±0.03	275±155	-1224±355	-334±157
J1052+2810	2.0731±0.0004	2.6±0.2	0.18±0.01	335±252	241±165	-200±138
J0328-0536	2.0290±0.0005	8.1±1.3	0.16±0.01	70±244	1093±235	32±174
J1039+0531	2.0380±0.0005	3.2±0.3	0.43±0.02	512±575	-113±154	-482±179
J1254-0043	2.0517±0.0005	6.4±1.2	0.21±0.01	638±357	543±177	-947±152
J0928-0023	2.0776±0.0008	2.6±0.1	0.21±0.02	375±597	219±263	516±248
J1344-0052	2.0842±0.0002	5±0.4	0.23±0.02	-641±178	608±590	255±151

[a] measured from the peak wavelength position of the narrow [OIII]λ5007 emission line
[b] measured from Gaussian fits to the peak position of the relative broad line

Table 4.1: Spectroscopic UV/optical rest-frame emission line properties of 8 targets selected from the SDSS at $z \sim 2$. The two objects highlighted in boldface can be classified as sub-pc MBHB candidates according to our criterion based on peculiar flux ratios (see text for details).

Chapter 5

Summary and conclusions

The focus of this thesis was the study of electromagnetic signatures from close MBHBs evolving in gas-rich environments. In particular, we investigated the possibility of detecting the presence of sub-pc MBHBs in Active Galactic Nuclei (AGN) by searching for peculiar emission line properties in their spectra. The theoretical framework is that of two MBHs orbiting in a Keplerian binary on pc scales that formed in the aftermath of a gas-rich galactic merger. The binary is embedded within a rotating circum-binary disk that is guiding both the dynamical hardening and the fueling of the MBHs under the action of gravitational torques and inflowing tidal streams.

The physical scenario outlined above is in general agreement with the current cosmological model and with the observational evidences of MBHs residing at the center of isolated as well as interacting massive galaxies. Still MBHBs on pc/sub-pc scales are difficult to observe and the expected number of sources detectable with gravitational or electromagnetic waves is uncertain (e.g. Dotti et al. 2012 for a recent review). For now it is not possible to spatially resolve these systems unless through radio interferometric observations of specific nearby sources, as for the only known case of a binary system with a projected separation of $\sim$ 7pc in the nucleus of the radio galaxy 0402+379 (Rodriguez et al. 2006). Hence much attention has been given to find evidences of the binary orbital motion through variability studies, looking for periodic light curves, and spectroscopic searches performed on increasingly large samples, relying on the presence of multiple sets of broad (BELs) and narrow (NELs) emission lines at slightly different redshifts.

In the last decade, several analytical and numerical techniques have been developed to better understand the evolution of comparable mass binaries embedded in circum-binary disks. These studies highlighted the importance of considering in details the dynamical disk-binary coupling to firmly assess the MBHB fate (e.g. Rödig et al. 2012 and references therein). However we have not yet reached the point where we can benefit from the comparison between the observed and expected number of spectroscopically selected sub-pc MBHBs because of the lack of confirmed MBHB candidates as well as the uncertainties in the theoretical description of the MBHB evolution. For instance, according to the models of Volonteri et al. (2009), different assumptions on the level of activity associated with the binary MBHs, depending on the evolutionary history of their host systems, yield results that differ of an order of magnitude. Thus the upper limit to the predicted number of detectable sub-pc MBHBs in the SDSS unobscured quasar spectra at $z \lesssim 0.7$ is between 0 and ~ 200.

In this context, the thesis project has been developed along two main directions involving:

(i) *The search for new binary candidates at different redshifts*, ruling out other possible interpretations of their physical nature. The discovery of secure MBHBs would be a fundamental test for current models of galaxy formation and for the different scenarios of MBHB orbital evolution. Proving the existence of sub-pc MBHBs is of extreme importance for Gravitational Wave (GW) experiments, such as the proposed NGO and the on-going Pulsar Timing Array, in order to constrain the expected number of detectable sources. Moreover, a better knowledge of the environment of close MBHBs would help to predict the possible electromagnetic counterparts to GW detections.

(ii) *The prediction of new observational features* associated with MBHBs at different evolutionary stages. The identification of peculiar observational features associated with MBHBs benefits from a detailed understanding of broad line region (BLRs) associated with single MBHs. At the same time, the study of BLR properties in strongly perturbed scenarios (as in the presence of a MBHB) can unveil new clues on the structure of unperturbed BLRs and on the complexity of the AGN physics.

The main results of our contributions to these research areas will be presented in the following paragraphs together with some possible future developments.

In the first part of this work we have discussed a MBHB model to interpret the optical spectrum of the quasar SDSSJ0927. Apart from the presence of a set of blue-shifted BELs attributed to the gas bound to the orbiting active

MBH, this source displays a very peculiar set of blue-shifted NELs. These have been interpreted in terms of the emission from the low density gas in the gap region of the circum-binary disk. If our model will be confirmed for this source or for other possible candidates showing similar features, it would represent the first detection ever of an electromagnetic signature associated with the material in the circum-binary gap whose detailed properties are still largely unknown. For the case of SDSSJ0927, we have shown that the alternative scenario of a recoiling MBH is much less probable than the binary hypothesis and cannot consistently explain the set of blue-shifted NELs. Moreover the images of the field around this source analyzed by our group do not reveal the presence of a rich cluster of galaxies that would increase the possibilities of a chance superposition of two distinct objects along the line of sight.

In the second part of this work we have proposed a new spectroscopic technique based on the observation of a peculiarly reduced value of the flux ratio between two prominent BELs characterized by different ionization potentials, i.e. the CIV and the MgII lines ($F_{\rm MgII}/F_{\rm CIV}$). We have focused on unequal mass MBHBs with the secondary being the only active MBH and we have taken into account the different contributions to the BELs coming from the BLR bound to the single active MBH, the circum-binary disk and the low density gas in the gap. Our analysis shows that it is possible to select close MBHBs because of a peculiarly reduced value of $F_{\rm MgII}/F_{\rm CIV}$ for a limited range of sub-pc orbital separations. In this range the main contribution to the BELs comes from the tidally perturbed BLR bound to the secondary active MBH. We noticed that, although orbiting at very close separations, the MBHBs characterized by a low $F_{\rm MgII}/F_{\rm CIV}$ are expected to be in the long-lived disk-driven phase of the binary orbital migration. At even closer separations, where the binary lifetimes are shorter due to the emission of gravitational waves, the line flux from the BLR of the secondary keeps on reducing, while the gas associated with the circum-binary disk starts to give a significant contribution to the BELs. This has two main consequences: $F_{\rm MgII}/F_{\rm CIV}$ rises up into the typical observed range for AGN, and the BELs are expected to show a more complex profile and temporal behavior that is not easily referable to the binary orbit, in agreement with the results of Shen & Loeb (2010) for a different BLR geometry.

An important advantage of our newly proposed spectroscopic approach relies in the possibility of selecting new MBHBs at higher redshifts since it does not require the presence of a set of NELs, such as the [OIII]λ5007, observable in the optical range up to $z \lesssim 0.8$. We have shown that it is possible to define a sample of peculiar quasars at $1.9 \lesssim z \lesssim 2.1$ characterized by $F_{\rm MgII}/F_{\rm CIV} \lesssim 0.15$ according to the data available in the SDSS archives. These targets can be further observed in the NIR band to look for a shift between the broad Hβ and the narrow [OIII]. Observing an anomalously reduced $F_{\rm MgII}/F_{\rm CIV}$ together with a periodically varying Doppler-shift between the broad and the narrow emission lines would be indeed a clear indication of the presence of a sub-pc MBHB since this feature is not predicted by any other scenario alternative to the binary interpretation. Hence we selected 9 sources with peculiarly reduced flux ratios from the SDSS database and we observed them again with the ISAAC NIR spectrograph mounted on the Very Large Telescope. Our main results are that 3 over 8 detected targets actually show a reduced $F_{\rm MgII}/F_{\rm CIV}$, 2 of which display a shift of a few hundred up to ~ 1000 km s^{-1} between the narrow [OIII] and the broad CIV, MgII and Hβ.

In the near future, we plan to expand both the observational and the theoretical work presented in this thesis. The new *observational* work will comprise:

(i) Follow-up observations of SDSSJ0927 to monitor the expected periodic motion of the shifted emission lines, and to gather additional information on the quasar emission properties at different wavelengths, the quasar host galaxy and its close environment. These observations are mandatory to firmly verify the MBHB model proposed for this source, and to exclude the other possible physical scenarios. These follow-up studies will be performed also on the other 31 MBHBs candidates selected at $z \lesssim 0.8$ in the SDSS database through an automatic procedure developed by our group upon the serendipitous discoveries of a few peculiar sources such as SDSSJ0927.

(ii) A further implementation of the search method developed by our group to look for MBHB candidates with double-peaked CIV profiles in the higher redshift range of $1.6 < z < 4.5$. Two distinct peaks in the CIV line are not observed in the spectra of double-peaked emitters (see Sec. 2.2.2) and they are not expected in the case of a recoiling MBH. Therefore double-peaked CIV profiles could be a distinguishing signature of the presence of two active MBHs member of a close MBHB.

(iii) Follow-up observations of the two MBHB candidates selected at $z \sim 2$ to confirm the peculiarly reduced value of $F_{\rm MgII}/F_{\rm CIV}$ and to monitor the shifts of the broad optical lines. We have verified that the spectroscopic measures of the SDSS automatic procedure are not reliable in the case of peculiar spectra such those expected for the targets selected through our flux ratios criterion. Therefore it will be necessary to define a new starting sample to carry out the search for MBHBs at $z \sim 2$, and to firmly assess the validity of our spectroscopic technique.

The new *theoretical* work will comprise:

(i) The improvement of the simplified radiation transport scheme adopted in our analysis of data taken from hydrodynamical numerical simulations to properly model the attenuation of the ionizing radiation and to include the possible effects related to the line optical depth along the ray-paths.

(ii) The realization and the analysis of grid-based hydrodynamical simulations to better map the properties of the lower density gap region and so to study its possible contribution to the emission of forbidden lines as expected in the MBHB model for SDSSJ0927.

(iii) The prediction of other possible observational features associated with close MBHBs that can be detected for example through reverberation mapping studies. The presence of a sub-pc binary can affect the spatial distribution, the dynamical properties and the ionization structure of the BLR implying peculiar characteristics in the lines profiles and in the time delays for lines of different ionizing potentials.

Appendix I: Numerical simulations of MBH binaries/circum-binary disks systems

In Ch. 4 of this thesis we presented our analysis performed on data taken from a numerical simulation of a MBHB orbiting in the lower density region, i.e. the gap, excavated in the central part of a surrounding thin circum-binary gaseous disk. The considered numerical experiment is presented in the work by Sesana et al. (2012; S12 hereafter) and was performed using the code Gadget-2. In the following paragraphs we we will first describe the basic features of the public version of the code. Then we will highlight the main differences present in the modified version used by S12.

Gadget-2: public version

The code Gadget-2 (GAlaxies with Dark matter and Gas intEracT; Springel, Yoshida & White 2001, Springel 2005 and references therein) is a Smoothed Particle Hydrodynamics (SPH; Gingold & Monaghan 1977, Lucy 1977) tree-code (Appel 1985, Barnes and Hut 1986; BH96 hereafter) where the gas dynamics is followed with SPH and the gravitational forces are computed with a hierarchical multipole expansion. Gas and collisionless fluids (e.g. dark matter and stars) are both represented as particles. The code is particularly suited for the study of three-dimensional problems implying a large dynamic range in the evaluation of both the gravitational and the hydrodynamic forces. Thanks to its particle-based Lagrangian nature Gadget-2 is indeed adaptable to any given geometry and allows an automatic change of resolution in the hydrodynamic calculations that follows the local gas density. Hereafter we will describe the algorithm used to compute the gravitational and the hydrodynamical forces.

Gravitational forces

Gadget-2 evaluates the gravitational forces using a so called tree method. In this scheme, the particles are arranged in a hierarchy of groups. When the acceleration of a particular particle is computed, the force exerted by distant groups is approximated by the lower moments of its multipole expansion. In this way, the force on a single particle can be computed with $\mathcal{O}(N \log N)$ interactions instead of $\mathcal{O}(N^2)$ as required by direct summation methods. The forces become more accurate if the multipole expansion is carried out to higher orders, but eventually the increasing cost of evaluating higher moments makes it more efficient to terminate the multipole expansion and rather use a larger number of smaller particles sub-groups to achieve a desired force accuracy. In Gadget-2 only the monopole moments are considered.

The procedure for the evaluation of the gravitational acceleration of each particle is performed in two steps as described hereafter.
(i) Following the BH96 oct-tree construction, the computational domain is hierarchically partitioned into a sequence of cubes, where each cube contains eight sub-cubes, each with half the side-length of the parent. These cubes form the nodes of the tree structure. The tree is constructed such that each node (cube) contains either exactly one particle (leaf of the tree), or is progenitor to further nodes. In this case the node carries the monopole moment (i.e. the total mass and the position of its center of mass) of the gravitational potential generated by all the particles that lie inside its cube.
(ii) The force computation proceeds by walking the tree structure, i.e. summing up the appropriate force contributions from the tree nodes. The tree walk along a certain branch is terminated when it is possible to use the multiple approximation for the considered node. If this is not the case, the node is *opened* and the walk is continued with all its sub-cubes. In the standard BH96 tree walk, the multipole expansion of a node of size l can be used if:

$$r > \frac{l}{\theta} \tag{5.1}$$

where θ is the accuracy parameter and r is the distance between the considered particle and the center of mass of the node. This geometrical criterion tries to limit the relative error of every particle-node interaction and results from the comparison between a size estimate of the quadrupole term ($\sim Ml^2/r^4$) and that of the monopole term ($\sim M/r^2$). In Gadget-2 this criterion is used for the first force computation in the simulation. Then a second criterion is used requiring that the absolute force error is a small fraction α of the total expected force exerted on each particle. This force is assumed to be well approximated by the force evaluated at the previous time-step explaining why this criterion cannot be used at the first time-step. Considering that in Gadget-2 the multipole expansion is truncated at monopole order, the new criterion can be expressed as:

$$\frac{GM}{r^2}\left(\frac{l}{r}\right)^2 < \alpha\,|\vec{a}_{\rm old}| \tag{5.2}$$

where $\vec{a}_{\rm old}$ is the particle acceleration as computed in the previous time-step. An additional condition that has to be fulfilled not to open a node is that the considered particle has to lie outside a box about 20 percent larger than the tree node.

The mass distribution in Gadget-2 is modelled via a finite number of particles, that is usually significantly smaller than the real number of either stars, gas particles or dark matter particles in a real physical system. In order to prevent artificially large gravitational accelerations due to close passages of extremely massive particles a *gravitational softening* prescription is implemented in Gadget-2. Each particle generates a gravitational potential:

$$\Phi(\vec{r}) = -G\,m\,W_2(r)/\epsilon, \tag{5.3}$$

where m is the particle mass, ϵ is its the gravitational softening length and $g(r)$ describe the radial dependence of the *softened* gravitational potential of each particle:

$$W_2(u) = \begin{cases} \frac{16}{3}u^2 - \frac{48}{5}u^4 + \frac{32}{5}u^5 - \frac{14}{5}, & 0 \leq u < \frac{1}{2}, \\ \frac{1}{15}u^{-1} + \frac{32}{3}u^2 - 16u^3 + \frac{48}{5}u^4 - \frac{32}{15}u^5 - \frac{16}{5} & \frac{1}{2} \leq u < 1, \\ -u^{-1} & u \geq 1 \end{cases} \tag{5.4}$$

where $u = r/\epsilon$. This is equivalent to the potential produced by a mass distribution given by:

$$\rho(r) = m_k W(r/\epsilon), \tag{5.5}$$

where W is the smoothing kernel expressed as a spline of the form:

$$W(u) = \frac{8}{\pi\epsilon^3} \begin{cases} 1 - 6u^2 + 6u^3, & 0 \le u \le \frac{1}{2}, \\ 2(1-u)^3, & \frac{1}{2} < u \le 1, \\ 0, & u > 1. \end{cases} \tag{5.6}$$

If the distance between two particles is $> \epsilon$, $g(r) = 1/r$ and the gravitational interaction follows exactly the Newtonian prescription.

Hydrodynamics

Gadget-2 evaluates the hydrodynamic forces and the variations of internal energy in two phases.
(i) In the first phase, the *hydrodynamical smoothing lengths* h_i are determined for the gaseous particles, and for each of them, the neighboring particles inside their respective smoothing radii are found. The Lagrangian nature of SPH arises when this number of neighbours is kept either exactly, or at least roughly, constant. This is achieved by varying the smoothing length h_i of each particle accordingly. The h_i thus adjust to the local particle density adaptively, leading to a constant mass resolution independent on the density of the flow. As suggested for the first time by Hernquist & Katz (1989), Gadget-2 uses the gravity tree discussed above for the neighbour search and the density evaluation. The search is performed in the cubic search range inscribing the spherical region of size h_i around each particle. Walking the gravitational tree, Gadget-2 opens a node if it spatially overlaps with the spherical search range otherwise it is discarded. If the algorithm arrives at a leaf of the tree, this is added to the neighbour list if the relative particle lies inside the search radius. A tree walk is terminated along a branch if the node lies completely inside the search range. Then all the particles in the node can be added to the neighbour list, without checking any of them for overlap with the search range any more to reduce the computational effort. The procedure starts with a guess on the search radius ($h_{i,\mathrm{guess}}$) for each particle. The prediction of this radius is based on the smoothing length $h_i^{(\mathrm{old})}$ evaluated at the previous time-step, on the number of neighbours N_i within $h_i^{(\mathrm{old})}$ at the current time-step, and the local velocity divergence:

$$h_{i,\mathrm{guess}} = \frac{1}{2} h_i^{(\mathrm{old})} \left[1 + \left(\frac{N_\mathrm{s}}{N_i} \right)^{1/3} \right] + \dot{h}_i^{(\mathrm{old})}\, \Delta t, \tag{5.7}$$

where $\dot{h}_i = \frac{1}{3} h_i (\nabla \cdot \vec{v})_i$, and N_s is the desired number of neighbours. The term in brackets tries to bring the number of neighbours back to the desired value if N_i deviates from it. In the first time-step no previous $h_i^{(\mathrm{old})}$ is known, so Gadget-2 follows the neighbour tree backwards from the leaf of the particle under consideration, until a first reasonable guess for the local particle density is obtained (based on the number N of particles in a node of volume l^3), providing an initial guess for $h_{i,\mathrm{guess}}$. If the obtained number of neighbours inside the predicted $h_{i,\mathrm{guess}}$ is not equal to the required number of neighbours (or fall outside the prescribed range), Gadget-2 iteratively adjusts $h_{i,\mathrm{guess}}$ until the number of neighbours is again brought back to the desired range.
(ii) The second phase consists in the computation of the hydrodynamical properties of the gas (e.g. the density ρ_i, the internal energy per unit of mass u_i, the pressure P_i), and in the computation of the hydrodynamic forces. The density is computed as:

$$\rho_i = \sum_{j=1}^{N} m_j W(r_{ij}/h_i) \tag{5.8}$$

where $r_{ij} \equiv |\vec{r}_i - \vec{r}_j|$ is the distance between the particles i and j, and $W(\vec{r}_{ij}/h_i)$ has the same form of the gravitational smoothing kernel shown in eq. 5.6. The code assumes that the gas is ideal, and that is described by an *entropic function* A defined as

$$A = P/\rho^\gamma, \tag{5.9}$$

where P is the gas pressure and γ is the gas polytropic index ($\gamma = 5/3$ for an ideal monoatomic gas). Since A is only a function of the entropy for an ideal gas, it is referred to as the gas *entropy* in the Gadget-2 paper and in the rest of this Appendix. We notice that the entropy of each particle i (A_i) is automatically conserved in absence of shocks or external heating sources.

The hydro force due to the pressure gradient (felt only by gas particles) is:

$$\vec{a}_i^{\mathrm{gas}} = -\sum_j m_j \left(f_i \frac{P_i}{\rho_i^2} \nabla_i W_{ij}(h_i) + f_j \frac{P_j}{\rho_j^2} \nabla_i W_{ij}(h_j) \right), \tag{5.10}$$

where

$$f_i = \left(1 + \frac{h_i}{3\rho_i} \frac{\partial \rho_i}{\partial h_i} \right)^{-1} \tag{5.11}$$

and P_i is computed from the particle entropy ($P_i = A_i \rho_i^{\gamma}$). In presence of shocks in the gas an additional force term is added:

$$\vec{a}_i^{\rm gas} = -\sum_j m_j \Pi_{ij} \nabla_i \bar{W}_{ij}, \tag{5.12}$$

where $\bar{W}_{ij}$ is the arithmetic average of the two kernels $W_{ij}(h_i)$ and $W_{ij}(h_j)$, and

$$\Pi_{ij} = -\frac{\alpha}{2}(c_i + c_j - 3w_{ij}) w_{ij} \rho_{ij}. \tag{5.13}$$

Here α is a dimensionless parameter (usually set in the range $\approx 0.5-1$) setting the strength of the gas numerical viscosity, c is the sound speed associated to a particle, and $w_{ij} = v_{ij} \dot{r}_{ij}/|r_{ij}|$ if the two i and j particles are approaching each other, or 0 otherwise. In case of such an irreversible shock, entropy is generated by the artificial viscosity at a rate

$$\frac{\mathrm{d}A_i}{\mathrm{d}t} = \frac{1}{2}\frac{\gamma-1}{\rho_i^{\gamma-1}} \sum_j m_j \Pi_{ij} v_{ij} \dot{\nabla}_i \bar{W}_{ij}. \tag{5.14}$$

MBH binary simulation

S12 used the code Gadget-2 to model a MBHB that has excavated a gap in a co-rotating, co-planar thin Keplerian disk. The properties of the circum-binary disk are expected to depend on the binary mass (M) and semi-major axis (a). S12 focused on the prediction of electromagnetic signatures associated with MBHBs whose gravitational wave (GW) emission is in the frequency range of the Pulsar Timing Array experiment. Accordingly, S12 set the primary mass $M_1 = 2.6 \times 10^8$ M$_\odot$, the binary mass ratio $q = 0.35$ and the initial semi-major axis $a_0 = 0.012$ pc.

The dynamics of the system is studied in the Newtonian approximation neglecting relativistic corrections that are still not important at the considered orbital separation. The disk is modelled with 8 million gaseous particles and its mass is set $M_{\rm d} \sim 1.5 \times 10^2\, M$ assuming a β-disc model extending from $R_{\rm in} = 2a_o$ to $R_{\rm out} = 10a_o$. The disk viscous timescale results to be shorter than the GW coalescence timescale so that the MBHB is still gravitationally coupled with the circum-binary disk. Hereafter we list the changes applied by S12 to the public version of the code.

(i) In order to follow the MBHB dynamics with a better accuracy, the two

MBHs are taken out of the standard oct-tree implemented in the code and used to model the gravitational interactions between the disk particles. The gravitational forces acting on the MBHs are computed exactly, i.e. by summing up the contribution from each gaseous particle. To maintain symmetry, the gravitational force exerted by the MBHs is added directly to each particle. Moreover, to ensure an accurate integration, the dynamics of the MBHs is followed with a fixed time-step, equal to $0.01\Omega_o^{-1}$ where $\Omega_o = \sqrt{GM/a_0^3}$.
(ii) In addition to the basic hydrodynamic equations, the gas is allowed to cool according to $(du/dt)_{\rm cool} = u/t_{\rm cool}$ where u is the gas internal energy per unit mass and $t_{\rm cool}$ is the cooling time. This is set to be proportional to the local disk dynamical time $t_{\rm cool} = \beta\, t_{\rm dyn}$ where $\beta = 10$ so that the cooling timescale is not fast enough to make the disk fragment. Moreover in order to confine the gas in the central gap to a thin geometry, the internal energy (per unit mass) of the small amount of gas present in the inner regions ($r \lesssim 1.75\, a$) is forced to follow the relation $u \sim 0.14\,(GM/R)$.
(iii) The particles reaching a short distance (sink radius) from either MBH are removed from the simulation. Hence the MBH accretion rate is defined as the number of particles passing below its sink radius in a given time-step. The mass and momentum of the accreted particles are added to the respective MBH. The sink radius for the two MBHs is set to $\sim 0.005 a_0$. This value is greater than the typical particle softening lengths so that the two MBHs can be safely modeled as non-softened particles.

Appendix II: CLOUDY

In Ch. 4 of this thesis we used the released version 08.00 of the code CLOUDY (Ferland et al. 1998) to compute the physical conditions and the resulting spectral properties of an ensemble of gaseous clouds in the broad line region (BLR) of an active galactic nucleus (AGN). BLR clouds are located close to the very energetic radiation field, extending from the radio band to the γ-rays, emitted by the accreting MBH and are characterized by high hydrogen number densities $n_{\rm H} \gtrsim 10^{10}\,{\rm cm}^{-3}$. Differently from the case of a planetary nebula ionized by a hot star, the X-ray non-thermal part of the AGN continuum penetrates trough the cloud front creating a warm partially ionized zone extending beyond the hydrogen ionization front. Moreover the higher cloud densities imply that line optical-depth and radiative transfer effects can be very important. Hence the BLR physics is far more complicated and the application of the standard methods of nebular astrophysics give less certain results (see e.g. Osterbrock & Ferland 2006).

Numerical simulations like those performed by CLOUDY make possible to self-consistently model complex physical environments, such that of a BLR, whose properties are determined by a host of microphysical processes, and to predict many observable quantities specifying only the properties of the cloud and of the radiation field striking it. In the following paragraphs we will overview the code assumptions and the approach used in the computations. Then we will give a schematic view of the code structure and describe the input/output options making particular reference to those considered in this work.

Overview

CLOUDY is a one-dimensional code designed to compute the distribution of ionization, density and temperature across a cloud possibly exposed to an external source of radiation, and to predict the resulting spectrum. This is done by solving the equations of statistical and thermal equilibrium, the equations that balance ionization-neutralization processes, and the heating-cooling processes. The density of a particular ionization level i is given by a balance equation of the form:

$$\frac{\partial n_i}{\partial t} = G_i + \sum_{j \neq i} R_{ji} n_j - n_i \left(L_i + \sum_{j \neq i} R_{ij} \right) = 0 \tag{5.15}$$

where n_i is the level i population, G_i and L_i represents the rate per unit volume at which new atoms appear and are lost at the level i respectively while R_{ji} and R_{ij} are the rates of processes that move atoms up and down the ionization levels. Eq. 5.15 together with equations representing conservation of energy, mass and charge fully specify the problem.

CLOUDY makes no assumptions that the gas is in local thermodynamical equilibrium (LTE), i.e. that the distribution of the levels populations is given by:

$$\frac{n_u}{n_l} = \frac{g_u}{g_l} exp \left(\frac{\Delta E}{kT} \right) \tag{5.16}$$

where g_u and g_u are respectively the statical weights of the upper u and lower l level, ΔE is energy difference between the upper and the lower level, k is the Boltzmann constant and T is the gas equilibrium temperature. However in most cases, as the one considered in this work, it assumes that the cloud is old enough that atomic processes have had time to become time-steady. At the end of the calculations the code will check that none of the equilibrium timescales for significant physical processes were longer than the age of the cloud. Generally, for an ionized gas with electronic temperatures $\approx 10^4$ K, the longest is the hydrogen recombination time scale

$$T_{\rm rec} = \frac{1}{\alpha(T_e) n_e} = 0.66\, T_4^{0.8} n_9^{-1} \text{ hours} \tag{5.17}$$

where T_4 is the temperature in units of 10^4 K, n_9 is the electron density in units of $10^9\,\mathrm{cm}^{-3}$ and α is the total recombination coefficient, i.e. the sum of the recombination coefficients to all the hydrogen levels.

The cloud is also assumed to be static although a wind model can be optionally computed. In the stationary case the lines are broadened only by thermal motions and an additional micro-turbulent component, i.e. occuring over scales smaller than a photon mean free path, can be included. The cloud orbital motion on larger scales is considered macro-turbulence, i.e. it does not affect the optical depth through the cloud emitting region.

The code will not permit temperatures below 2.8 K or above 10^{10} K. CLOUDY assumes that the electrons are non-relativistic while there is no formal lower temperature limit although very cold gas is rarely in steady-state due to the much longer equilibrium timescales. Hence the range of validity of the code is approximately from 10 K to 10^9 K and temperatures outside this range within the code limits are treated with greater uncertainty.

The code includes all the ionization stages of the 30 lightest elements from H to Zn and the grain physics can be added as an option. The numerical limits to the density are set by the architecture of the machine that is performing the simulation. The physics of the code imposes no lower density limit. For high densities the simulation is less complete mainly because of the treatment of the line radiative transfer and of the ionization processes involving high-excited states of heavy elements (see below) that set an upper limit at $\sim 10^{15}\,\mathrm{cm}^{-3}$. Tests with densities of $10^{19}\,\mathrm{cm}^{-3}$ show that hydrogen and helium atoms go to LTE at high densities.

In general, the observed spectrum is the result of the transport of radiation through the depth-dependent physical conditions. The approach of most 1-D spectral synthesis code such as CLOUDY is to consider a cloud divided into a large number of zones, chosen so that conditions are fairly constant across each. Going through the different zones, all the ionization and the recombination processes determining the balance of eq. 5.15 are considered.

Ionization precesses include: *photoionizations and collisional ionizations*, new electrons are liberated through the absorption of photons with energy greater than the hydrogen ionization potential and through collisions between electrons and ions, respectively; *the Auger effect*, high energy photons can remove an inner-shell electron of an heavy atom and the electron vacancy can be filled by ejecting outer electrons; *the charge exchange process*, two-body reactions between neutral atoms and protons can convert the protons into hydrogen atoms and the original neutral atoms into ions.

Recombination processes include: *radiative recombinations*, recaptures of free electrons to any level are followed by downward radiative transitions leading ultimately to the ground level; *dielectronic recombinations*, due to resonances in the total recombination cross section of heavy ions the incoming free electron can give up its kinetic energy exciting a bound level of the ion and thus creating a short-lived doubly excited bound level of the next lower stage of ionization that can further decay to a singly excited bound level and then down to the ground term; *three-body recombinations* and *charge transfer* corresponding respectively to the inverse process of collisional ionizations of levels with large principal quantum number n and of the charge exchange process between a proton and a neutral atom.

The free electrons are assumed to have a predominantly Maxwellian velocity distribution. The electrons energy is indeed redistributed by Coulomb scatterings between electrons that have the largest cross section among all the other physical processes involved and tend to set up a Maxwell-Boltzmann energy distribution. Thus the electronic kinetic temperature is the only thermodynamic quantity describing the ionized cloud and is determined by the balance between heating and cooling processes. For instance, the net photoelectric heating rate of level u is given by:

$$G = G_u - \Lambda_{\mathrm{ind},u} - \Lambda_{\mathrm{spon},u} \qquad \mathrm{erg\,s^{-1}\,cm^{-3}} \tag{5.18}$$

where the heating rate due to photoionization is:

$$G_u = n_u \int_{\nu_0}^{\infty} \frac{4\pi J_\nu}{h\nu} \alpha_\nu h(\nu - \nu_0)\, d\nu \tag{5.19}$$

the cooling rate due to induced recombination is:

$$\Lambda_{\mathrm{ind,u}} = n_u \int_{\nu_0}^{\infty} \frac{4\pi J_\nu}{h\nu} \alpha_\nu exp(-h\nu/kT) h(\nu - \nu_0)\, d\nu \tag{5.20}$$

the cooling rate due to spontaneous radiative recombination is:

$$\Lambda_{\mathrm{spon},u} = n_e n_{\mathrm{ion}} \frac{8\pi}{c^2} \frac{g_n}{g_e g_{\mathrm{ion}}} \left(\frac{2\pi m_e k}{h^2 T}\right)^{3/2} \int_{\nu_0}^{\infty} \nu^2 h(\nu - \nu_0) exp(-h/\nu - nu_0)/kT)\, d\nu \tag{5.21}$$

and

$$J_\nu = \frac{1}{4\pi} \int I_\nu(\theta, \phi)\, d\Omega \tag{5.22}$$

where J_ν is the mean angle-averaged intensity and I_ν is the monochromatic intensity in units of $\mathrm{erg\,cm^{-2}\,s^{-1}\,sr^{-1}\,Hz^{-1}}$, α_ν is photoionization rate, h is the Planck constant and ν_0 is the photoionization frequency threshold for level u. Instead collisional processes contribute to a net cooling rate due to the emission of collisionally excited lines given by:

$$\Lambda_{ul} = h\nu_{ul}(n_l C_{lu} - n_u C_{ul}) \tag{5.23}$$

and to a net heating rate due to collisional ionizations less three-body recombinations:

$$G_k - \Lambda_k = \sum_u n_u C_{uk} h\nu_0 (1 - b_u) \tag{5.24}$$

where C_{lu} is the collisional excitation rate from the lower to the upper level and C_{ul} is the collisional de-excitation rate, C_{uk} is the collisional ionization rate and b_u is the departure coefficient, i.e. the ratio between the actual level population and the value corresponding to the LTE case. Far from thermodynamic equilibrium, departure coefficients are usually $\gg 1$ only for the ground term resulting in a net cooling process.

Then the continuum and the line radiative transfer must be solved simultaneously. As far as the optical depth to electron scattering is not large, the transfer of the attenuated incident continuum and of the diffuse emission is properly treated considering the absorptions and re-emissions associated with all the involved processes (e.g. free-free (invers bremssthralung) absorption, grain opacity (when present), electron scattering (of both bound and free electrons) and Rayleigh scattering among the main opacity sources for the ionizing continuum; free-free (bremsstrahlung), free-bound and two-photon emission in addition to the continuum absorption and re-emission from all the ground terms and many excited states of all the ionization stages of the included elements). Generally, the treatment of radiative transfer (RT) effects is not critical for the continuum since the diffuse ionizing emission, mostly produced by recombining gas, is much fainter than the incident continuum. The default assumption for the diffuse ionizing radiation is to account for all the opacity sources that compete in absorbing the recombination photons making the recombination process more efficient using a modified version of the on-the-spot (OTS) approximation (i.e. that the recombinations to the ground state produce ionizing photons that are all absorbed locally).

On the other hand line transfer effects can be important especially for strong resonance lines (i.e. corresponding to the transition between the ground state and the first excited level) such as the hydrogen Lyα line. Line RT is performed with escape probabilities (EP). The radiative balance equation for a two-level atom is given by:

$$A_{ul} n_u - B_{lu} \overline{J} n_l + n_u B_{ul} \overline{J} = A_{ul} n_{ul} \rho_{ul} \tag{5.25}$$

where A_{ul}, B_{lu} and $B_{ul} = (g_l/g_u) B_{lu}$ are the Einstein coefficients for spontaneous emission, absorption and for stimulated emission respectively,

$\overline{J} = \int_0^\infty J_\nu \phi(\nu)\, d\nu$ is the mean intensity averaged over the line whose profile function is $\phi(\nu)$ and $\rho_{ul} = 1 - \overline{J}/S$ is the net radiative bracket where $S = A_{ul}/(B_{lu}(n_l - n_u g_l/g_u))$ is the line source function. The essence of the line RT implementation in the code is to approximate ρ_{ul} with the escape probability $P_{\rm esc}$ assuming that the difference between $\overline{J}$ and S is due to photons leaking away from the region.

The major advantage of EP relies in their computational simplicity. The only interaction between a specific cloud location and the global environment is that the EP at a depth τ into a cloud of total optical depth T is simply given by $[P_{\rm esc}(\tau) - P_{\rm esc}(T-\tau)]/2$. Moreover the line thermalization effects are simply included. If C_{ul} is the collisional de-excitation rate for a level with transition probability A_{ul}, then the line will undergo A_{ul}/C_{ul} scatterings before being collisionally de-excited. Neglecting collisional de-excitations, a line at an optical depth τ will undergo $P_{\rm esc}^{-1}$ scatterings before escaping. Photons produced at a τ such that $P_{\rm esc}^{-1} < A_{ul}/C_{ul}$ escape after scattering. Photons produced at greater depths are converted into heat before escaping. In this latter case, the level is collisionally dominated, and its population is close to LTE. If the line is optically thick, it will radiate as a black body. However EP are an approximation method affected by several deficiencies. For instance, the temperature and the ionization state are not constant across the line-forming region as assumed in the formal derivation. It is difficult to know to what extent these problems affect the predictions since as for now no definitive calculations exist for the complete non-LTE equilibrium and the line emission problem at intermediate densities ($10^{10} - 10^{15}\,\mathrm{cm}^{-3}$). Hence this approach is used in many state-of-the-art photoionization codes with the eventual goal of a complete description of how matter produces light without compromise for the energy conservation, the detailed treatment of the atomic physics and RT to be attained with the advent of more powerful machines and new programming methods.

Code structure

This Section gives a brief schematic view of the higher level code structure. This is the same when the code is used as a stand-alone program or as a sub-program of other larger codes.

CLOUDY is initialized and controlled by the program *main*. The left panel of Fig. 5.1 shows that after reading the input stream the *main* routine calls *cdDrive* to compute the model and then checks whether any problems occurred during the calculation by calling *cdNwcns*. It then prints a brief summary of what happened and stops.

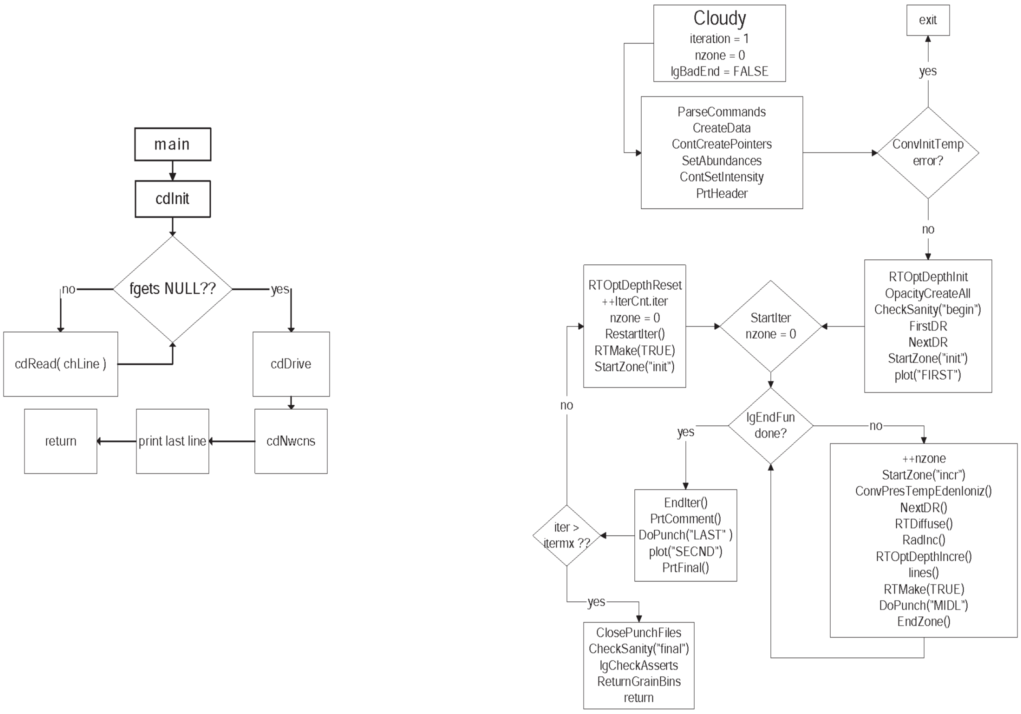

Figure 5.1: Schematic illustration of the program *main* that controls the code CLOUDY (*left*) and of the subroutine *cloudy* that controls the integration over the zones of a cloud model (*right*)

To perform most of the actual computation *cdDrive* calls the subroutine *Cloudy* illustrated in the right panel of Fig. 5.1. This routine controls the zone and iteration variables *nzone* and *iter*. At its outermost level, the routine controls the number of iterations and stops when the simulation is complete. Within this loop is an inner loop that determines whether a particular iteration is complete. This loop controls the integration over zones and checks stopping criteria to determine whether the structure is complete.

Many quantities must be simultaneously converged to compute the cloud structure. The table in Fig. 5.2 shows that at the highest level the pressure is converged by the routine *ConvPresTempEdenIoniz*. This solver assumes

Routine	Ionization OTS	Electron density	T_{kin}	Pressure	Trace keyword
ConvPresTempEdenIoniz	Stable	Stable	Stable	Solve	pressure
ConvTempEdenIoniz	Stable	Stable	Solve		temperature
ConvEdenIoniz	Stable	Solve			eden
ConvIoniz	Solve				ioniz
ConvBase	Drive				

Figure 5.2: List of the nested routines of the code responsible for the convergence of the different physical quantities needed to specify a cloud model.

that all the other quantities are known. Below that is the temperature solver, *ConvTempEdenIoniz*, which is not concerned with the pressure, but assumes that the ionization and electron density are known. Further below is the electron density solver, *ConvEdenIoniz*, which assumes that the level of ionization and the OTS rates are known.

Untill the pressure is declared converged, the major loop of *ConvPresTempEdenIoniz* determines what the local pressure should be, changing the density if necessary, and then calls *ConvTempEdenIoniz* to determine the local temperature, electron density, and level of ionization. A great deal of the code within *ConvTempEdenIoniz* is in identifying problems in obtaining temperature convergence. A temperature failure occurs and the simulation is halted when heating (G) and cooling (Λ) do not balance within a certain tolerance that can be set in the code. The temperature convergence problem is physical when the temperature failure occurs because more than one temperature solution is possible. The criterion of thermal stability used by the code is that the net cooling, $\Lambda - G$, has a positive temperature derivative computed at constant density.

I/O for BLR clouds models

Photoionization codes such as CLOUDY predict a large number of observables resulting from only a few input parameters. Ionization fractions, continuum and line optical depths, the intensity of the continuum emerging from the cloud and other relevant properties together with many millions of spectral lines can be computed from the specification of only:
(i) the shape and intensity of the external radiation field striking a cloud;

(ii) the chemical composition and grain content of the gas;
(iii) the geometry of the gas, including its radial extent and the dependence of density on radius.
In out work we adopted one of the different models stored in the code using the **table AGN** command to model the shape of the continuum incident on the BLR clouds. The considered template is meant to be similar to typical radio-quiet AGN spectra. A grid of models was obtained with the **vary** command to account for BLR clouds, each with a different total hydrogen density ($n_{\rm H}$), distributed around the central source at different radii and therefore striked by different hydrogen ionizing photon fluxes ($\Phi_{\rm H}$).

The limits to the range of $n_{\rm H}$ and $\Phi_{\rm H}$ are motivated by physical or observational considerations. Clouds located further away from the ionizing source ($\log\,(\Phi_{\rm H}/{\rm cm}^{-2}\,{\rm sec}^{-1}) < 18$) give a very low contribution to the emission and form graphite grains, while the absence of broad forbidden lines implies that clouds with lower density ($n_{\rm H} < 10^{8}\,{\rm cm}^{-3}$) are not present. Clouds very close to the ionizing source ($\log\,(\Phi_{\rm H}/{\rm cm}^{-2}\,{\rm sec}^{-1}) > 24$) or with very high densities ($n_{\rm H} > 10^{14}\,{\rm cm}^{-3}$) are either at the Compton temperature or so dense that they become predominantly continuum emitters.

To stop the computations the requirement was to reach a total hydrogen column density $N({\rm H}) = 10^{23}\,{\rm cm}^{-2}$ while the chemical composition was set to the solar value considering that: the majority of the broad emission lines, and in particular those considered in our work, are mostly formed at the considered column density and are not strongly affected by the choice of metallicity (see e.g. Korista et al. 1997, Korista & Goad 2000).

Each cloud was assumed to have a constant density and the default plane-parallel open geometry, i.e. that the cloud distance from the source is much greater than the cloud thickness, appropriate for small cloud covering factors as in the case of BLR clouds. Finally we have to consider that the default number of iterations over the cloud zones is 1 while radiative transfer effects are in important in BLR clouds. Hence we include the **iterate to converge** command in order to perform all the iterations needed to converge the optical depths.

In the panels of Fig. 5.3 we show the results of the above calculations used in our work so that they can be compared with those obtained in a similar computation by Korista et al. (1997). In particular, we display the BLR clouds reprocessing efficiency expressed in terms of the equivalent width (EW, W_{λ}) of the Hβ, the MgII and the CIV line in the $n_{\rm H}$-$\Phi_{\rm H}$ plane. The EWs are computed relative to the incident continuum at 1215 Å assuming

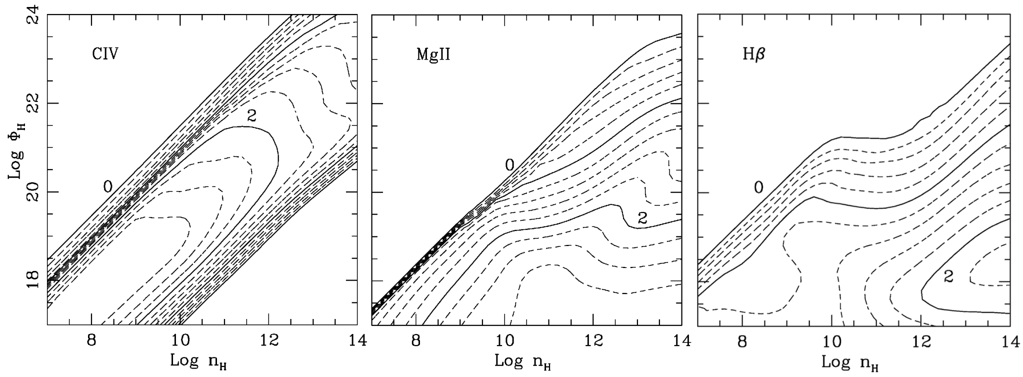

Figure 5.3: Equivalents widths of the CIV (*left*), the MgII (*middle*) and the Hβ(*right*) line relative to the incident continuum at 1215 Å emitted by BLR clouds with different hydrogen densities (n_{H}) and exposed to different ionizing photon fluxes (Φ_{H}). Solid lines are separated by 1 dex and dashed lines by 0.2 dex. The smallest (1 Å) and the largest (100 Å) solid contour lines are labeled in each plot.

full covering factor according to:

$$W_{\lambda} = \int \frac{F^{\mathrm{l}}_{\lambda} - F^{\mathrm{c}}_{\lambda}}{F^{\mathrm{c}}_{\lambda}}\, d\lambda \approx \lambda \frac{F_{\mathrm{line}}}{\lambda F^{\mathrm{c}}_{\lambda}} \tag{5.26}$$

where F^{c}_{λ}, F^{l}_{λ} and F_{line} are the specific flux of the incident continuum and of the emission line at wavelength λ and the emission line flux, respectively. The smallest (1 Å) and the largest EW logarithmic contours are labelled for each line. Contours with constant ionization parameter $U(\mathrm{H}) = \Phi_{\mathrm{H}}/n_{\mathrm{H}}c$ are parallel to the diagonal line at 45°.

Looking at the three panels it can be noted that the high ionization collisionally excited CIV line is preferentially emitted in a narrow area on the density-flux plane with EW contours running at constant $U(\mathrm{H})$. The EW decreases sharply when moving orthogonal to the diagonal band because $U(\mathrm{H})$ is either too low (lower right) or too high (upper left). Conversely, the Hβ and MgII lines are emitted over a wider area including the low Φ_{H}- high n_{H} regions since the relative ions still exist under these conditions. Hence the EW peak of the two lines with lower ionization potential shifts at lower $U(\mathrm{H})$ implying that they are more efficiently emitted at larger distances from the ionizing source relative to the CIV line in agreement with the reverberation mapping observational results (e.g. Peterson et al. 2004 and references therein).

Bibliography

Aarseth, S. J. 2003, Ap&SS, 285, 367

Adelman-McCarthy, J. K., et al. 2007, ApJS, 172, 634

Alexander, D. M., Bauer, F. E., Brandt, W. N., et al. 2003, AJ, 125, 383

Amaro-Seoane, P., Aoudia, S., Babak, S., et al. 2012, Classical and Quantum Gravity, 29, 124016

Armitage, P. J., & Natarajan, P. 2002, ApJL, 567, L9

Armitage P.J., Natarajan P., 2005, ApJ, 634, 921

Artymowicz, P., & Lubow, S. H. 1994, ApJ, 421, 651

Baldwin, J., Ferland, G., Korista, K., & Verner, D. 1995, ApJL, 455, L119

Ballo, L., Braito, V., Della Ceca, R., Maraschi, L., Tavecchio, F.,& Dadina, M. 2004, ApJ, 600, 634

Barnes, J., Hut, P., 1986, Nature, 324, 446

Barnes, J. E., & Hernquist, L. 1996, ApJ, 471, 115

Barrows, R. S., Lacy, C. H. S., Kennefick, D., Kennefick, J., & Seigar, M. S. 2011, NewA, 16, 122

Barth, A. J., Bentz, M. C., Greene, J. E., & Ho, L. C. 2008, ApJL, 683, L119

Baumgardt, H., Gualandris, A., & Portegies Zwart, S. 2006, MNRAS, 372, 174

Begelman M.C., Blandford R.D., Rees M.J., 1980, Nature, 287, 307

Berczik P., Merritt D., Spurzem R., Bischof H.P., 2006, ApJ, 642, 21

Bianchi, S., Chiaberge, M., Piconcelli, E., Guainazzi, M., & Matt, G. 2008, MNRAS, 386, 105

Blecha, L., Civano, F., Elvis, M., & Loeb, A. 2012, arXiv:1205.6202

Bogdanovic, T., Smith, B. D., Sigurdsson, S., & Eracleous, M. 2008, ApJS, 174, 455

Bogdanovic, T., Eracleous, M., & Sigurdsson, S. 2009, American Astronomical Society Meeting Abstracts, 213, #328.01

Boroson, T. A., & Lauer, T. R. 2009, Nat, 458, 53

Boroson, T. A., & Lauer, T. R. 2010, AJ, 140, 390

Callegari, S., Mayer,L., Kazantzidis, S., et al. 2009, ApJL, 696, L89

Callegari, S., Kazantzidis, S., Mayer, L., et al. 2011, ApJ, 729, 85

Caproni, A., Abraham, Z., & Monteiro, H. 2012, arXiv:1210.2286

Chornock, R., Bloom, J. S., Cenko, S. B., et al. 2010, ApJL, 709, L39

Civano, F., Elvis, M., Lanzuisi, G., et al. 2010, ApJ, 717, 209

Colpi, M., & Dotti, M. 2011, Advanced Science Letters, 4, 181

Comerford, J. M., Griffith, R. L., Gerke, B. F., et al. 2009a, ApJL, 702, L82

Comerford, J. M., Gerke, B. F., Newman, J. A., et al. 2009b, ApJ, 698, 956

Croton, D. J., Springel, V., White, S. D. M., et al. 2006, MNRAS, 365, 11

Cuadra, J., Armitage, P. J., Alexander, R. D., & Begelman, M. C. 2009, MNRAS, 393, 1423

Davies, R. I., Tacconi, L. J., & Genzel, R. 2004, ApJ, 613, 781

Decarli, R., Dotti, M., Falomo, R., et al. 2009a, ApJL, 703, L76

Decarli, R., Treves, A., Falomo, R., et al. 2009b, IAUC, 9047, 2

Decarli, R., Reynolds, M. T., & Dotti, M. 2009c, MNRAS, 397, 458

Decarli, R., Dotti, M., Montuori, C., Liimets, T., & Ederoclite, A. 2010, ApJL, 720, L93

Della Ceca, R., et al. 2002, ApJL, 581, L9

Devecchi, B., Rasia, E., Dotti, M., Volonteri, M., & Colpi, M. 2009, MNRAS, 394, 633

Di Matteo, T., Springel, V., & Hernquist, L. 2005, Nat, 433, 604

Dotti M., Colpi M., Haardt F., 2006, MNRAS, 367, 103

Dotti M., Colpi M., Haardt F., Mayer L., 2007, MNRAS, 379, 956

Dotti, M., Ruszkowski, M., Paredi, L., et al. 2009a, MNRAS, 396, 1640

Dotti, M., Montuori, C., Decarli, R., et al. 2009b, MNRAS, 398, L73

Dotti, M., Sesana, A., & Decarli, R. 2012, Advances in Astronomy, 2012,

Downes D., Solomon P.M., 1998, ApJ, 507, 615

Eggleton, P. P. 1983, ApJ, 268, 368

Eisenhauer, F., et al. 2004, Astronomische Nachrichten, 325, 120

Eracleous, M., Halpern, J. P., Gilbert, A. M., Newman, J. A.,& Filippenko, A. V. 1997, ApJ, 490, 216

Eracleous, M., & Halpern, J. P. 2003, ApJ, 599, 886

Eracleous, M., Lewis, K. T., & Flohic, H. M. L. G. 2009, NewAR, 53, 133

Eracleous, M., Boroson, T. A., Halpern, J. P., & Liu, J. 2012, ApJS, 201, 23

Escala A., Larson R.B., Coppi P.S., Maradones D., 2005, ApJ, 630, 152

Escala A., Larson R.B., Coppi P.S., Maradones D., 2004, ApJ, 607, 765

Evans, D. A., et al. 2008, ApJ, 675, 1057

Fabbiano, G., Wang, J., Elvis, M., & Risaliti, G. 2011, Nat, 477, 431

Ferland, G. J., Korista, K. T., Verner, D. A., Ferguson, J. W., Kingdon, J. B.,& Verner, E. M. 1998, PASP, 110, 761

Ferrarese, L., & Ford, H. 2005, SSR, 116, 523

Fried, J. W., & Ulrich, H. 1985, AAp, 152, L14

Fu, H., Yan, L., Myers, A. D., et al. 2012, ApJ, 745, 67

Garcia-Marin, M., Colina, L., Arribas, S., Alonso-Herrero, A., & Mediavilla, E. 2006, ApJ, 650, 850

Gaskell, C. M. 1983, Liege International Astrophysical Colloquia, 24, 473

Gaskell, C. M. 2009, NewAR,53, 140

Gerssen, J., van der Marel, R. P., Axon, D., et al. 2004, AJ, 127, 75

Gezari, S., Halpern, J. P., & Eracleous, M. 2007, ApJS, 169, 167

Gingold R.A., Monaghan J.J., 1977, MNRAS, 181, 375

Godfrey, L. E. H., Lovell, J. E. J., Burke-Spolaor, S., et al. 2012, ApJL, 758, L27

Governato F., Colpi M., Maraschi L., 1994, MNRAS, 271, 317

Green, P. J., Myers, A. D., Barkhouse, W. A., et al. 2010, ApJ, 712, 762

Guainazzi, M., Piconcelli, E., Jiménez-Bailón, E., & Matt, G. 2005, AAp, 429, L9

Guidetti, D., Murgia, M., Govoni, F., Parma, P., Gregorini, L., de Ruiter, H. R., Cameron, R. A., & Fanti, R. 2008, AAp, 483, 699

Gültekin, K., Richstone, D. O., Gebhardt, K., et al. 2009, ApJ, 698, 198

Haiman, Z., Kocsis, B., & Menou, K. 2009, ApJ, 700, 1952

Hayasaki K., Mineshige S., Sudou H., 2007 PASJ, 59, 427

Hayasaki, K., Mineshige, S., & Ho, L. C. 2008, ApJ, 682, 1134

Hayasaki, K. 2009, PASJ,61, 65

Heckman, T. M., Krolik, J. H., Moran, S. M., Schnittman, J., & Gezari, S. 2009, ApJ, 695, 363

Hernquist L., Katz N., 1989, ApJ, 70, 419

Hobbs, G., Archibald, A., Arzoumanian, Z., et al. 2010, Classical and Quantum Gravity, 27, 084013

Hopkins, P. F., Hernquist, L., Cox, T. J., et al. 2006, ApJS, 163, 1

Hudson, D. S., Reiprich, T. H., Clarke, T. E., & Sarazin, C. L. 2006, AAp, 453, 433

Ivanov P.B., Papaloizou J.C.B., Polnarev A.G. 1999, MNRAS, 307, 79

Iwasawa, M., An, S., Matsubayashi, T., Funato, Y., & Makino, J. 2011, ApJL, 731, L9

Kaspi, S., Brandt, W. N., Maoz, D., et al. 2007, ApJ, 659, 997

Kazantzidis S. et al., 2005, ApJ, 623, L67

Khan, F. M., Just, A., & Merritt, D. 2011, ApJ, 732, 89

Klamer, I., Subrahmanyan, R., & Hunstead, R. W. 2004, MNRAS, 351, 101

Komossa, S. 2003, The Astrophysics of Gravitational Wave Sources, 686, 161

Komossa, S. 2006, Memorie della Societa Astronomica Italiana, 77, 733

Komossa, S., Zhou, H., & Lu, H. 2008, ApJL, 678, L81

Korista, K., Baldwin, J., Ferland, G., & Verner, D. 1997, ApJS, 108, 401

Korista, K. T., & Goad, M. R. 2000, ApJ, 536, 284

Kormendy, J., & Gebhardt, K. 2001, 20th Texas Symposium on relativistic astrophysics, 586, 363

Koss, M., Mushotzky, R., Treister, E., et al. 2011, ApJL, 735, L42

Kunert-Bajraszewska, M., & Janiuk, A. 2011, ApJ, 736, 125

Lauer, T. R., & Boroson, T. A. 2009, ApJ, 703, 930

Lehto, H. J., & Valtonen, M. J. 1996, ApJ, 460, 207

Lewis, K. T., Eracleous, M., & Storchi-Bergmann, T. 2010, ApJS, 187, 416

Lin, D. N. C., & Papaloizou, J. 1979, MNRAS, 188, 191

Liu, X., Civano, F., Shen, Y., et al. 2012, arXiv:1209.5418

Lodato, G., Nayakshin, S., King, A. R., & Pringle, J. E. 2009, MNRAS, 398, 1392

Lousto, C. O., & Zlochower, Y. 2009, PhRvD, 79, 064018

Lousto, C. O., & Zlochower, Y. 2011, Physical Review Letters, 107, 231102

Lucy, L.B., 1977, AJ, 82, 1013

Maness, H. L., Taylor, G. B., Zavala, R. T., Peck, A. B., & Pollack, L. K. 2004, ApJ, 602, 123

Narayanan, D., Bothwell, M., & Davé, R. 2012, MNRAS, 426, 1178

Makino J., Ebisuzaki T., 1996, ApJ, 465, 527

Makino J., Funato Y., 2004, ApJ, 602, 93

MacFadyen, A. I., & Milosavljević, M. 2008, ApJ, 672, 83

Mayer L., Kazantzidis S., Madau P., Colpi M., Quinn T., Wadsley J., 2007, Science, 316, 1874

Mazzarella, J. M., Iwasawa, K., Vavilkin, T., et al. 2012, AJ, 144, 125

McLure, R. J., & Jarvis, M. J. 2002, MNRAS, 337, 109

Merloni, A. 2004, MNRAS, 353, 1035

Merritt D., Poon M.Y., 2004, ApJ, 606, 788

Merritt, D.,& Milosavljevic, M. 2005, Living Reviews in Relativity, 8, 8

Merritt, D., Mikkola, S., & Szell, A. 2007, ApJ, 671, 53

Merritt, D., & Vasiliev, E. 2011, ApJ, 726, 61

Milosavljević M., Merritt D., 2001, ApJ, 563, 34

Milosavljevic, M., & Merritt, D. 2003a, The Astrophysics of Gravitational Wave Sources, 686, 201

Milosavljević, M., & Merritt, D. 2003b, ApJ, 596, 860

Montuori, C., Dotti, M., Colpi, M., Decarli, R., & Haardt, F. 2011, MNRAS, 412, 26

Montuori, C., Dotti, M., Haardt, F., Colpi, M., & Decarli, R. 2012, MNRAS, 425, 1633

Mortlock, D. J., Warren, S. J., Venemans, B. P., et al. 2011, Nat, 474, 616

Nixon, C. J., Cossins, P. J., King, A. R., & Pringle, J. E. 2011, MNRAS, 412, 1591

Osterbrock, D. E., & Ferland, G. J. 2006, Astrophysics of gaseous nebulae and active galactic nuclei, 2nd. ed. by D.E. Osterbrock and G.J. Ferland. Sausalito, CA: University Science Books, 2006

Ostriker E., 1999, ApJ, 513, 252

Perets, H. B., Hopman, C., & Alexander, T. 2007, ApJ, 656, 709

Peterson, B. M., Ferrarese, L., Gilbert, K. M., et al. 2004, ApJ, 613, 682

Piconcelli, E., Vignali, C., Bianchi, S., et al. 2010, ApJL, 722, L147

Preto, M., Berentzen, I., Berczik, P., & Spurzem, R. 2011, ApJL, 732, L26

Quinlan, G. D. 1996, NewA, 1, 35

Richards, G. T., Lacy, M., Storrie-Lombardi, L. J., et al. 2006, ApJS, 166, 470

Richards, G. T., Myers, A. D., Gray, A. G., et al. 2009, ApJS, 180, 67

Richstone, D., Ajhar, E. A., Bender, R., et al. 1998, Nat, 395, A14

Rodriguez, C., Taylor, G. B., Zavala, R. T., Peck, A. B., Pollack, L. K.,& Romani, R. W. 2006, ApJ, 646, 49

Rödig, C., Dotti, M., Sesana, A., Cuadra, J., & Colpi, M. 2011, MNRAS, 415, 3033

Rödig, C., Sesana, A., Dotti, M., et al. 2012, AAp, 545, A127

Sanders D.B., Mirabel I.F., 1996, ARA&A, 34, 749

Schlegel, D. J., Finkbeiner, D. P., & Davis, M. 1998, ApJ, 500, 525

Seaton, M. J. 1954, MNRAS, 114, 154

Sesana, A. 2010, ApJ, 719, 851

Sesana, A., Gualandris, A., & Dotti, M. 2011, MNRAS, 415, L35

Sesana, A., Roedig, C., Reynolds, M. T., & Dotti, M. 2012, MNRAS, 420, 860

Shakura N. I., Sunyaev R. A., 1973, Astronomy and Astrophysics, Vol. 24, p. 337 - 355

Shankar, F., Weinberg, D. H., & Miralda-Escudé, J. 2009, ApJ, 690, 20

Shen, Y., & Loeb, A. 2010, ApJ, 725, 249

Shen, Y., Richards, G. T., Strauss, M. A., et al. 2011, ApJS, 194, 45

Shi, J.-M., Krolik, J. H., Lubow, S. H., & Hawley, J. F. 2012, ApJ, 749, 118

Shields, G. A., Bonning, E. W., & Salviander, S. 2009a, ApJ, 696, 1367

Shields, G. A., Rosario, D. J., Smith, K. L., et al. 2009b, ApJ, 707, 936

Spaans, M., & Silk, J. 2000, ApJ, 538, 115

Springel V., Yoshida N., White S.D.M., 2001, NewA, 6, 79

Springel, V. 2005, MNRAS, 364, 1105

Springel V., Di Matteo T., Hernquist L., 2005, MNRAS, 361, 776

Syer, D., & Clarke, C. J. 1995, MNRAS, 277, 758

Tacconi, L. J., Genzel, R., Tecza, M., Gallimore, J. F., Downes, D.,& Scoville, N. Z. 1999, ApJ, 524, 732

Tadhunter, C., Ramos Almeida, C., Morganti, R., et al. 2012, arXiv:1209.3568

Tang, S., & Grindlay, J. 2009, ApJ, 704, 1189

Tarchi, A., Castangia, P., Henkel, C., & Menten, K. M. 2007, New Astronomy Review, 51, 67

Tecza, M., Genzel, R., Tacconi, L. J., Anders, S., Tacconi-Garman, L. E.,& Thatte, N. 2000, ApJ, 537, 178

Tsalmantza, P., Decarli, R., Dotti, M., & Hogg, D. W. 2011, ApJ, 738, 20

Tsalmantza, P., & Hogg, D. W. 2012, ApJ, 753, 122

Valtonen, M. J., et al. 2006, ApJ, 646, 36

Valtonen, M. J., Lehto, H. J., Nilsson, K., et al. 2008, Nat, 452, 851

Vignati, P., et al. 1999, AAp, 349, L57

Villforth, C., Nilsson, K., Heidt, J., et al. 2010, MNRAS, 402, 2087

Volonteri M., Haardt F., Madau P., 2003, ApJ, 582, 559

Volonteri, M., Miller, J. M., & Dotti, M. 2009, ApJL, 703, L86

York, D. G., Adelman, J., Anderson, J. E., Jr., et al. 2000, AJ, 120, 1579

Urry, C. M., & Padovani, P. 1995, PASP, 107, 803

Wada, K., & Norman, C. A. 2001, ApJ, 547, 172

Worrall, D. M., et al. 1982, ApJ, 261, 403

Wrobel, J. M., & Laor, A. 2009, ApJL, 699, L22